CanmetMATERIALS

Strength, Creep, and Toughness of Two Tank Car Steels

TC128B and A516-70

Submitted to Transport Canada

GCDOCS Workflow ID 38647561

Jonathan McKinley, Su Xu, Mark Gesing,
Bruce Williams

April 2019

CanmetMATERIALS

DISCLAIMER

Natural Resources Canada makes no representations or warranties respecting the contents of this report, either expressed or implied, arising by law or otherwise, including but not limited to implied warranties or conditions of merchantability or fitness for a particular purpose.

ISBN: 978-0-660-32009-0

Cat. No.: T86-56/2019E-PDF

ACKNOWLEDGEMENTS

This work was funded by Transport Canada under the guidance of Mr. Ian Whittal and Mr. Michael Spiess. We would like to thank Dr. D.-Y. Park for his help and discussions on fracture toughness testing, especially on SE(T) tests, Drs. C. Scott and F. Fazalli for useful discussions on steel microstructure. We would also like to acknowledge the contributions of Dr. H. Simha and Dr. M. Arafin who laid the groundwork for this report before they departed CanmetMATERIALS.

Project Contributors

J. McKinley
S. Xu
B. Williams
M. Gesing
W.R. Tyson
L. Blaga
A. Laver
L. Yang
J. Liang

CONTENTS

LIST OF ACRONYMS ABREVIATIONS AND SYMBOLS

Organizations:

ASTM	American Society for Testing and Materials
AAR	Association of American Railroads
AFFTAC	Analysis of Fire Effects on Tank Cars
BLEVE	Boiling Liquid Expanding Vapour Explosion
RPI	Railway Progress Institute
TSC	Transportation Systems Center
FRA	Federal Railroad Administration
MHIDAS	Major Hazard Incident Data Service
NRC	National Research Council
US DOT	United States Department of Transportation

Technical Terms:

CE	Carbon Equivalent
CFD	Computational Fluid Dynamics
CTOA	Crack-Tip Opening Angle
CTOD	Crack-Tip Opening Displacement
CVN	Charpy 'V' Notch
DT	Dynamic Tear
DBTT	Ductile-to-Brittle Transition Temperature
DWTT	Drop-Weight Tear Test
E.L.	Tensile Elongation
FATT	Fracture Appearance Transition Temperature
FEA	Finite Element Analysis
HAZ	Heat-Affected Zone
HSLA	High Strength Low Alloy
HT	Heat Treatment
IDA	Insulation Defect Analyzer
LPG	Liquefied Petroleoum Gas
LVDT	Linear Variable Differential Transformer
NDT	Nil-Ductility Transition
PRD	Pressure Relief Device
RD	Rolling Direction
RT	Room Temperature
SE(B)	Single Edge notched Bend
SE(T)	Single Edge notched Tension
SRT	Stress Relieving heat Treatment
TD	Transverse Direction
TT	Transition Temperature
TMCP	Thermo-Mechanical Controlled Processing

YS	tensile Yield Strength
USE	Upper-Shelf Energy
UTS	Ultimate Tensile Strength

Symbols:

a_0	initial crack length
e_1, e_2, e_3	Constants used in fit for temperature-dependence of elastic modulus
E_{RT}	Room temperature Young's modulus
J	J-integral
J_{el}	elastic component of J
J_{pl}	plastic component of J
K	stress-intensity factor
K_a	fracture arrest toughness in stress-intensity factor
K_A	dynamic fracture arrest toughness in stress-intensity factor
K_{Ia}	plane-strain fracture arrest toughness in stress-intensity factor
K_{IA}	dynamic plane-strain fracture arrest toughness in stress-intensity factor
K_{Ic}	plane-strain fracture toughness
K_{Id}	dynamic fracture toughness in stress-intensity factor
K_{mat}	material fracture toughness in stress-intensity factor
r_1, r_2, r_3, r_4	constants used in fit for temperature-dependence of yield strength
T	temperature
W	width of fracture toughness specimen
σ	stress
σ_u	ultimate tensile strength
σ_y	yield strength (0.2% offset)
σ_{y0}	room-temperature yield strength
υ	Poisson's ratio
$\dot{\varepsilon}$	strain rate

LIST OF FIGURES

LIST OF TABLES

1 EXECUTIVE SUMMARY

CanmetMATERIALS (CMAT) conducted literature reviews on the fracture toughness and high-temperature performance of rail tank car steels in 2015 and 2016 at the request of Transport Canada. The objective of this work was to gain an understanding of the material parameters affecting tank car performance in accident scenarios such as tank punctures and pool fires. This work identified deficiencies in the available literature and recommended experiments to close the gaps. From 2016 to 2018 CMAT conducted a comprehensive experimental program on two common tank car steels, TC128B and ASTM 516 grade 70 (A516-70). The tests performed included; composition and microstructure, tensile testing at temperatures from -80°C to 800 °C, creep rupture testing, Charpy impact, dynamic fracture toughness using drop weight tare tests (DWTT) measuring crack tip opening angle (CTOA), and fracture toughness using single edge notched bending SE(B) and tension SE(T) specimens. Detailed results from this work are included in CMAT technical reports [1]–[6]. The main results of the work are summarized in this combined report.

The compositions of the TC128B and A516-70 steel tested in this work meet Association of American Railroads (AAR) 2014 specifications. The low sulphur and phosphorous contents are consistent with current steelmaking technology. The constituent phases are ferrite and pearlite in a heavily banded structure. Tensile properties of longitudinal and transverse samples are very similar and consistent. Tensile strengths decreased with increasing temperature. Discontinuous yielding (Lüders band formation) was found between temperatures of -80 °C and 200 °C. Lüders strains of up to 2.93% were observed and decreased with increasing temperature. Discontinuous yielding was not observed at temperatures above 200°C. The tensile test data was fit to a temperature dependent constitutive material model to be implemented in finite element code.

Both steels have Charpy absorbed energy values (CVN) that are substantially higher than the AAR specification at -46°C. Fracture propagation toughness values, $CTOA_{B/2}$, are in the low/middle range in comparison with typical pipe steels. The results of B×2B SE(B) tests, representing baseline conservative fracture toughness values, were acceptable for structural applications but relatively low in the range of typical modern pipe steels. Fracture toughness tests revealed some differences between the tank car steels compared with pipe steels (i.e., later attainment of maximum loads, small load drops during tests before maximum loads, and anomalous effects of constraint on fracture toughness) and these should also influence tank car structural performance. The results provide a fracture toughness dataset that can be used for the low-temperature integrity assessment of current tank car steels and for steel development.

Creep was observed at the test temperatures between 500 °C and 800 °C. Both steels demonstrated the typical creep response of metallic alloys with primary, secondary, and tertiary creep deformation. As expected, the rate of creep increased with temperature and applied load. For most creep tests the rupture time was within 100 minutes which is much shorter than a standard creep test. Shorter tests were performed to match the timeframe of a tank car failure. The creep rupture data will be fit to an appropriate creep model. Finite element simulations of tank cars in pool fire

scenarios can then be completed to capture the combined effect of plastic and creep deformation at high-temperature. CMAT is currently working towards this objective.

2 INTRODUCTION

CanmetMATERIALS began an investigation into the fracture toughness and high-temperature strength of rail tank car steels in 2015 at the request of Transport Canada. The objective is to gain a better understanding of how tank car steels behave in accident scenarios and, especially under pool fire conditions. The preliminary reports [1], [4] covered literature reviews on the topics mentioned above. They found that there were gaps in the available mechanical test data for the two most common tank car steels and recommended that these gaps be closed by a comprehensive test program. In the following years, CanmetMATERIALS conducted extensive mechanical testing including low-temperature tensile, high-temperature tensile, various fracture toughness tests, and creep rupture tests on TC128B and A516-70 steels. Four additional reports were written covering this work [2], [3], [5], [6]. The objective of this report is to consolidate the complete body of work to date. Internal corrosion of tank cars was also investigated in a separate report [7] which is not covered in this document.

The high-temperature stress-strain response of the two steels studied was fit to a constitutive equation with the intent to implement it in a finite element code. Similar work is to be completed on the materials' creep behaviour. Then, finite element simulations of tank car failure can be performed to capture the high-temperature plastic and creep deformation behaviour of tank car steel.

3 BACKGROUND

The rail tank cars are important for transporting commercial goods. In North America, most bulk liquid chemicals are transported in tank cars [8], including hazardous materials such as propane, ammonia, vinyl chloride, ethylene oxide, alcohol and petroleum oil/gases, often involving pressure and sometimes cryogenic temperatures [8]–[12]. Although there have been a number of high-profile tank car derailment accidents with fatalities and spills in Canada and the US recently, railroad tank cars have a better safety record than highway tank trucks, i.e., a lower frequency of reported hazardous material spills per mile shipped [11]. However, this draws attention to the evaluation of the structural integrity and fracture resistance of currently operating pressure tank cars to ensure the highest level of safety.

3.1 Tank Car Failure

The three main failure modes of tank cars are puncture related fracture, high-temperature tank failure due to fire, and failure due to fatigue crack growth. This work focusses on fracture and high-temperature properties of tank car steels. In general, the fatigue crack growth rate of steels decreases with increasing yield strength, work-hardening (e.g. [11]) and toughness. Fatigue properties and assessment will not be discussed in this report.

3.1.1 Fracture of Tank Cars

The requirements for tank car steels are strength, weldability, toughness and low cost in order to reduce car care and construction costs [8]. Strength is used for tank car design (i.e., stress-based

design) and the stress in the component (e.g., at the design shell thickness) must be lower than the strength of steel with an appropriate safety factor [13]. High-strength steel can help to reduce tank car weight. Tensile properties are essential to tank car steels and tensile strengths are known to increase with decreasing temperature and rising strain rate. A change in strength influences the fracture behaviour of tank car steels. Fracture toughness is a measure of a material's ability to resist crack initiation and propagation and is essential to the safety and reliability of tank cars that carry dangerous goods. In a fracture-mechanics-based design, the applied fracture driving force for a given flaw size under a given stress should be smaller than the fracture toughness of the steel [14]. Fracture toughness is required in order to evaluate the defect tolerance of tank cars during construction and operation (e.g., determination of the inspection interval), to avoid catastrophic fracture, to achieve appropriate puncture resistance during accidents or upon impact loading, and to ensure continuing safety of tank cars damaged after accidents.

The ductile-to-brittle transition (DBTT) behaviour of tank car steels is vital to designing for low-temperature service conditions for base steel and weldments. Steel can become brittle due to low-temperatures or high loading rates. This is due to the increased strength and therefore lower ductility of the steel under these conditions.

Tank cars experience low-temperature service in Canada and the US and high strain-rate deformation and failure in impact accidents such as collision or derailment. Knowledge of the effects of low-temperatures and high strain rates on tensile properties is important for understanding the deformation and fracture of tank car steels (for example in computer modelling [15], [16]).

It is well known that the strength (or flow stress) of steel increases with decreasing temperature and increases with strain rate. Tensile tests in a range of temperatures between -51°C and 23°C were performed for the AAR Tank Car Committee [31], [32].

3.1.2 Failure in Fire Scenarios

For flammable hydrocarbon ladings, such as crude oil, natural-gas condensates, ethanol or propane, during an accident (or derailment) there is potential for discharge owing to the failure of valves or puncture of the tank shell due to impact. In the event of a discharge of flammable lading from a tank car a pool forms and may ignite leading to a pool fire. A pool fire is defined as a turbulent diffusion fire burning above a horizontal pool of vaporizing hydrocarbon fuel, where the fuel has zero or low initial momentum. Instances of tank-car railroad accidents involving crude oil are in Lac-Mégantic, Quebec, [17]; Casselton, North Dakota, [18]; and Finland, [19]. In all of the cited accidents, a post-crash pool fire resulted. In the Lac- Mégantic accident, 47 lives were lost.

Statistics for the period of 1986 show that 16% of accidents involving freight trains conveying Petroleum Gas (LPG) in Great Britain resulted in a spill leading to fires, [20], As stated by D'Aulisa [21], analysis of tank-car accidents in databases such as Major Hazard Incident Data Service (MHIDAS), suggests that approximately 30% of accidents lead to Boiling Liquid Expanding Vapour Explosions (BLEVE). The MHIDAS, [22], is an international database of accidents and has been maintained since 1986 by the United Kingdom Atomic Energy Authority.

Pool fires, irrespective of whether the fire engulfs the car or is at distance from the car, subject the car to a thermal load (in addition to the internal vapour pressure). This load is more severe in the case wherein the tank is engulfed by the fire. From the standpoint of risk assessments for tank car designs, regulatory purposes, or design reviews, computational methods involving Computational Fluid Dynamics (CFD) for the fire modelling, and finite element-based solid mechanics for the failure modelling of the tank car may be used. For making failure predictions, mechanical properties at high-temperature are crucial.

The thermal load on the tank car may cause the lading to boil or evaporate. This increases the internal pressure of the tank car. If the pressure reaches the discharge pressure of the Pressure-Relief Device (PRD). The vapour is then vented into the atmosphere, leading to a drop in the liquid level and allowing more of the liquid to evaporate. This will also lead to a larger portion of the shell surface exposed to vapour which insufficiently cools those portions; this weakens the shell and may lead to failure. A Boiling Liquid Expanding Vapour Explosion (BLEVE) may occur under these conditions. When the shell fails, the liquid pressure suddenly drops to the atmospheric pressure. Owing to the liquid temperature being well above the boiling point at atmospheric pressure, the liquid abruptly evaporates leading to a violent expansion to a cloud that has a volume larger than that of the liquid volume by a factor on the order of magnitude of one thousand. There are some debates in the literature about the exact conditions for the onset of a BLEVE with regards to the temperature of the liquid being at the “superheat limit temperature”. For a recent review of this issue and other details regarding BLEVEs, the article by R. K. Eckhoff [23] may be consulted.

When subjected to thermal loading, the tank car shell material softens; that is, the strength of the material decreases. Data on the decrease in yield and ultimate strength of the material as a function of temperature have been reported in the following reports: [24], [25].

Failure of tank car steels in pool fire conditions can occur through two different mechanisms:

1. Short-term overheating where the shell is exposed to excessively high temperatures over short time periods leading to material softening and then failure.

2. High-temperature creep. No yielding occurs during high-temperature creep but time, temperature, and load conspire together to lead to material failure.

Creep is a time-dependent failure. A metal, exposed to both load and high temperatures can deform over time even if the applied stress is less than the yield strength of the material.

Failure due to short-term overheating usually leads to fracture surfaces that have a knife-edge like appearance and considerable wall thinning in the fracture edge. In contrast, failure surfaces owing to high-temperature creep will have thick lips or edges and rough appearance; the appearance is due to the linkage of micro-voids and inclusions leading to fracture. For more discussion, the monograph by [26] may be consulted.

Failure of the tank can be modeled using the principles of solid mechanics. Models may be classified into engineering and finite element-based methods. In the engineering approach, the yield strength is softened per some model as a function of the temperature and the corresponding

internal pressure at which the hoop stress exceeds the threshold yield is the failure pressure. A shortcoming of the engineering technique is the neglect of the time-dependence of failure at high-temperature, and this is partially alleviated by the use of rupture models for creep. Additionally, engineering assessments tend to simplify the problem which can lead to conservatism. More complexity can be added to the model for better failure predictions, but at some point it becomes more realistic to use a three-dimensional FE model to study the high-temperature plastic and creep deformation response of the material under complex loading and realistic geometry. The results of complex 3D FEM simulations could also be used to develop non-complex engineering models that accurately describe failure prediction.

3.2 Evolution of Tank Car Steels

The evolution of tank car steels has been discussed in many reports which are summarized in Table 1 [8], [27]–[33].

- Until 1966, ASTM A212B and A285C steels were mainly used to build tank cars [28], [29]. A212 was specified as high tensile strength steel plates for boilers and other pressure vessels. The specification for A212B became obsolete when ASTM withdrew it in 1966 [29].
- ASTM A515-70 steel replacrd A212B. Because normalization heat treatment was not required at that time [27], these tank car steels are coarse grained in the as-rolled condition.
- ASTM A515-70 steel was replaced by ASTM A516-70 (fine grained) for improved low-temperature toughness but the improvement was found to be useful only to the weld and not in terms of steel toughness [8].
- ASTM A285C was specified as a pressure vessel steel and the use of A285C was discontinued for pressure cars in the mid-1960s and for non-pressure cars in the early 1980s[28].
- In the mid-1960s, TC128A was used to build some tank cars in the as-rolled condition, which was essentially identical to ASTM A612 processed to fine grains [27].
- In the 1970s, the AAR sponsored the development of TC128B steel [8]. Due to the relatively high cost of TC128B, it was mainly used for pressure tank cars between the mid-1960s and mid-1980s, and A515/A516 was used for non-pressure tank cars [28].

The normalization heat treatment of tank car steels was not required until the mid-1980s; as-rolled steels were largely used, which are characterized by a coarse-grained microstructure, lower fracture toughness and higher DBTT compared to normalized steels. The FRA and Transport Canada have required normalized TC128B or normalized A516-70 steels for pressure cars carrying hazardous materials since 1989 and 1999, respectively. As-rolled A516-70 was most common for non-pressure cars and normalized TC128B is now most common for pressure cars [28]. In 2003, the AAR also recommended the use of normalized steels as opposed to as-rolled steels in the construction of non-pressure cars carrying hazardous materials (as cited in [33]). Therefore, all tank car steels are now required to undergo a normalization heat treatment in order to achieve the specified toughness to carry hazardous materials for low-temperature service (e.g., in northern climates, which is the case for Canada and the US) and/or to carry liquid CO_2.

Table 1: Evolution of tank car steels for shell construction [8], [27]–[33]

Steel	Heat Treatment	Year Used for Construction	Pressure-car or Non-pressure Car
A212B	As-rolled	Before 1966	Both
A285C	As-rolled	Before mid-1960s	Pressure-car
		Before early 1980s	Non-pressure car
A515-70	As-rolled	After 1966	Both
A516-70	As-rolled	After 1966	Both
	As-rolled	After 1989	Non-pressure car
	Normalized	After 1989	Pressure-car
	Normalized	After 2003	Non-pressure car
TC128B	As-rolled	Mid-1960 to Mid-1980s	Mainly pressure-car
	Normalized	After 1989	Both

Tank car steels used in pressure cars prior to 1989 are shown in Figure 1 [31], [32]. It is evident that TC128B is the main steel for pressure tank car construction (93.3%). Also note that since the life of a tank car can be long, some tank cars built in the 1960s were still in use at the survey time. The design life of pre-1974 tank cars was forty years and that of post-1974 tank cars is fifty years. Note that the observations in Figure 1 are based on 2008 data and the composition of the tank car fleet may have changed significantly since then. Since TC128B and A516-70 are the tank car steels currently used for tank car construction, they will be the focus of this work.

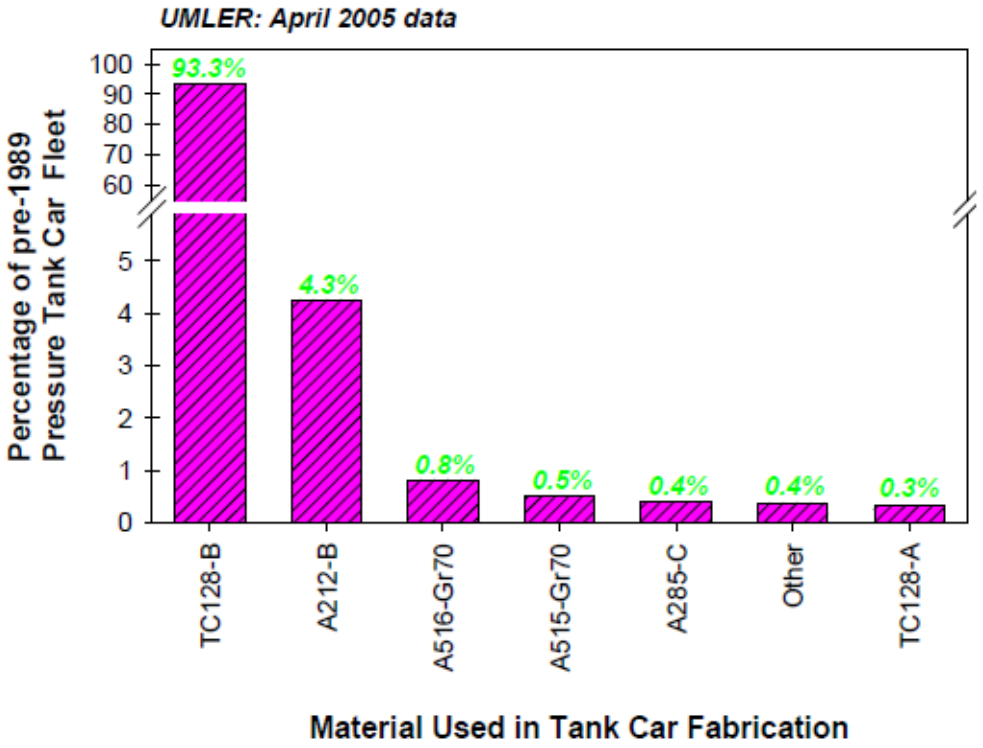

Figure 1: Steels used in pre-1989 pressure tank cars [31], [32]

All tank car steels are medium carbon steels. The main compositions of tank car steels and potential tank car steels are set out in Table 2, along with the maximum contents or allowable range in heat analysis. ASTM A212B, A285C, A515-70 and A516-70 steels contain only C and Mn as alloying elements and TC128B is a micro-alloyed high-strength low-alloy (HSLA) steel as shown in Table 2 (most data from [8]). Aluminium and Silicon are used for removing oxidation during the tank car steelmaking process and are not listed as alloying elements in Table 2. Also listed in Table 2 are the main chemical compositions of an experimental steel (A-8XX) and more recent Thermo-Mechanical Controlled Processing (TMCP) pipe steels for comparison.

Table 2: Comparison of major alloy compositions of steels (wt%) [8]

Steel	C	Mn	Si	Al	Cu	Nb	Ni	V
A212B*	0.31	0.90	0.15-0.30					
A285C**	0.28	0.98						
A515	0.31	1.30	0.45					
A516	0.28	1.30	0.45					
TC128B	0.29	1.46	0.45					0.08
A-8XX	0.16	1-1.75	0.15-0.50			0.06		0.11
Pipe Steel (e.g., X70)	0.08-0.09	1.90	0.25-0.35	0.025-0.035	0.00-0.20	0.045-0.055	0.00-0.11	0.07-0.08

* Data cited from ASTM A212-64, 1964.
** Data cited from ANSI/ASTM A285-78, 1978.

Since 1998, AAR specification (M-128) requires new tank cars to be stress relieved at 649°C (1200°F) for one hour after fabrication (as cited in [34]). In general, the SRT slightly decreased the strengths and increased or maintained the ductility of TC128B [24]. This is beneficial to low-temperature fracture properties, especially since TC128B and A516-70 are usually produced to considerably exceed the specified yield strength (YS) and meet the upper limit ultimate tensile strength (UTS) [35], [36].

3.2.1 Proposed Tank Car Steel Improvements

Micro-alloying is an effective means of achieving a fine-grained microstructure, strength and toughness, especially in combination with proper heat treatment or TMCP. Since the 1980s, the industry and the AAR have investigated different low-C micro-alloyed TMCP steels [8], [12], [33], [37]–[45] for tank car applications. These micro-alloyed steels offer a good strength and toughness combination and have less carbon content to reduce the carbon equivalent (CE), which is a common indicator of weldability. TMCP steels, including pipe steels, are used in the as-rolled condition. This may reduce the fabrication cost. Another advantage of TMCP steels is that field welding can be done without post-weld heat treatment. Some of the potential tank steels may be used to transport cryogenic liquids [12]. However, these alloys have not been used in

tank car construction due to low weld metal Charpy toughness [12], [33], [39], [44] or low toughness of HAZ [45] after Stress Relieving Treatment (SRT), no improvement [40] or no drastic improvement of Charpy toughness [45], segregation bands and martensite streaks [44], and cost (e.g. [43]). Note that the usual design temperature of the buried pipeline (-5 to -20°C) is higher than that of tank car steels (-46°C [46]) for low-temperature service. Unless the overall material and construction cost is reduced compared to TC128B steel, these applications of micro-alloyed steels will not be realized.

3.3 Specifications for TC128B and A516-70 Steels

The tank car steel specification outlines requirements in terms of chemical composition, mechanical properties and tests to be performed, as well as processes. In AAR specification M1002 [47], tank car steel must be made to fine grain practice in as-rolled or normalized condition. When specified for low-temperature service, the steel must be normalized to meet the CVN (Charpy absorbed energy) requirement.

Chemical composition is one of the basics for controlling the properties of steels and is determined by the current knowledge of its influence on performance properties (mainly strength and toughness), processing properties (e.g., weldability and formability) and cost. The chemical compositions of AAR TC128B and A516-70 are listed in Table 3 [46], [47]. The compositions given for TC128B are for plates 19.1mm thick or less. The A516-70 specifications due not change with thickness. The composition requirements for TC128B and A516-70 in the AAR specifications have evolved with the advancement of steelmaking technology to lower limits on S (0.015%), CE (0.53 for TC128B and 0.45 for A516-70) and micro-alloying elements to the total amount (Nb+Ti+V=0.11%) as described in [45]. These additional requirements have been included in AAR M1002 [46] or appear as an AAR supplemental requirement to ASTM 516/516M [29] for improved Charpy Upper-Shelf Energy (USE), weldability and formability [45]. In AAR specification M128.00 (the specification for high-strength carbon manganese steel plates for tank cars, AARTC128-70) as cited in [25], both TC128A and TC128B grades are included. Grade A requires a minimum of 0.02% V, whereas Grade B has no minimum V requirement. The Grade B steel specification has maximum limits for Ni, Cr, Mo, Cu and V contents, while maximum limits are not specified for Grade A steel.

Specified tensile properties of TC128B and A516-70 steels are set out in Table 4 [46], [47]. TC128B is a 50-ksi yield strength and 81-ksi UTS steel. A516-70 is a 38-ksi YS and 70-ksi UTS steel.

The Charpy toughness requirements for low-temperature service for TC128B and A516-70 steels are set out in Table 5 [46]. The test coupons must simulate the in-service condition of the material (e.g., after stress-relief heat treatment following fabrication). The requirement is to ensure the performance requirement to avoid brittle fracture during low-temperature service. The length of the Charpy specimen is in the longitudinal direction (i.e., rolling direction). According to the AAR specification (AAR M-1002, Chapter 2, paragraph 2.2.1.2) [46], *for non-low-temperature service*, Charpy specimens are transverse to the rolling direction in accordance with ASTM A20; the requirement is an average of 20.3 J for 3 specimens at -34.4°C with no single

value below 13.6 J and no two values below 20.3 J. However, this transverse testing is not required for *low-temperature service*.

Table 3: Chemical limits for heat and product analyses for TC128B and A516-70 (wt%) [46], [47]

Element	TC128B, maximum permitted – Plate 19.1 mm thick or less		A516-70, maximum permitted	
	Heat Analysis	Product Analysis	Heat Analysis	Product Analysis
C	0.24	0.28	0.27	0.27
Mn	1.00-1.65	1.00-1.70	0.85-1.20	0.79-1.30
P	0.025	0.25	0.025	0.025
S	0.009	0.009	0.025	0.025
Si	0.15-0.40	0.13-0.45	0.15-0.40	0.13-0.45
V	0.08	0.084		
Cu	0.35	0.35		
Al	0.015-0.060	0.015-0.060		
Nb	Per ASTM A20 [47]	Per ASTM A20		
Ti	0.020	0.020		
B	0.0005	0.0005		
N	0.010	0.012		
Sn	0.020	0.020		
Nb+V+Ti	0.11	0.11		
Cu+Ni+Cr+Mo	0.65	0.65		

Table 4: Tensile requirements for TC128B and A516-70 [46], [47]

Steel	**YS (MPa)/(ksi)**	**UTS (MPa)/(ksi)**	**E.L. (5) in 50 mm**
TC128B	Min. 345/(50)	560-695/(81-101)	22.0
A516-70	Min. 260/(38)	485-620/(70-90)	21.0

Table 5: CVN requirements for tank car [46]

T (°C)	**Orientation**	**CVN (J)**
-45.6	Longitudinal	20.3 J min. average for 3 specimens and 13.6 J min. for 1 specimen

Typical optical micrographs of normalized TC128B and A516-70 steels are shown in Figure 2 [34] and Figure 3 [48]. The microstructures of TC128B and A516-70 consist of fine-grained pearlite and ferrite phases. The slightly aligned or banded microstructures are due to the steel hot-rolling process and are parallel to the rolling direction (i.e., grain or metal flow direction). This aligned microstructure is responsible for the mechanical property anisotropy in rolled steel plate. The orientations in steel plate are usually identified as the rolling (or longitudinal) direction, transverse direction and short-transverse direction (i.e., through-thickness direction). In fracture toughness testing, both loading and fracture propagation plane orientations are relevant and the code for orientation as per ASTM 1823 [49] is shown in Figure 4 for reference.

In Figure 4, the first letter indicates the orientation of loading and the second letter is the crack propagation direction.

Figure 2: Micrographs of TC128B (the micro-bar in the figure is 100 μm) [34].

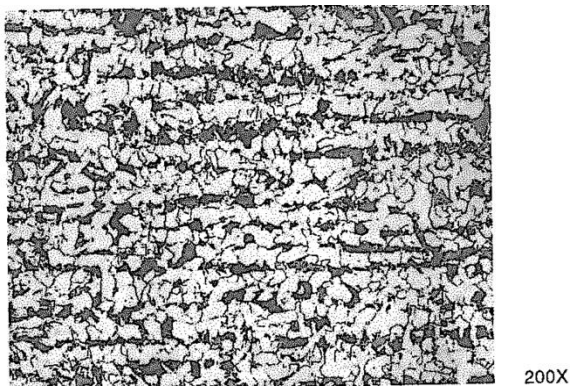

Figure 3: Micrograph of A516-70H [48].

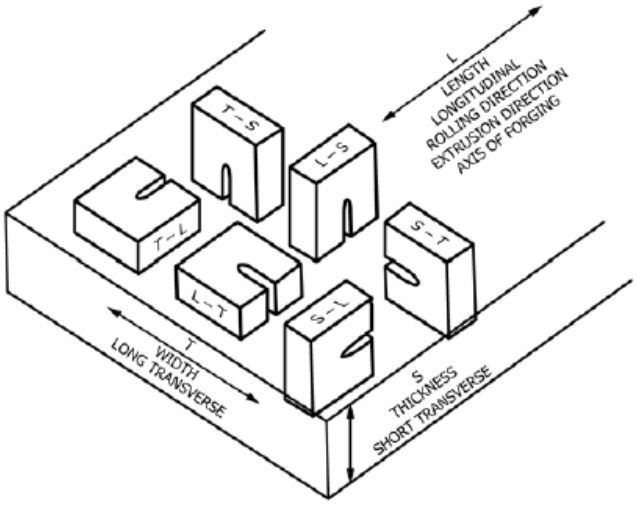

Figure 4: Crack plane orientation code for plate [49].

3.4 Previous Work on High-Temperature Properties of Tank car steels

No high-temperature performance specifications exist for tank car steels and little data has been published on this topic. Data on the decrease in yield and ultimate strength of TC128B as a function of temperature has been reported by Hicho and Harne, as well as Zahoor and Hicho [25], [50]. Therein standard “dog-bone” shaped samples were subjected to uni-axial tensile loading at elevated temperature. These tests were carried out at the stated temperatures. The samples were held at temperature for 30, 60, and 120 minutes. This data is reproduced in Figure 5. As a point of reference, the minimum room temperature (RT) values of the yield and ultimate strength are shown as dotted and dashed lines. Actual room temperature data for the material tested was not provided. Significant softening upon increase in temperature is apparent. Stress-strain curves for TC128B as a function of temperature were not found in the literature.

A M Birk and K T Yoon [51] carried out an extensive testing program to measure the rupture times in both the longitudinal and hoop direction of three different vintages (1964, 1968, 2002) of TC128 grade B steel. Typical rupture times for TC128 grade B steel are shown in Figure 6. As data in the figure shows, with increased temperature, there is a decrease in both the rupture time and stress at which rupture occurs. They found that 2002 and 1968 steels have superior stress-rupture properties than the 1964 TC128B.

In order to model the high-temperature behaviour of tank car steels a comprehensive set of data is required which includes complete stress-strain curves at a wide range of temperatures and creep-rupture data for the same material at the same temperatures. This data does not currently exist in open literature.

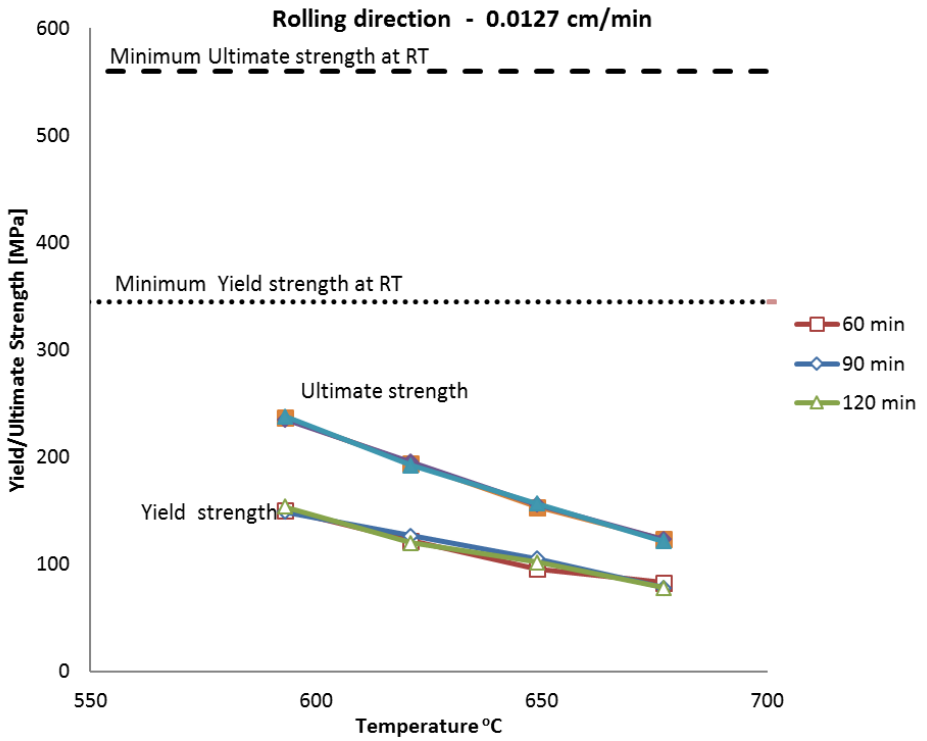

Figure 5: Quasi-static high-temperature tensile testing data for TC128 Grade B [50]. For reference, minimum yield and ultimate strength at RT are shown as dotted and dashed lines.

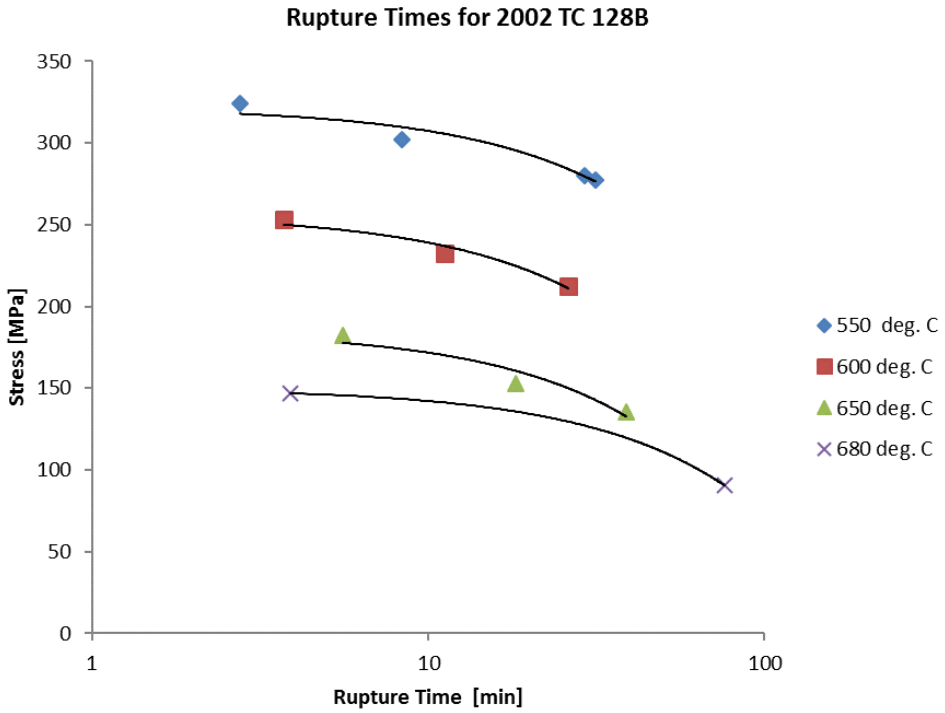

Figure 6: Rupture times for TC128 grade B steel of 2002 vintage. Specimens were machined from ex-service tanks in the hoop direction. [51]

4 MATERIALS FOR EXPERIMENT

This section describes the origin of the samples of TC128B and A516 used in the experiments described in the following sections of this report.

4.1 TC 128B

A piece of TC128B steel was obtained from a tank car that had been subjected to side impact testing in September 2016, sponsored by the US Department of Transportation (DOT). The tank car was built and qualified in 2015. The steel was from the shaped tank car shell about one ring in from the heads as shown in Figure 7. It was a curved plate taken as far as practical from the side impact site and centered between circumferential welds, of thickness (B) 15.2 mm. The plate rolling direction (RD) is normal to the axis of the tank. Mechanical test samples were machined from the panel (arrow) shown in Figure 7.

Figure 7: US Federal Railroad Administration impact-tested tank car, showing location of TC128B panel used in this work. Photo provided by Nolan Hanson of the Transportation Technology Center, Inc.

4.2 ASTM 516 Grade 70

A formed sample of A516-70 was not available to CanmetMATERIALS therefore a piece of commercial A516-70 steel plate in the normalized condition was purchased instead; the steel was manufactured in 2016 by ArcelorMittal Plate LLC. The normalization treatment involved heating to 899°C for 24 minutes followed by air-cooling. The nominal steel plate thickness (B) is

19.1 mm. In service A516-70 may have slightly different properties than this plate due to the additional fabrication processes that it has undergone.

5 EXPERIMENTAL PROCEDURES

In this section a brief description of each experiment is provided followed by the insight that the experiment provides.

5.1 Composition and Microstructure

The composition of the material was measured using a Baird One Spark OES (optical emission spectrometer). Measurements were taken at three positions though the thickness of the steel plate and averaged. The Carbon, Sulfur, Oxygen, and Nitrogen compositions were verified using a Leco Combustion-Fusion mass spectrometer which has higher sensitivity at lower element concentrations. Samples of the steels were mounted in epoxy resin, polished using diamond paste, and then etched with a solution of 2% Nital to increase the contrast of the grain boundaries. Micrographs were taken using an optical microscope.

5.2 Quasi-Static Tensile Testing

Tensile test were performed at low (ambient to -80°C), and high (200°C to 800°C) temperatures. Standard hydraulic test frames were used for all tests.

Tensile testing provides the basic material properties required to evaluate the structural performance of a material. The resulting stress-strain curves provide the modulus of elasticity (E), yield strength (YS), ultimate tensile strength (UTS), and elongation to failure as a function of temperature. This information can be used to fit constitutive material models. These models can then be used in finite element simulations of complex scenarios.

5.2.1 Low-Temperature Tensile Tests

Tensile specimens were machined as close to ¼ thickness of the plate as possible. All low-temperature tensile specimens had a reduced section of at least 31.75mm and diameter of 6.35 mm, and were taken with orientations both RD (plate longitudinal direction, transverse to the tank axis) and TD (plate transverse direction, parallel to the tank axis). Sample temperature was controlled using liquid nitrogen spray. Samples were pulled under displacement control at a constant rate. The strain was measured using a mechanical extensometer with a 25.4 mm gauge length. Force was measured using a load cell. Room temperature tests were conducted in rolling and transverse directions to evaluate the materials' anisotropy. Note that the standard *ASTM E8 – Standard Test Methods for Tension Testing of Metallic Materials*[52] defines room temperature as 50 to 100°F (10 to 37.8°C). The room temperature tests performed for by Canmet MATIALS were conducted between 20 to 25°C.

5.2.2 High-Temperature Tensile Test

For high-temperature tensile and creep tests cylindrical specimens with a reduced section of 38.1-mm length and 6.35-mm diameter cross-section were used. The specimen geometry is shown in Figure 10 and it conforms to the recommendations of the E8 [52] standard for tensile testing of metals, which is called on by the E21-09 [53] standard for high-temperature tensile testing.

Tensile tests were performed at temperatures from 200°C to 800°C. A furnace with ceramic shell heaters (heated with resistance wire heating) was used to elevate the sample temperature in all high-temperature tests. The sample temperature was ramped to the test temperature over a period of 30 min, and then held at this level for another 30 minutes before application of the load. A feedback loop temperature controller was used to maintain a constant temperature throughout the test. A mechanical extensometer with 25.4-mm gauge length was used for the strain measurement for the initial portion of the test [Figure 9]. The extensometer provides accurate strain measurement for determining the modulus and yield point but cannot accommodate high strains over 20%. Since total elongations of greater than 20% were achieved. The extensometer was removed during the tests to prevent damage and the strain measurement was switched to crosshead displacement. The tensile tests were carried out under displacement-control at a constant speed. The initial strain rate was set to 0.12 $\frac{mm}{mm}/min$ for A516-70 and to 0.10 $\frac{mm}{mm}/min$ for TC128B.

Upon test completion, the load and extensometer data were analyzed to provide engineering stress versus engineering strain curves, and true stress versus true strain curves. From these, the yield strength, based on the 0.2% offset method, and the ultimate strength, based on the onset of localization or reduction in applied load, was obtained. A minimum of two repeats were performed at each temperature to ensure repeatability.

Figure 8: MTS test frame with furnace and extensometer

Figure 9: MTS frame close up of furnace and extensometer

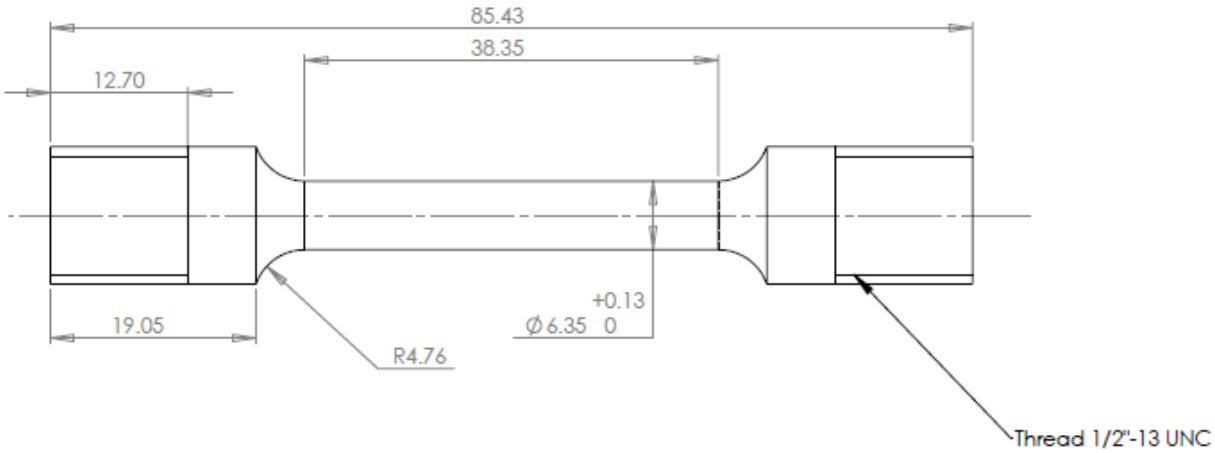

Figure 10: Drawing of tensile specimen. Dimensions in mm except the thread callout which is imperial to match the test frame grips.

5.2.3 Fractography

Images of the tensile specimen fracture surfaces were taken using a NeoScope JCM-5000 SEM. Images were taken with magnifications from 34 to 1000 times. The fractographs show the mechanism of failure.

5.3 Creep Rupture Tests

The creep rupture tests were conducted using the same sample geometry and equipment as the high-temperature tensile tests. The difference between the two types of tests is how the load is applied. The creep tests were performed at constant load. After a sample was held at the test temperature for 60 minutes the load was applied and the sample would elongate by creep and eventually rupture. Basic creep rupture tests only require that the time to rupture be recorded. The tests are often time consuming with very large strains obtained. In this work the strain was recorded using the same procedure as the high-temperature tensile tests with an extensometer at low strains and a Linear Variable Differential Transformer (LVDT) at high strains.

Creep rupture tests provide insight into the rate-dependent properties of a material. Creep deformation differs from metal plasticity in that it occurs below the yield stress of the material. This data is necessary for evaluating the performance of a material that is subjected to sustained high temperatures under load. This data can be used to construct creep models to be implemented in future finite element simulations.

5.4 Charpy Impact Tests

Charpy specimens were full-size and taken with two orientations designated L-T (longitudinal) and T-L (transverse); the orientation code is based on ASTM E1823-10 [49], i.e. L-T is an RD sample and T-L is a TD sample, both notched through-thickness. Charpy specimens were machined as close to ¼ thickness of the plate as possible. A pendulum Charpy machine with maximum available energy of 750 J was used. Specimens were chilled prior to the experiment using a water bath. The temperature was controlled using a mix of liquid nitrogen and ethanol. The temperature was verified using a K-type thermocouple. The test was only considered valid if the sample could be transferred from the bath and fractured within 5 seconds. The energy absorbed by each sample was recorded.

Charpy impact test is a convenient test to perform and the results provide an indication of resistance to fracture initiation and propagation of steels. Charpy test results, as a quality screen parameter, have often been correlated to other more sophisticated toughness tests for design and integrity assessment purposes. Charpy tests also show the ductile to brittle transition temperature (DBTT); the temperature at which a material's failure mechanism switches from ductile to brittle. The AAR provides a Charpy impact specification for tank car steels.

5.5 Dynamic Fracture Toughness: CTOA

Crack-tip opening angle (CTOA) is a fracture parameter to characterize fracture propagation resistance of a steel. Impact DWTT (drop weight tear test) were employed to characterize crack propagation toughness relevant to tank car puncture fractures. Instrumented DWTT tests were performed to obtain the dynamic fracture propagation toughness CTOA using a drop-weight tear test machine (Figure 11).

DWTT specimens were machined from both RD and TD orientations for CTOA tests according to ASTM E3039-16 [54]. DWTT specimens were full-thickness with a plan size of 76 mm × 305 mm and an initial machined notch depth of 10 mm as shown in Figure 12. Standard DWTT tests were performed at an impact rate of 5.1 m/s using a drop-tower. The force exerted on the sample by the dropped weight was recorded using a piezoelectric load cell. Displacement was measured using a LVDT. Intermediate rate DWTT tests were performed at 0.1 m/s using a 110-ton press servo-valve controlled hydraulic press. The load cell capacity of the press is 1000 kN The tup (i.e., impactor) radius of the die in the press, 12.7 mm, was half of the standard tup radius of 25.4 mm (1"). An LVDT on the press was used to measure the deflection of DWTT specimens. A digital image correlation (DIC) camera was used during the intermediate tests to monitor and record surface CTOA, crack length and strain at a rate up to 500 frames/second.
The TC128B DWTT specimens from RD orientation were flattened according to E3039 before testing due to the curvature of the tank car shell. Flattening is standard practice for DWTT specimens taken from pipelines. Pipelines have a much smaller radius of curvature than a tank car shell.

Figure 11: DWTT machine.

Figure 12: DWTT specimen, transverse orientation (arrow shows rolling direction).

5.6 Fracture Toughness SE(B) and SE(T)

Fracture toughness defined as stress intensity factor (K) or J integral, or crack-tip opening displacement (CTOD) (note not to confuse CTOD with CTOA) represents the resistance of tank car steel to crack propagation. Fracture toughness parameters (K, J or CTOD) can be used quantitatively in integrity assessment. Fracture toughness can be measured using single-edge-notched bend (SE(B)) or single-edged-notched tension (SE(T)) tests with either shallow or deep cracks. Different fracture specimen geometries produce different levels of constraint at the crack tip which can lead to different crack growth resistance responses.

Fracture toughness tests were performed using full-thickness SE(B) and SE(T) specimens. The specimens were oriented with length in the TD direction of the plate. SE(B) specimens were of B×2B type (where specimen thickness B is the plate thickness and specimen width is twice the thickness) with integral knife-edges, tested according to ASTM E1820-13[55]. SE(T) specimens were of type B×B, tested according to a draft procedure [56] based on a method developed at CMAT, using the single-clip-gauge option.

Fracture toughness specimens were fatigue pre-cracked to nominal initial crack size a_0 with the target ratios of a_0 to width (W) equal to 0.1 and 0.5 for SE(B) and 0.2 and 0.5 for SE(T) specimens. Fatigue precracking was carried out using a 3-point bend fixture as shown in Figure 13. A clip gauge mounted at the integral knife edges of the specimen was employed to measure crack mouth opening displacement (CMOD) for monitoring crack size. The purpose of fatigue precracking is to produce a sharp crack in each specimen to provide a conservative measure of crack resistance. The fatigue pre-cracked specimens were side-grooved to 7.5% specimen thickness (B) on each side and tested at room temperature (23°C). Crack length was monitored during testing using the unloading compliance method.

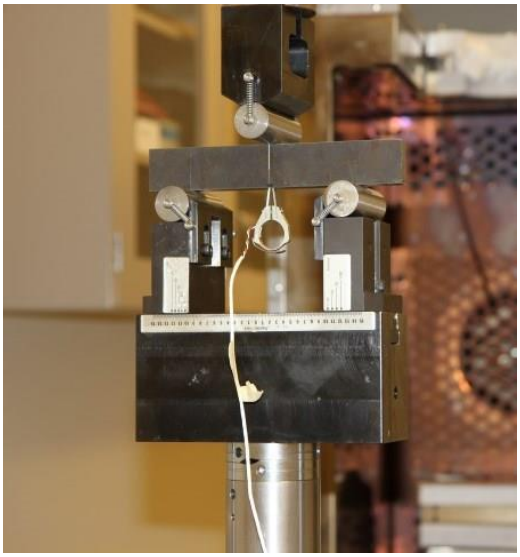

Figure 13: Fatigue precracking of fracture toughness specimen using a 3-point bend fixture.

Figure 14 and Figure 15 display on-going SE(B) and SE(T) tests, specimens and fixtures, respectively. SE(B) specimens were tested using a 3-point bend fixture while SE(T) specimens were clamped rigidly in hydraulic grips and loaded in tension. During testing, load (P), crack mouth opening displacement (CMOD) and load-line displacement (LLD) were monitored to control the test, deduce crack size and derive fracture toughness parameters (i.e., J and crack-tip opening displacement, CTOD); partial unloadings were employed periodically during testing to calculate the crack size.

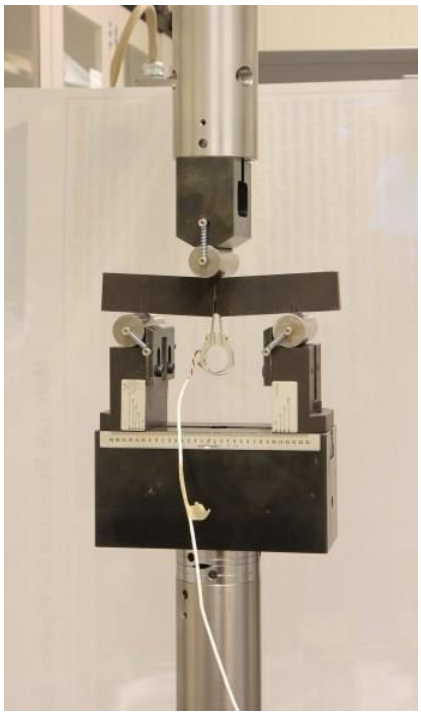

Figure 14: Fracture toughness SE(B) test set-up.

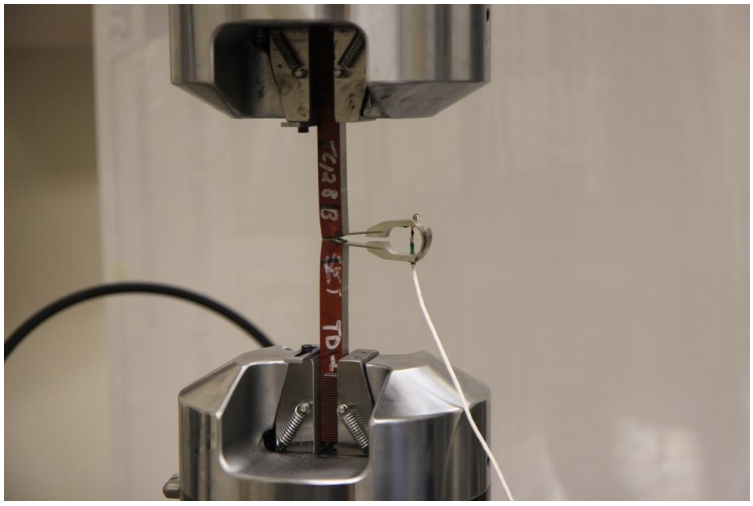

Figure 15: Fracture toughness SE(T) test set-up.

6 EXPERIMENTAL RESULTS

6.1 Composition and Microstructure

The composition of the both steels were analyzed using optical emission spectroscopy and the results are given in Table 6. The maximum permitted elemental values for TC128B [57] and A516-70 [57] are also listed for reference. The composition meets the AAR 2014 specification. The low S and P contents are consistent with current clean steelmaking technology.

Table 6: Chemical composition of the steel and limits for TC128B (wt%) [57]

Element	TC128B		A516-70	
	Spectroscopy analysis	**Maximum permitted in product analysis** [57]	**Spectroscopy analysis**	**Maximum permitted in product analysis** [57]
C	0.19	0.26	0.21	0.25
Mn	1.34	1.00-1.70	0.97	0.79-1.28
P	0.0059	0.25	0.0033	0.025
S	0.0014	0.009	<.001	0.015
Si	0.16	0.13-0.45	0.34	0.15-0.45
V	0.034	0.084	0.0019	0.04 (per ASTM A20 [58])
Cu	0.21	0.35	0.066	0.35
Ni	NA	NA	0.024	0.43 (per ASTM A20 [58])
Cr	NA	NA	0.039	0.34 (per ASTM A20 [58])
Mo	NA	NA	0.013	0.13 (per ASTM A20 [58])
Al	0.032	0.015-0.060	0.033	0.015-0.060
Nb	<0.001	0.03 (per ASTM A20 [58])	<.001	0.03 (per ASTM A20 [58])
Ti	0.0016	0.020	0.0031	0.020
B	0.0002	0.0005	0.0019	0.0005
N	0.0069	0.012	0.0048	0.012
Sn	0.0112	0.020	0.0048	0.020
CE*	0.46	0.55	0.44	0.45
Nb+V+Ti	<0.0366	0.11	<.006	0.11
Cu+Ni+Cr+Mo	0.43	0.65	0.10	0.65
Ti/N	0.23	4.0		4.0

* CE=C+(Mn+Si)/6+(Ni+Cu)/15+(Ni+Mo+V)/5

The microstructures of longitudinal and transverse sections of TC128B taken at ¼ thickness are shown in Figure 16. The polished micrographs illustrate that many inclusions are round in shape

and some are elongated in the rolling direction. The steel has equiaxed grains with grain size approximately 10-20 µm. The constituent phases are ferrite and pearlite in a heavily banded structure. This indicates micro-segregation of C and Mn in the pearlite bands.

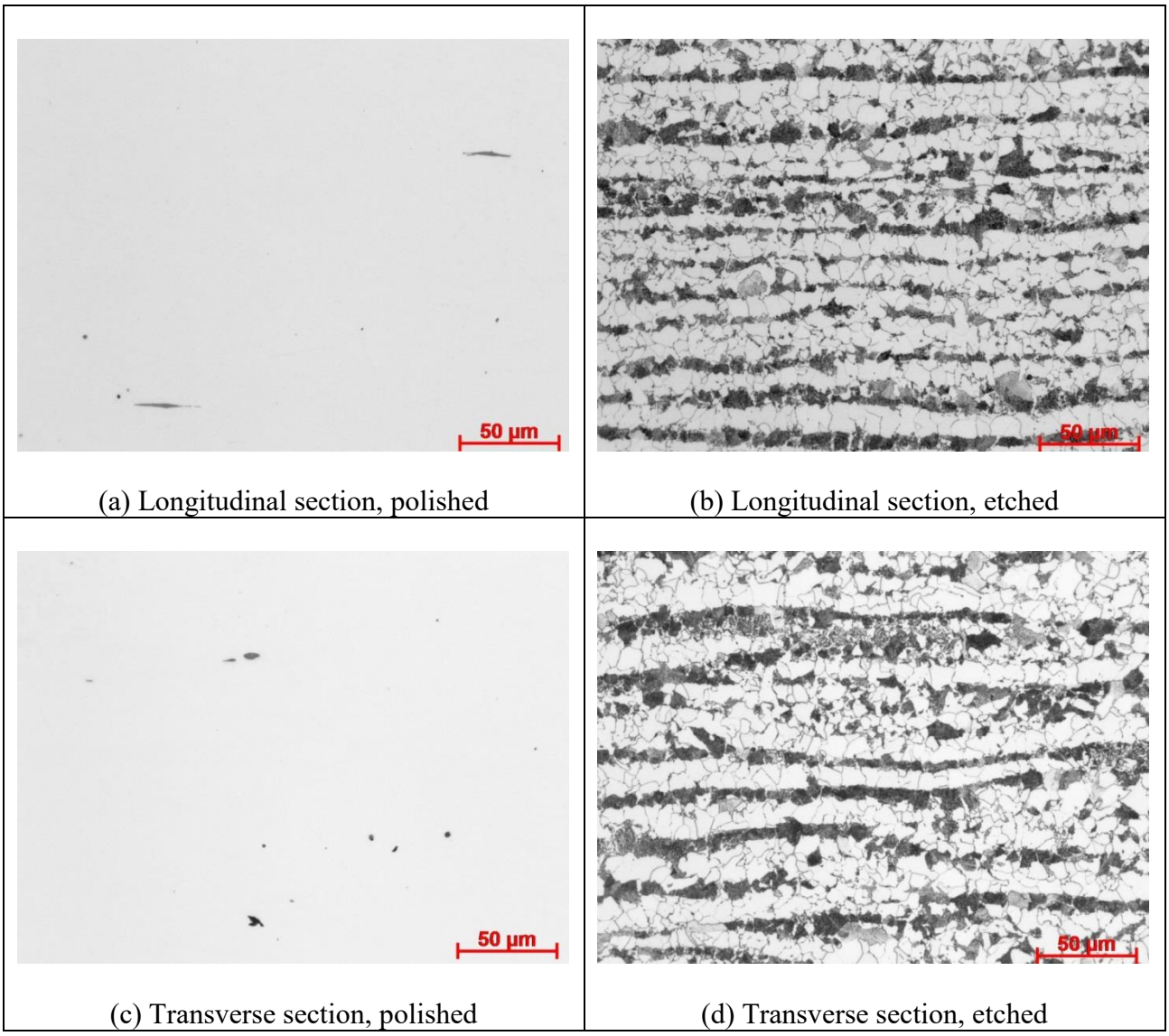

(a) Longitudinal section, polished

(b) Longitudinal section, etched

(c) Transverse section, polished

(d) Transverse section, etched

Figure 16: Polished and etched micrographs of TC128B at ¼ thickness. In the etched micrographs, the white and dark phases are ferrite and pearlite, respectively.

The microstructures of A516-70 are shown in Figure 17. The polished micrograph (Figure 17a) illustrates that many inclusions are close to round in shape or slightly elongated in the rolling direction. The steel has equiaxed grains with grain size approximately 10-30 µm. The constituent phases are ferrite and pearlite with lightly banded structure at ¼ thickness (Figure 17 b and d) but a mixture of bainite and marternsite (arrowed in Figure 17 d) is present close to mid-thickness where heavy banding occurs (Figure 17 c and d). This indicates significant segregation of C and Mn at the mid-thickness of the A516-70 plate.

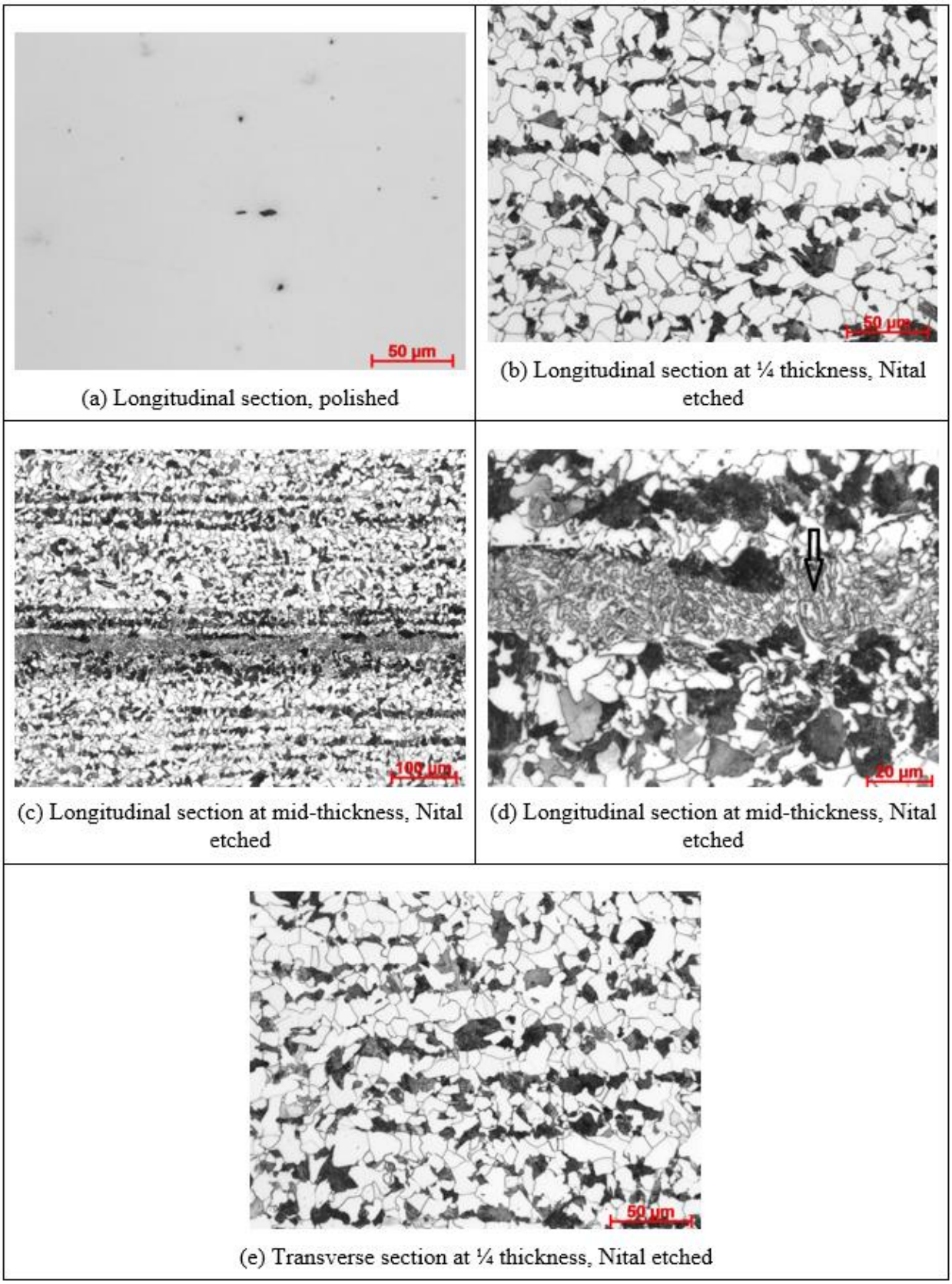

(a) Longitudinal section, polished

(b) Longitudinal section at ¼ thickness, Nital etched

(c) Longitudinal section at mid-thickness, Nital etched

(d) Longitudinal section at mid-thickness, Nital etched

(e) Transverse section at ¼ thickness, Nital etched

Figure 17: Polished and etched micrographs of A516-70 at ¼ thickness and mid-thickness. In the etched micrographs, the white and dark phases are ferrite and pearlite, respectively.

6.2 Quasi-Static Tensile Properties

6.2.1 Low-Temperature

Tensile testing of transverse samples was carried out at RT (room temperature) for displaying anisotropy the results are shown in Figure 18 and Figure 19. Tensile properties of longitudinal and transverse samples are very similar, showing little anisotropy. The tensile stress-strain curves for TC128 and A516-70 are shown in Figure 20 and Figure 21 respectively. Material properties for both steels are given in Table 7 from -80°C to 23°C. Three tensile tests were performed for each set of variables. The tensile properties were consistent (the ratio of standard deviation to average strength ≤ 2%). Strengths increased with decreasing temperature. Elongation and reduction of the area remained very similar in the temperature range of 23°C to -80°C for both materials. Lüders strains were in the range 2-2.93% and increased slightly with decreasing temperature. These characteristics will influence structural behaviour and fracture initiation toughness in a complex manner [59] and should be taken into account; in particular, true stress-strain curves are used as inputs to finite element models for integrity assessment and structural performance. Experimental data can be used to extract true stress and strain only up to the onset of necking.

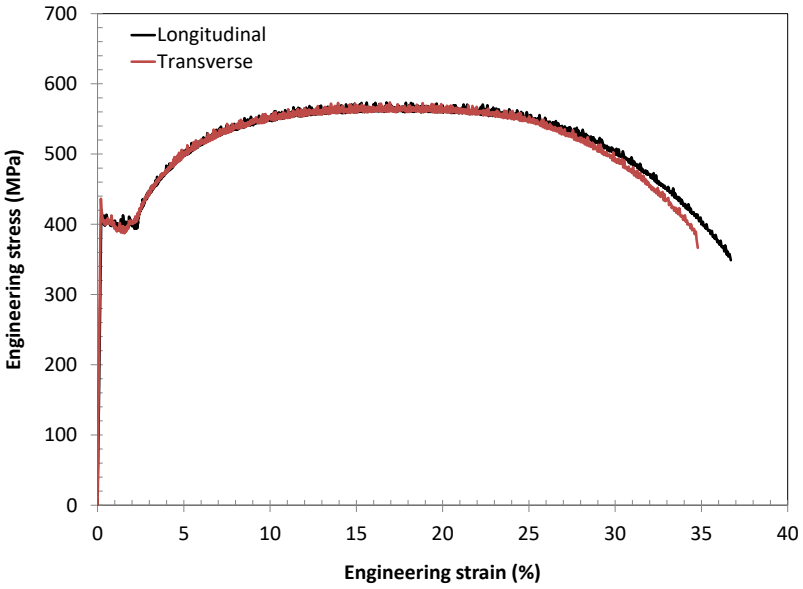

(a) Engineering stress vs. strain curve

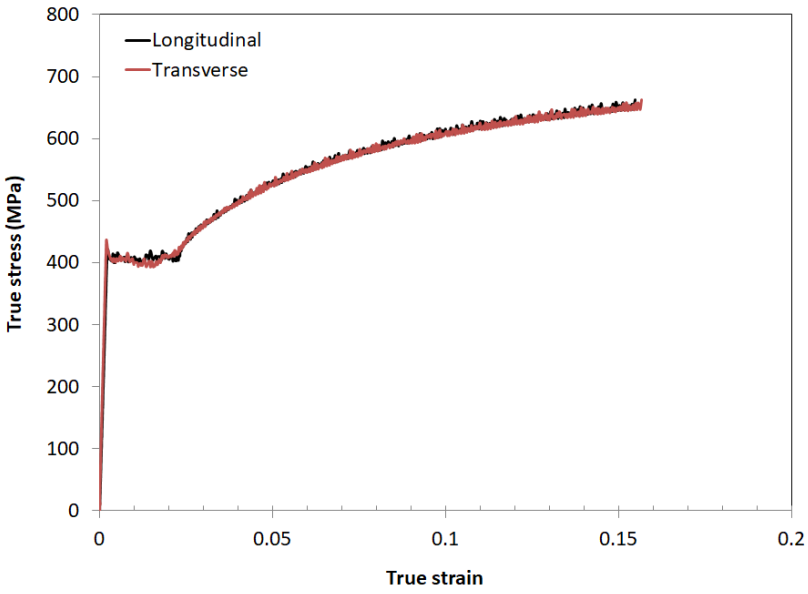

(b) True stress vs. strain curve

Figure 18: Tensile curves of TC128B at 23°C.

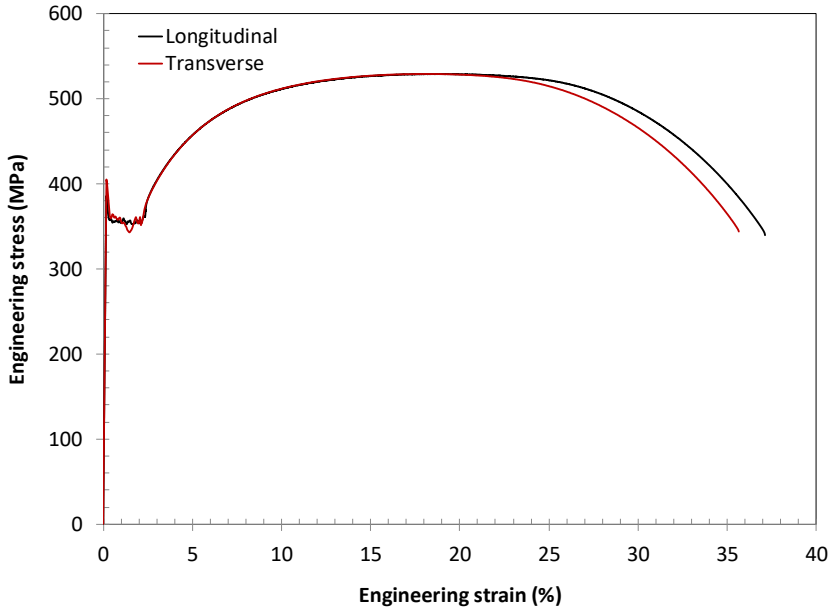

(a) Engineering stress vs. strain curve

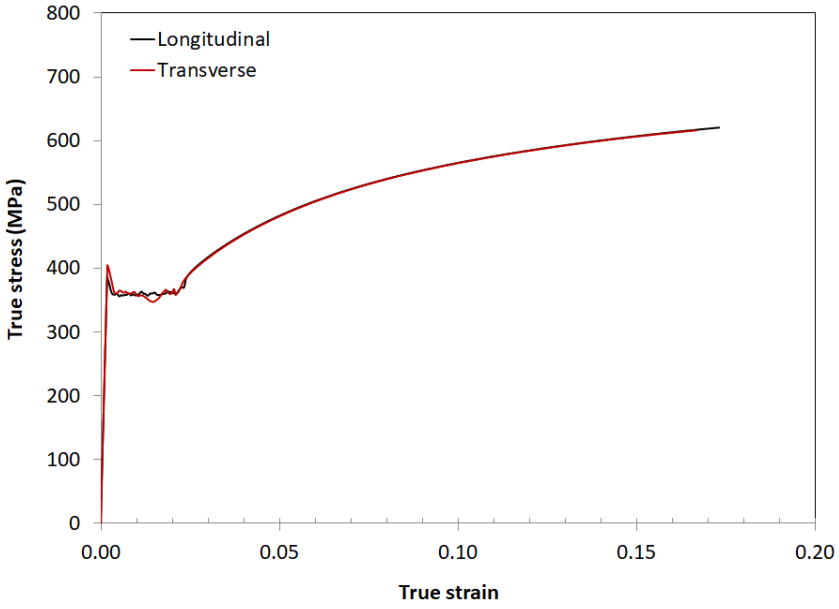

(b) True stress vs. strain curve

Figure 19: Tensile curves of A516-70 at 23°C

Table 7: Average tensile properties of three samples of TC128B and A516-70

Steel/Orientation	T (°C)	σ_y (MPa)	σ_{UTS} (MPa)	E.L. in 25 mm (%)	R.A. (%)	n-value
TC128B/Longitudinal	23	390	574	37	73	0.246
	0	405	589	36	72	0.279
	-20	416	606	35	72	0.288
	-40	437	626	37	71	0.288
	-60	453	654	37	68	0.296
	-80	480	681	38	68	0.290
TC128B/Transverse	23	389	573	35	70	0.270
A516-70/Longitudinal	23	351	529	38	72	0.292
	0	364	557	38	71	0.297
	-20	380	573	37	70	0.304
	-40	399	597	39	69	0.310
	-60	422	622	38	68	0.313
	-80	455	652	38	67	0.307
A516-70/Transverse	23	343	528	35	71	0.294

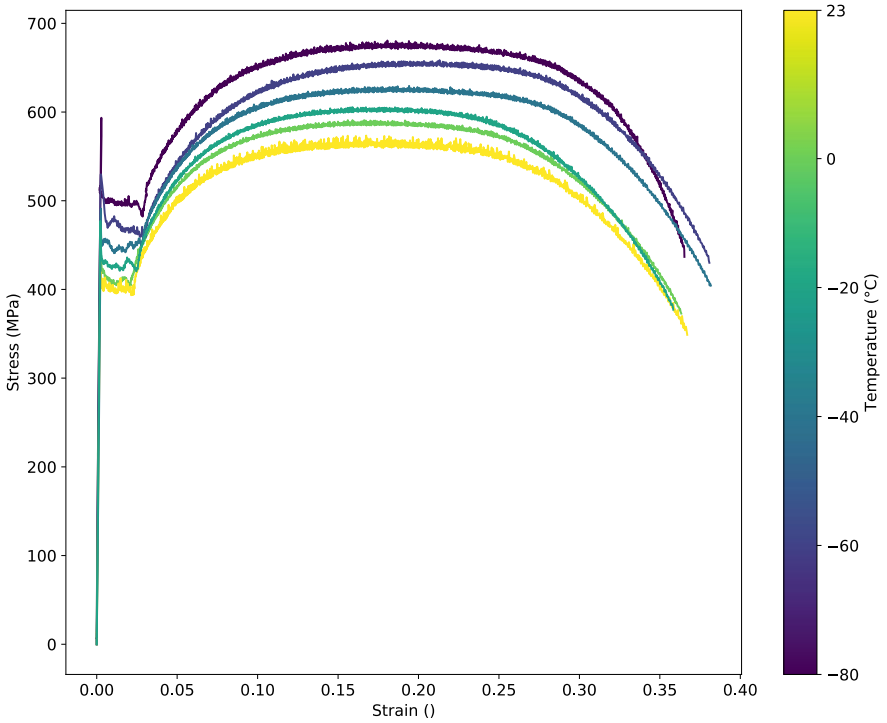

Figure 20: Effect of temperature on stress-strain curves of TC128B.

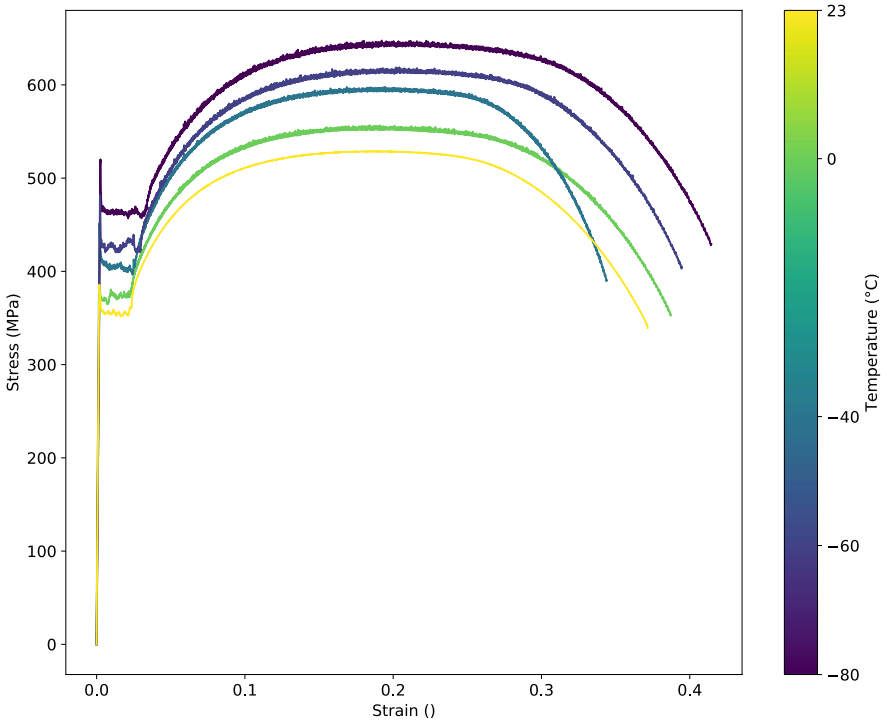

Figure 21: Effect of temperature on stress-strain curves of A516-70

The effect of temperature (and strain rate) on strength is related to thermally activated dislocation movement and can be described by constitutive equations; at temperatures above room temperature the strength of steel may be influenced by other deformation mechanisms (such as strain aging, recovery, and creep). A quantitative description of the dependence of flow stress on strain rate, temperature, and strain is referred to as a "constitutive equation". Since constitutive equations for steels are important for modelling prompted by advanced computational technologies, there has been renewed interest in constitutive equations, for example, in the control of fast ductile fracture of gas pipelines. A physically-based concise constitutive equation for ferritic structural steels was developed at CanmetMATERIALS [60] and has recently been further validated with different types of steels [61]. This constitutive equation has a sound physical basis and fits data at least as well as the constitutive equations used in common commercial finite element analysis software, such as the Johnson-Cook [62] and Zerilli-Armstrong [63] equations. The CMAT constitutive equation [60] is given below:

$$\sigma = \sigma_{(\text{quasi-static},22^{\circ}\text{C})} + \left[27.86 - 0.00393T \ln\left(\frac{10^8}{\dot{\varepsilon}} \right) \right]^2, \tag{1}$$

where σ is in MPa, T is the temperature in Kelvin and $\dot{\varepsilon}$ is the strain rate (s^{-1}). For a quasi-static rate of 3.1×10^{-3} s^{-1}, the constitutive equation is

$$\sigma = \sigma_{(\text{quasi-static},22^{\circ}\text{C})} + \left(27.86 - 0.09509T\right)^2 \tag{2}$$

It has been shown that the difference between any two true stress-strain curves at different temperatures for a given structural steel is approximately independent of strain (i.e., the true stress-strain curves are simply shifted along the stress axis) [60], [61]. Thus, the flow curves at different temperatures and strain rates for a given steel can be obtained simply by adding the thermal component (the second term in equations (1) and (2) to a flow curve (σ(ε)) obtained at room temperature at a quasi-static loading rate. Equation (2) provides a good fit to the data obtained in this work (Figure 22). Note that the accuracy of the equation is usually within 30 MPa of the measured strength data [60]. These equations were developed and validated for low-temperatures (25°C to -80°C for the data presented) a different approach is used at higher temperatures.

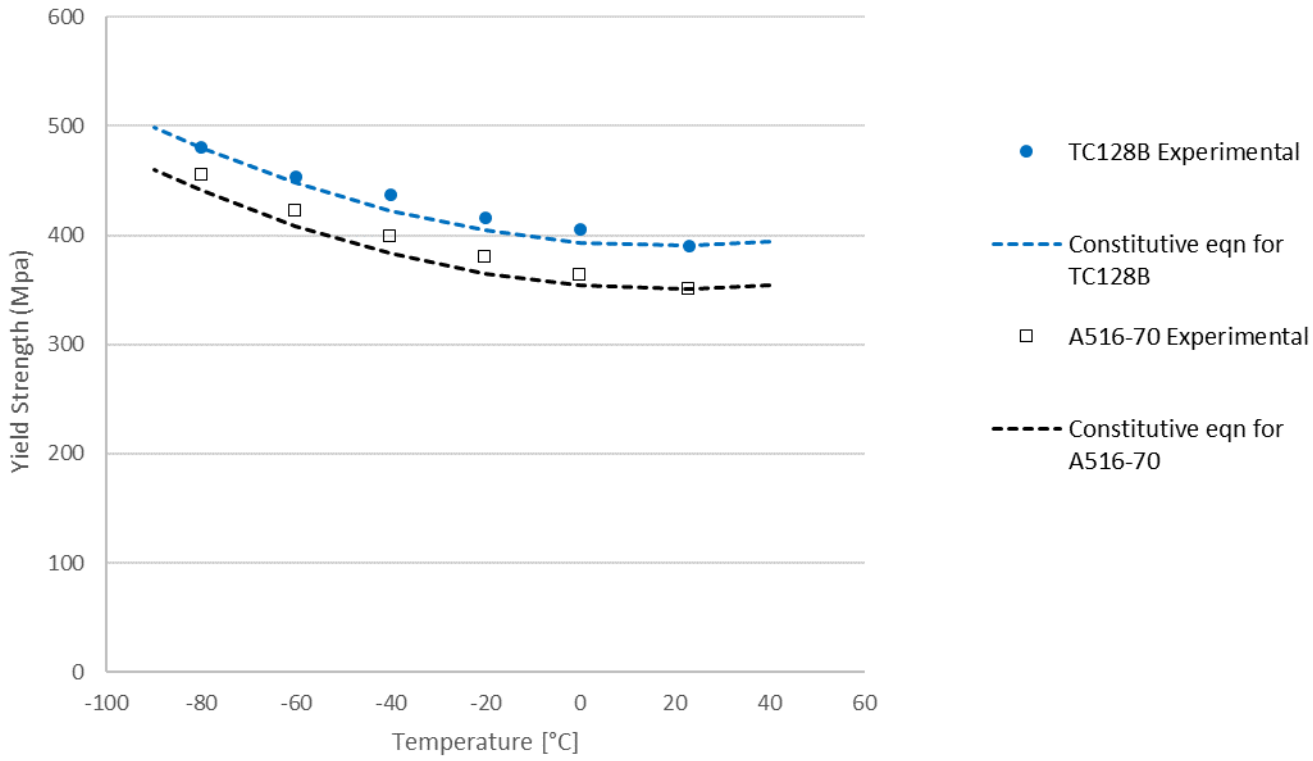

Figure 22: Effect of temperature on longitudinal yield strength of TC128B in blue and A516-70 in black.

Using equation (1), the increase in flow stress at any given strain was calculated as a function of temperature for three strain rates and given in Table 8. The increase in strength (thermal stress) with decreasing temperature increases with strain rate. (For reference, the strain rate experienced during automobile collisions is usually taken as between 100 and 500 s^{-1}.)

Table 8: Strength increase relative to quasi-static strength at 23°C as a function of temperature and strain rate, based on Eq. (9)

T (°C)	**Strength Increase (MPa)**		
	Quasi-static rate	**100 s^{-1}**	**500 s^{-1}**
23	0	139	187
0	3	170	218
-20	14	199	247
-40	32	231	278
-45.6	39	241	287
-50	44	248	295
-60	57	266	311
-80	90	302	346

6.2.2 High-Temperature Tensile Behaviour

The engineering stress-strain curves for TC128B and A516-70 are shown in

Figure 23 and Figure 24 respectively. The yield strength, UTS, and modulus for all tests are summarized in Table 9. It bears stressing that there are two values of UTS listed in the table. The UTS (ASTM) corresponds to the maximum load in the test divided by the original area; this definition conforms to the E8 Standard[52]. The UTS (true) is the maximum true stress; that is, the stress at onset of localization. While the former is computed per the recommendation in the Standard, the latter is required for material model development.

Most tests were conducted on samples oriented in the transverse direction (TD) which was expected to be weaker than the rolling direction (RD) however Figure 18 and Figure 19 show that both TC128B and A516-70 exhibit virtually no anisotropy at room temperature (RT) as discussed previously. Some of the TC128B test were conducted in the RD due to a shortage of TD samples at the time of testing.

Both steels displayed display discontinuous yielding at RT and to a lesser extent at 200^{o}C. The stress-strain curves in Figure 25 are truncated at 10% strain to better show the serrated yielding. Upper and lower yield points are also apparent. On account of the annealing effect of the higher temperatures, the dislocations present in the shell are annihilated and the discontinuous yielding is not seen.

As expected, there is a decrease in yield strength with increasing temperature for both steels. In contrast, the elongation prior to failure changes little between RT and 400^{o}C. It increases greatly from 400^{o}C to 800^{o}C.

There was some concern that the oxidation of the samples tested at higher temperatures was a significant contributor to the loss of strength. Figure 27 show samples tested at 200°C, 400°C, 500°C, 600°C, 700°C, and 800°C. Black oxide can clearly be seen on the outside of the high-temperature samples. The TC128B 800°C tests were repeated in an inert Argon atmosphere and the results are shown in Figure 26. There was no significant difference between the tests conducted in air and the tests conducted in argon. Each sample was also weighed prior to testing. After the tests were complete the oxide layer was chemically removed and the sample was weighed again. The total mass loss was less than 1% for all 800°C samples. No further tests were conducted in argon due to the increased expense of the argon gas.

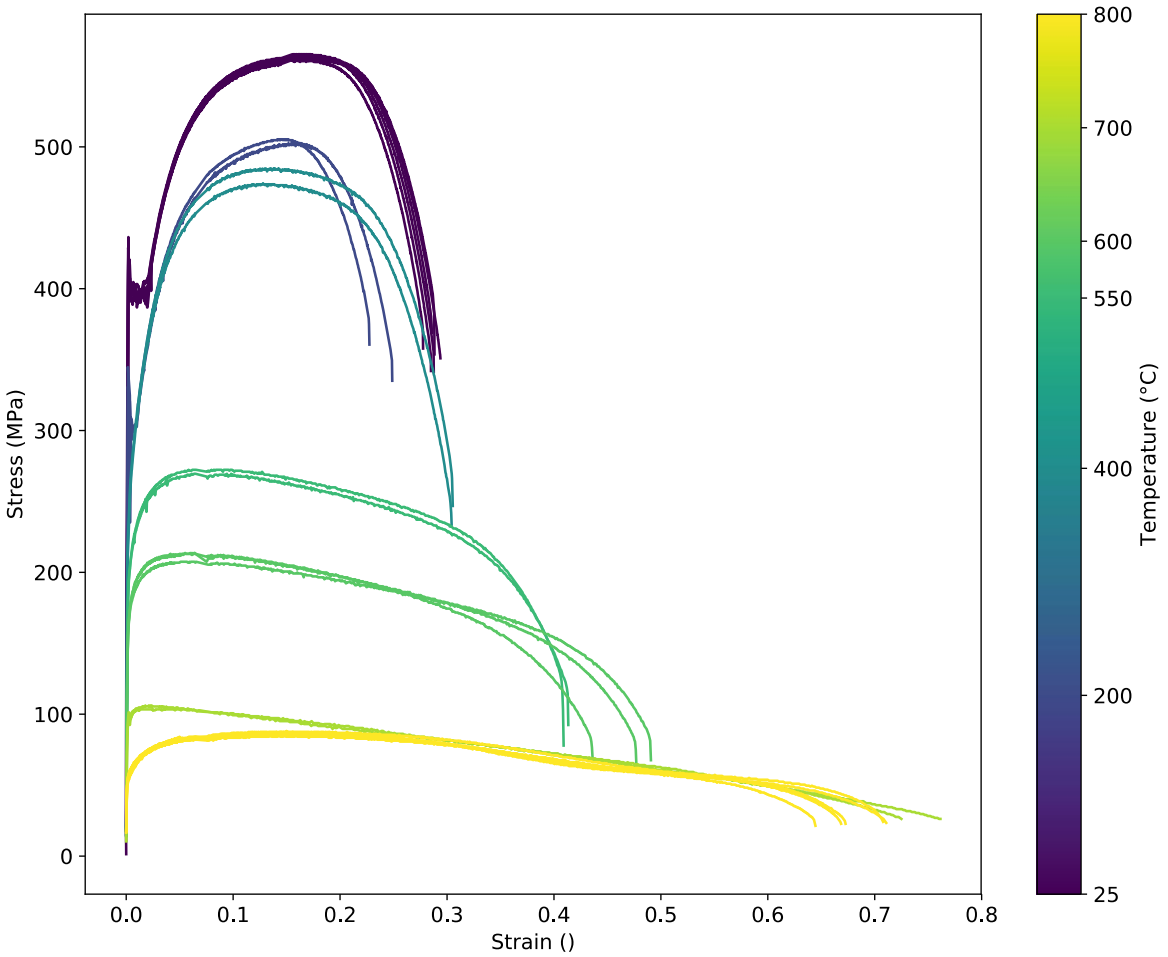

Figure 23: Engineering stress strain curves for TC128B

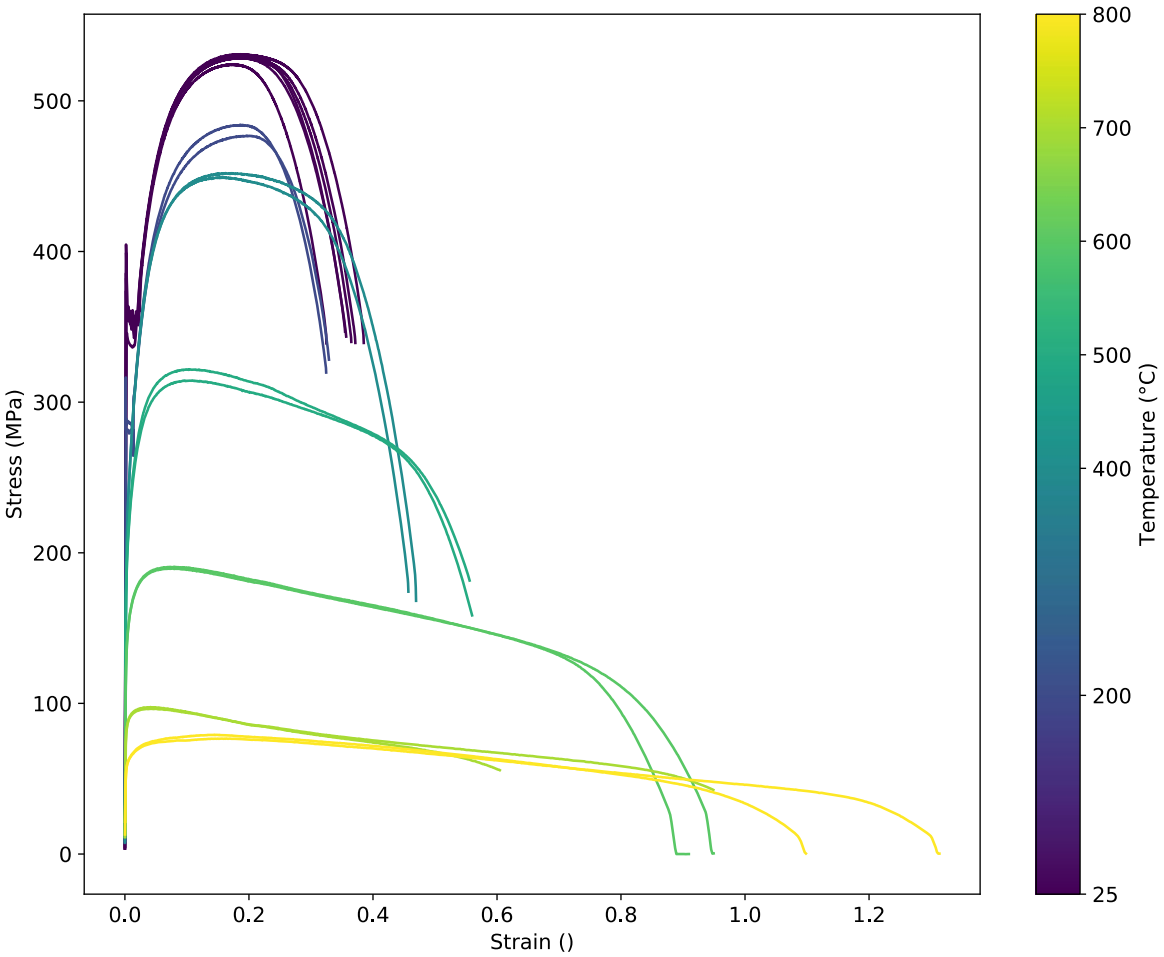

Figure 24: Engineering stress strain curves for A516-70

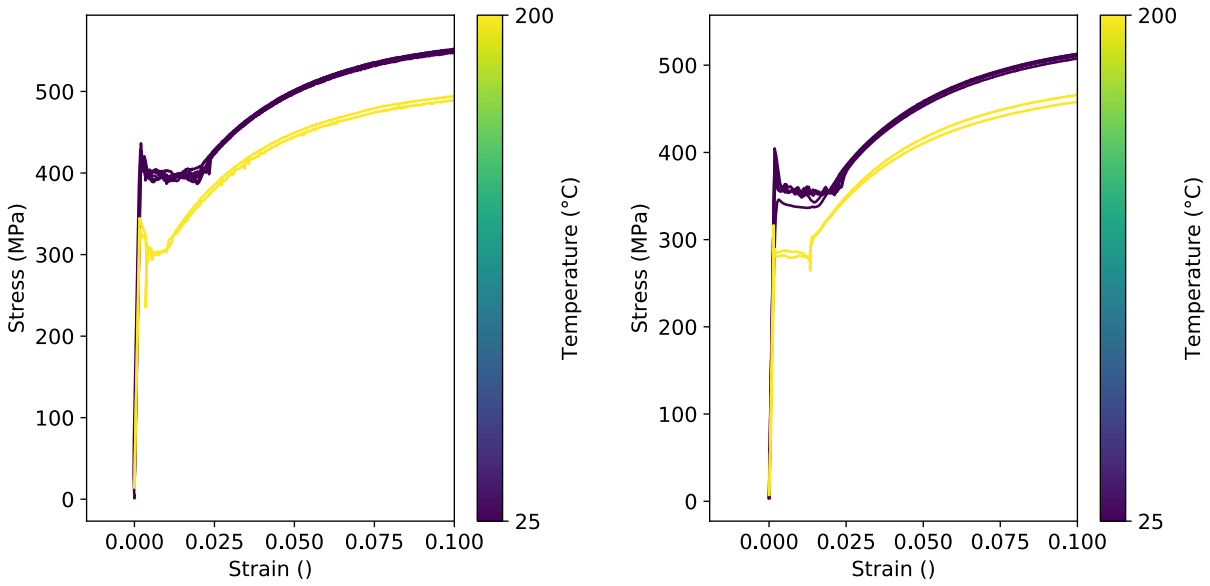

Figure 25: Engineering stress strain curves for TC128B (left) and A516-70 (right) at RT and 200°C showing discontinuous yielding

Table 9: Listing of modulus, yield and strength properties for TC 128 B and A516-70.

Steel	Test ID.	Temperature [ºC]	Orientation	0.2% Offset	UTS (ASTM)	UTS (true)	Young's Modulus
		[°C]		[MPa]	[MPa]	[MPa]	[GPa]
TC128B	105	20	TD	396	565	671	211
	111		RD	407	562	673	228
	129		TD	317	500	526	199
	135		RD	310	503	546	200
	104	200	TD	317	500	526	211
	106		TD	310	503	546	174
	108		TD	307	500	509	211
	110	400	TD	258	486	569	181
	112		TD	251	475	553	175
	114		TD	258	482	564	172
	131	550	TD	258	486	569	140
	137		TD	251	475	553	145
	116	600	TD	176	214	237	124
	117		TD	172	207	234	138
	118		TD	172	214	237	130
	133	700	TD	176	214	237	97
	139		TD	172	207	234	108
	119	800	TD	55	86	105	39
	120		TD	59	90	107	41
	121		TD	59	86	102	43
A516-70	RD 1 RT	25	RD	357	529	629	215
	RD 2 RT		RD	355	528	626	210
	RD 3 RT		RD	362	531	631	210
	TD 1 RT		TD	344	531	630	199
	TD 2 RT		TD	362	529	625	220
	TD 3 RT		TD	356	524	614	206
	200C No 1	200	TD	281	477	573	212
	200C No 2		TD	286	484	575	185
	400C No 1	400	TD	214	452	525	144
	400C No 2		TD	215	449	519	172
	500C No 1	500	TD	193	314	348	156
	500C No 2		TD	199	322	355	153
	600C No 1	600	TD	142	191	206	107
	600C No 2		TD	140	190	204	120
	700C No 1	700	TD	84	96	101	70
	700C No 2		TD	85	98	102	81
	800C No 1	800	TD	59	77	90	43
	800C No 2		TD	59	79	90	57

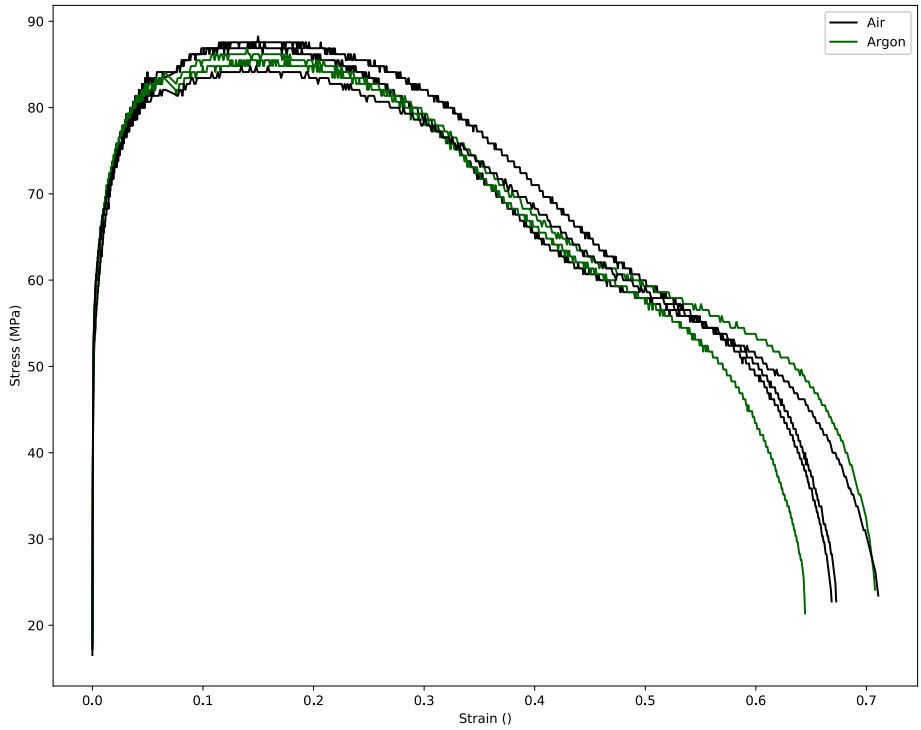

Figure 26: Engineering stress strain curves for TC128B at 800°C. Curves are shown for tests in argon and atmosphere.

Figure 27: Tensile specimens from left to right; untested, 200°C, 400°C, 500°C, 600°C, 700°C, 800°C.

6.2.3 Fractography

The fracture surfaces of 200°C and 600°C TC128 samples are shown in Figure 28. 200°C, 600°C, and 800°C fracture surfaces of A516-70 are shown in Figure 29. As was expected void driven ductile failure occurred at all temperatures. The size of the voids at failure increased with temperature. The greater elongation to failure at elevated temperatures allowed greater void coalescence and growth. The high-temperature samples had much greater reduction in area at the failure point.

The 800°C surface is darker with more rounded edges because the surface oxidized quickly after failure.

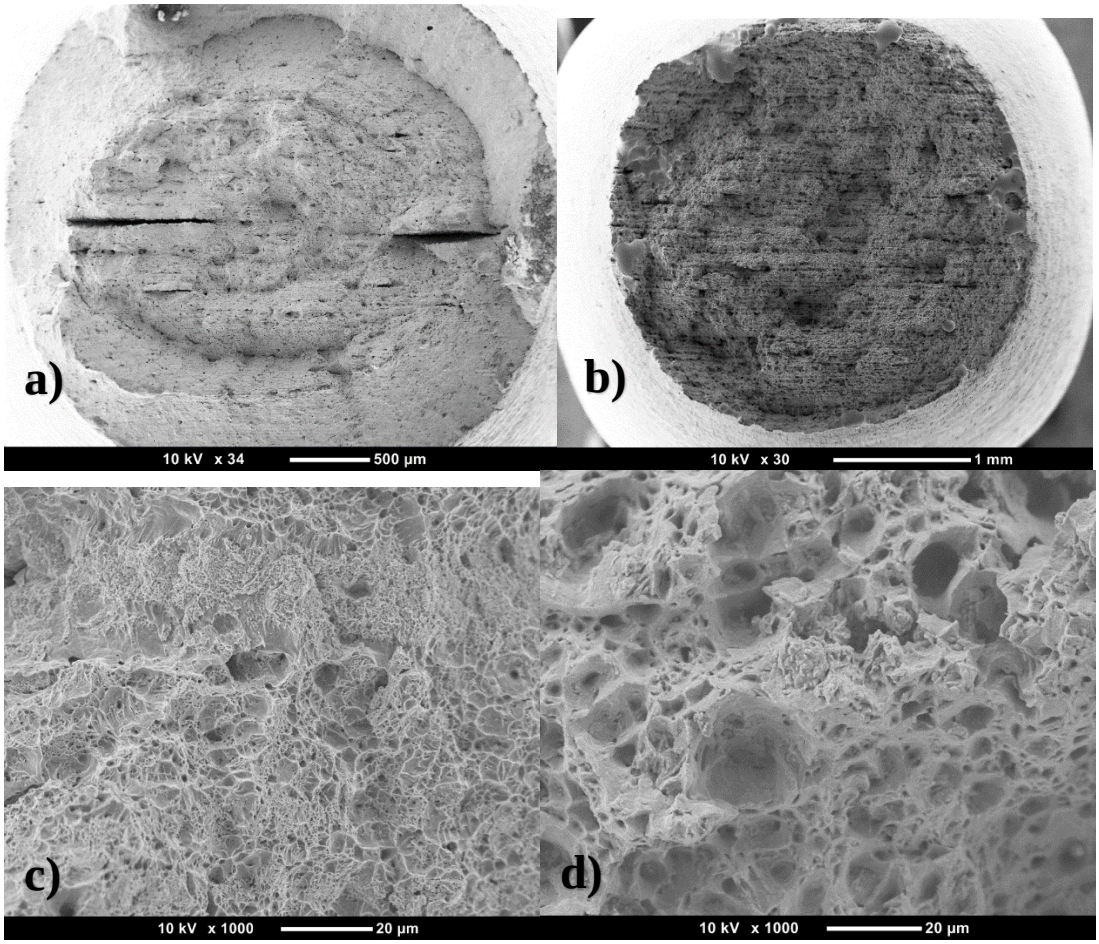

Figure 28: SEM fractographs at RT are shown in a) and c). 600°C fractographs are shown in b) and d)

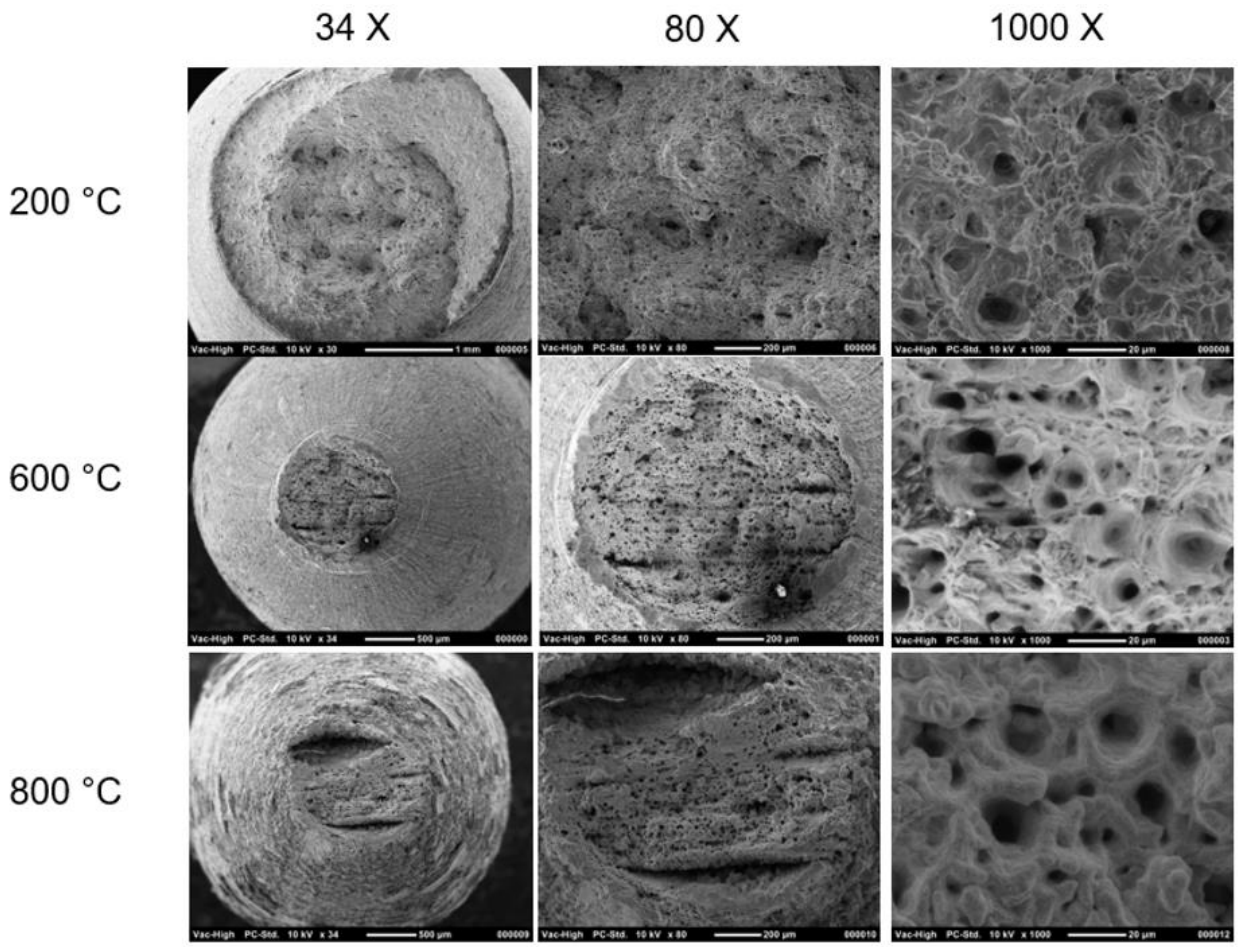

Figure 29: SEM fractographs of TC128B at 200°C, 600°C, and 800°C. Magnifications of 34, 80 and 1000 times are shown for each case.

6.3 Creep Rupture Test Results

The desired outcome of the creep rupture tests was to acquire rupture times in the range of 1, 10 and 100 minutes at temperatures of 400°C to 800°C. A significant range in rupture times is necessary to create an accurate model of the material's creep behaviour. One challenge of creep rupture test is that the constant load must be chosen in advance. Appropriate loads can be estimated based on the results of tensile tests and previous creep tests. If the initial load chosen is too low the sample may not fail in a reasonable timeframe. Achieving a creep rupture test with a specific time-to-failure is difficult without prior knowledge of the material's creep behaviour. The creep rate of both materials at 400°C was too slow to result in failure in a reasonable time therefore no data was recorded at that temperature. The lowest temperatures with successful creep rupture tests were 550°C for TC128B and 500°C for A516-70. The complete set of tests performed on TC128B is summarized in Table 10 below. Successful tests were obtained at 550, 600, 700, and 800°C. The results for A516-70 are given in Table 11. A516-70 tests were completed at 500, 600, 700, and 800°C. The strain evolution for the TC128B and A516-70 rupture tests are shown in Figure 30 and Figure 31 respectively. Initially, there is a linear portion which combines the primary and secondary portion of the creep history, and there is an accelerated portion with increasing strain rate leading to failure where there is an un-bounded strain increase. Time corresponding to the un-bounded increase in strain is the rupture time.

Creep rupture data can be summarized by plotting initial applied stress vs time to rupture, with time on a logarithmic scale, for each temperature tested as shown in Figure 32 and Figure 33. Logarithmic curve fits were added. These plots provide an easy visualization of temperature and load effects on creep rate. As the temperature is increased the load required to achieve rupture in a given time decreases drastically.

It can be challenging to select appropriate initial stresses for these creep-rupture tests, for example, all of the 700C specimens for TC128B failed in less than 17 minutes. Even though it would have been better to have test data at lower applied stresses and longer rupture times, the data shown does fit nicely in the trend established by the other data plotted in figure 32.

Table 10: Summary of TC128B creep rupture tests.

Sample #	Sample ID	Temp (°C)	Load (KN)	Time to Rupture (min)	Specimen Fractured?
206133	C3	800	1.64	68.1	Yes
206134	C4		1.73	65.5	Yes
206136	C7		0.72	115.0	No
206137	C8		1.17	115.0	No
206141	C12		1.55	94.9	Yes
206144	C15		1.73	51.6	Yes
206145	C16		1.64	71.6	Yes
206146	C17		1.55	90.3	Yes
249138	C25	700	3.0	3.5	No
249140	C26		2.8	5.5	No
249141	C21		2.6	9.0	Yes
249142	C27		2.5	12.6	Yes
249147	T23		3.0	3.8	Yes
249148	T27		2.8	6.1	Yes
249149	T26		2.6	8.7	Yes
249150	T14		2.5	10.6	Yes
206138	C9	600	5.20	24.7	Yes
206139	C10		4.93	32.7	Yes
206142	C13		4.66	58.6	Yes
206147	C18		5.20	16.7	Yes
206148	C19		4.93	26.9	Yes
206162	C20		4.66	42.4	Yes
249130	C22	550	6.1	118.8	Yes
249132	C23		5.8	199.8	No
249134	C24		5.5	200	No
249136	T21		5.2	200	No
249143	L10		6.1	124	No
249144	L8		5.8	183.6	Yes
249145	L9		6.3	92.4	Yes
249146	L4		6.4	71.6	No
206143	C14	500	6.47	200	No
206140	C11	400	7.70	200	No

Table 11: Summary of A516-70 creep rupture tests.

ID	Temp (°C)	Load (KN)	Time to Rupture (min)	Specimen Fractured?
800C-110%-No1	800	2.041	9.17	Yes
800C-110%-No2		2.041	10.60	Yes
800C-100%-No1		1.856	18.38	Yes
800C-95%-No1		1.763	25.12	Yes
800C-95%-No2		1.769	26.75	Yes
800C-90%-No1		1.675	30.90	Yes
800C-80%-No1		1.494	68.20	Yes
800C-80%-No2		1.494	75.67	Yes
700C-100%-No1	700	2.840	3.60	Yes
700C-100%-No2		2.840	3.26	Yes
700C-100%-No3		2.849	3.97	Yes
700C-90%-No1		2.556	8.10	Yes
700C-85%-No1		2.414	10.48	Yes
700C-85%-No2		2.414	10.58	Yes
700C-70%-No1		1.994	36.15	Yes
700C-60%-No1		1.709	73.78	Yes
700C-60%-No2		1.709	76.83	Yes
600C-115%-No1	600	5.116	8.44	Yes
600C-115%-No2		5.116	9.51	Yes
600C-100%-No1		4.449	23.02	Yes
600C-100%-No2		4.435	29.65	Yes
600C-85%-No1		3.782	72.02	Yes
600C-85%-No2		3.782	74.66	Yes
500C-140%-No1	500	8.757	16.47	Yes
500C-140%-No2		8.757	20.56	Yes
500C-125%-No1		7.731	88.95	Yes
500C-125%-No2		7.811	81.72	Yes
500C-100%-No1		6.184	896.83	Yes
500C-100%-No2		6.165	825.09	Yes
500C-100%-No3		6.165	803.38	Yes

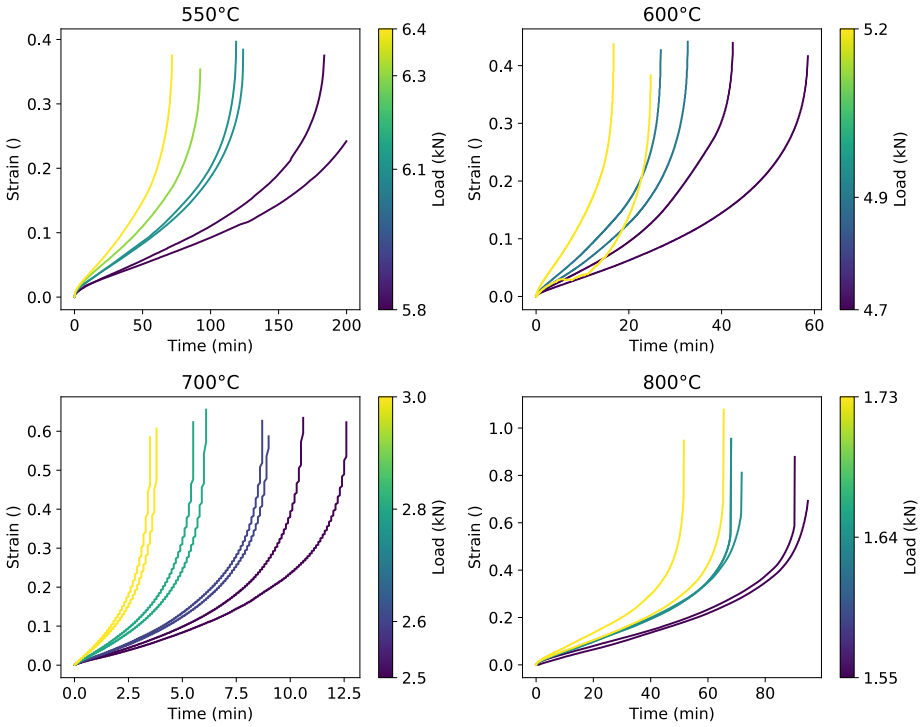

Figure 30: Strain vs Time curves for TC128B creep rupture tests

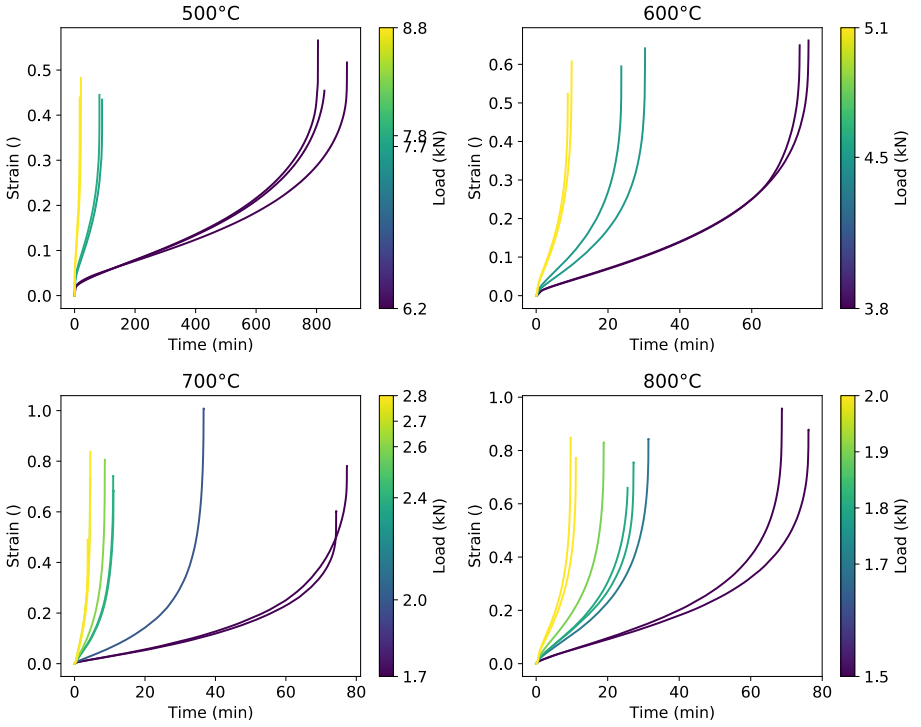

Figure 31: Strain vs Time curves for A516-70 creep rupture tests

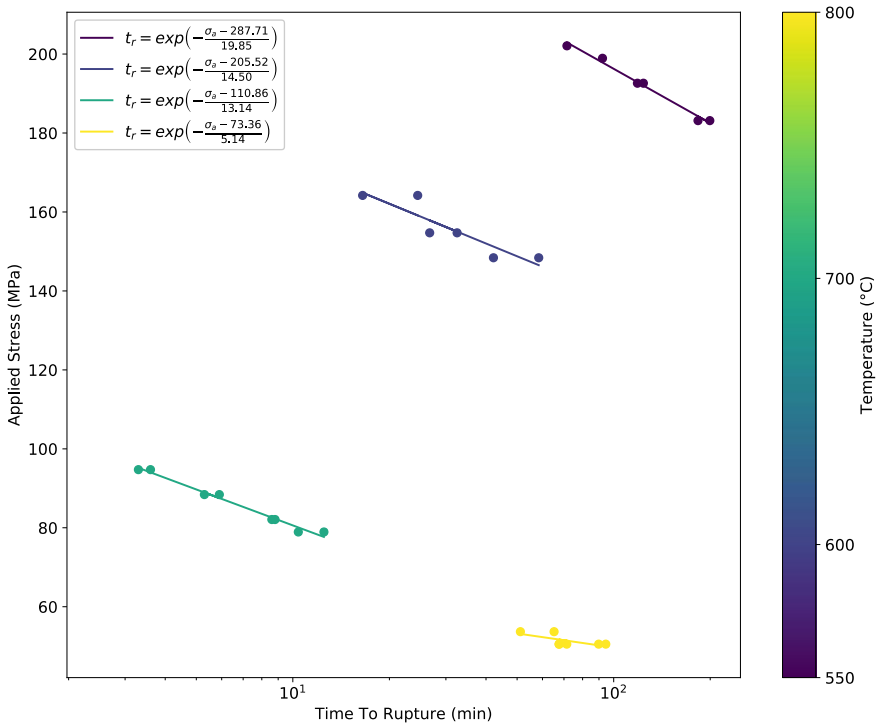

Figure 32: Time to rupture vs initial applied stress for TC128B with logarithmic fits

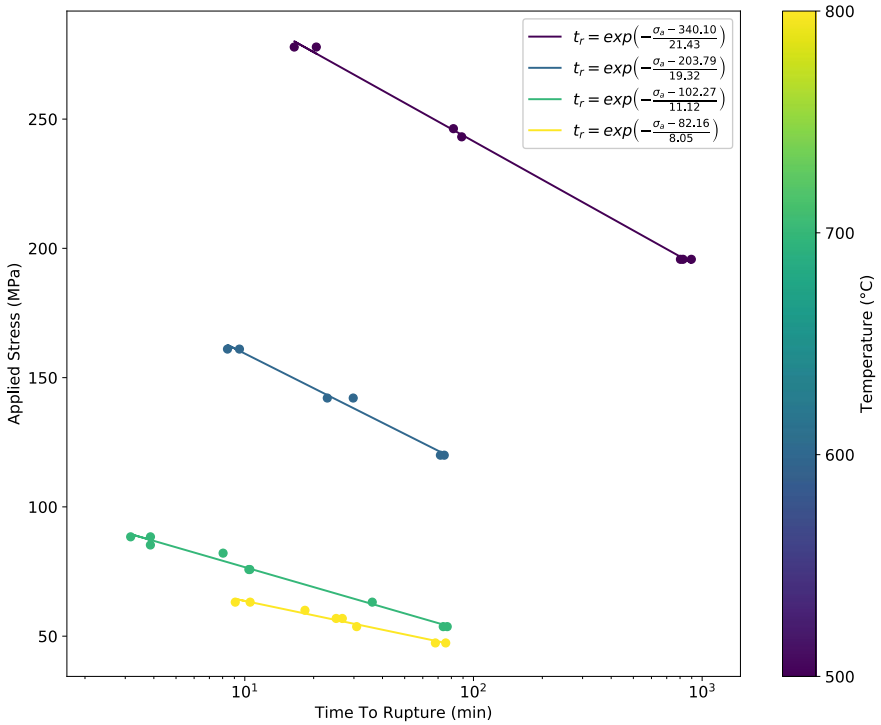

Figure 33: Time to rupture vs initial applied stress for A516-70 with logarithmic fits

Fracture Results

6.3.1 Charpy Properties

Charpy toughness is the only required toughness included in the AAR tank car steel specifications [45], [57] and TP14877 [64]. For pressure tank cars, the CVN requirements are 20.3 J (min. average for three longitudinal specimens, 13.6 J min. for one specimen) at -45.6°C [57], [64]. The specified 20.3 J for CVN is an empirical value for avoiding brittle fracture in steel structures. High CVN and low Charpy ductile-to-brittle transition temperature (DBTT) are desired because ductile fracture is normally ensured if the design temperature is higher than the DBTT and high CVN indicates good dynamic fracture toughness (i.e., resistance to fracture under dynamic loading conditions).

Charpy tests were performed at temperatures between 25°C and -79°C. Results are given for TC128B in Table 12 and for A516-70 in Table 13. The results are plotted as a function of temperature in Figure 34 and Figure 35. The CVN values decrease gradually with decreasing temperature. Longitudinal CVN values (crack propagation perpendicular to the rolling direction) are higher than transverse ones for both steels. The variation with orientation (or anisotropy) is consistent with the observation of some elongated inclusions along the rolling direction (Figure 16a, Figure 17a). The variation is not due to tensile anisotropy because it is small. At -60°C or lower, the difference of CVN between longitudinal and transverse samples diminished for TC128B but the scatters were large indicating that the steel is in ductile-to-brittle transition region. At high CVN range, ductile fracture is dominant and CVN is related to plastic deformation, void nucleation and growth and fracture across the elongated inclusions. At low CVN region, cleavage fracture is the main fracture mechanism and it depends on breakage of atomic bonding. Hence, the anisotropy is more obvious in high-temperature (CVN) region. The CVN data were fitted by the following equation [65], [66]:

$$CVN = C_1 + C_2 \tanh\left(\frac{T - T_0}{C_3}\right) \qquad (3)$$

Where:

- T is the temperature (°C)
- C_1, C_2, T_o and C_3 are regression parameters determined by least-squares analysis

The fitting curves are shown in Figure 34 and Figure 35. The fitting constants and Charpy properties at representative temperatures are given in Table 14. These values are comparable to those of contemporary X52 pipe steels (150-400 J) [67]. CVN for longitudinal samples of TC128B (calculated from Eq. (3)) and A516-70 (experimental) at -46°C is 81 J and is 111 J respectively; both are higher than the required 20.3 J. The 20 J transition temperatures for both longitudinal and transverse orientations of TC128B are approximately the same at -83°C. The 20 J transition temperatures for both longitudinal and transverse orientations of A516-70 are close at -77°C and -73°C, respectively. The good CVN values at -46°C and low 20 J transition temperatures are consistent with current steelmaking technology and are much better than CVN of previous tank car steels before 1989[1].

Table 12: Charpy absorbed energy (CVN) of TC128B: mean average (and individual)

T (°C)	CVN (J)	
	Longitudinal (RD)	Transverse (TD)
24	269 (276,269,263)	205 (219,197,200)
0	232 (239,235,223)	163 (157,166,166)
-20	165 (165,173,158)	140 (135,145,139)
-40	97 (77,128,87)	66 (81,53,64)
-60	56 (27,71,60)	53 (61,50,48)
-79	22 (21,18,27)	20 (15,31,13)

Table 13: Charpy absorbed energy (CVN) of A516-70: mean average (and individual)

T (°C)	CVN (J)	
	Longitudinal (RD)	Transverse (TD)
25	221 (218,225,220)	203 (195,213,202)
-20	164 (163,174,154)	140 (163,138,118)
-46	111 (86,131,115)	96 (99,98,92)
-60	48 (52,37,55)	39 (25,46,45)
-77	17 (15,24,11)	10 (11,9,11)

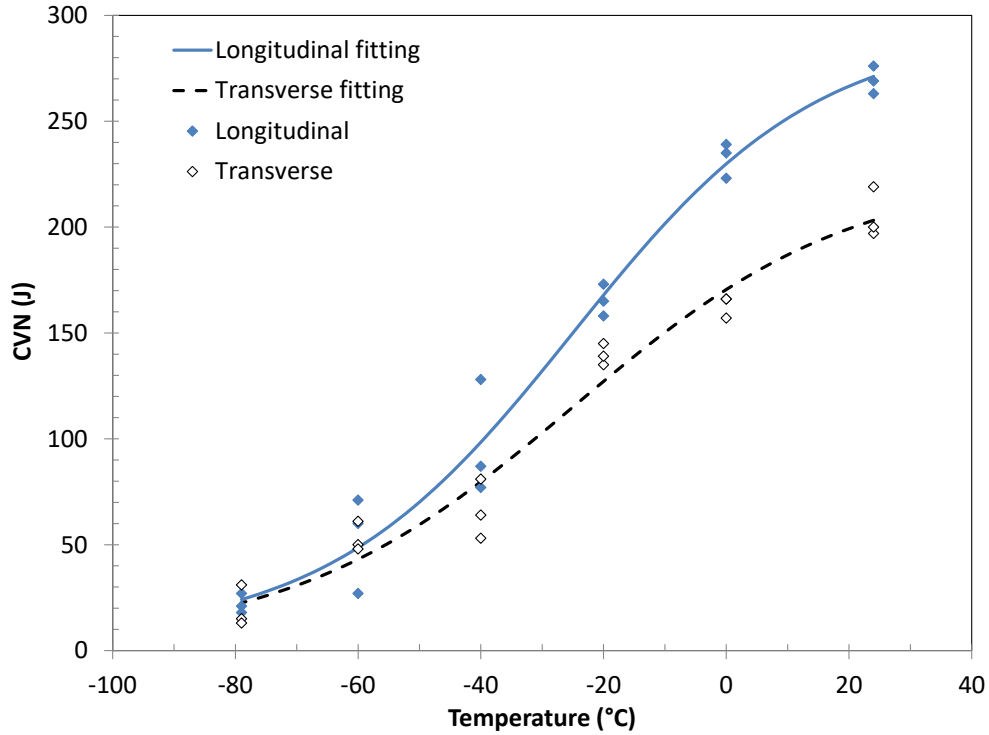

Figure 34: Charpy transition curve of TC128B.

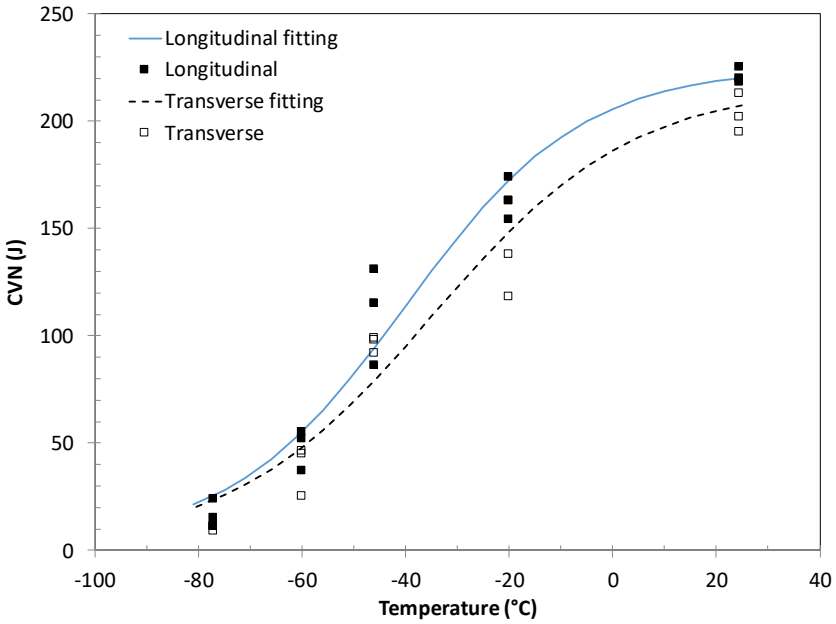

Figure 35: Charpy transition curves of A516-70

Table 14: Fitting constants and Charpy properties of TC128B and A516-70 based on fitted curves

Steel	Orientation	Fitting constants Eq. (3)				CVN at -46°C (J)	20 J DBTT (°C)
		C_1	C_2	T_o	C_3		
TC128B	Longitudinal	150	144	-25	40	81	-84
TC128B	Transverse	115	112	-25	46	67	-83
A516-70	Longitudinal	114	111	-35	34	95	-82
A516-70	Transverse	109	108	-35	39	79	-81

6.3.2 Dynamic Fracture Propagation Toughness – CTOA

As found in the literature review [1], during tank car accidents under impact, long fractures of tank car shells were observed. The extension of a large long fracture of tank car steel is related to fracture propagation and hence the appropriate parameter, CTOA. The fracture driving force in this case is mainly the impact force but not internal pressure.

Figure 37 shows load (P) vs. deflection or load-line displacement (Δ) curves of the impact tests for TC128B; the curves show good repeatability. The load (P) vs. deflection results for A516-70 are shown in Figure 38. DWTT specimens fractured in a shear mode (referred to as "slant fracture" because the fracture surface is approximately 45° to the plate surface); an example of a

tested DWTT specimen is shown in Figure 36. The transition from “thumb-nail” flat fracture to slant fracture started just after initiation.

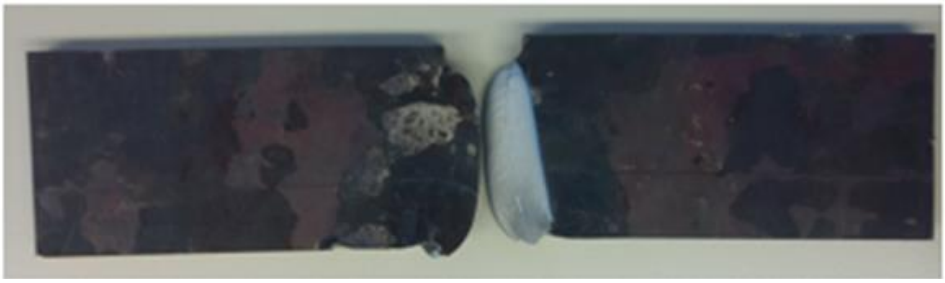

(a) Plane view

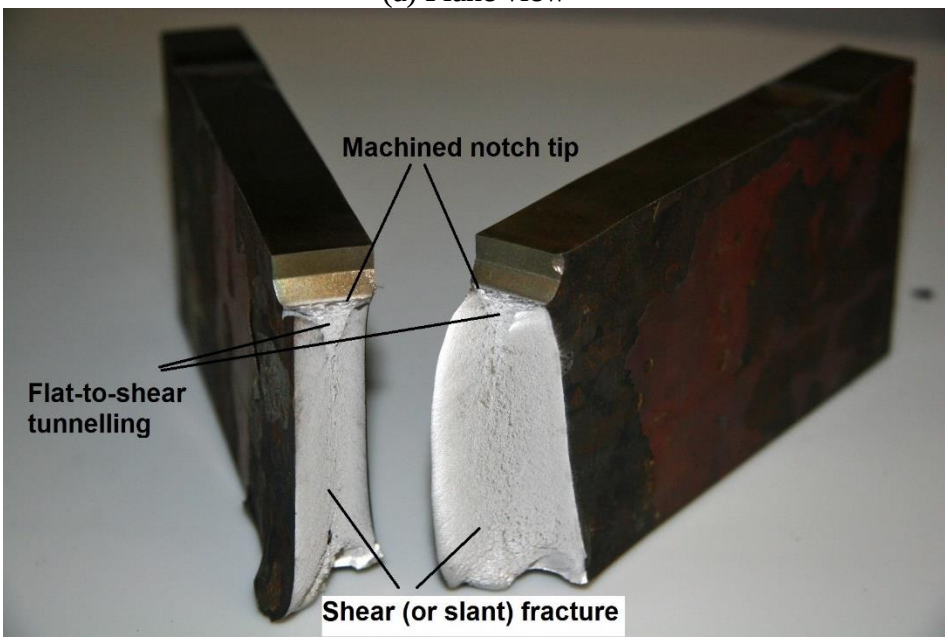

(b) Fracture Surface

Figure 36: A slant fractured A516-70 DWTT specimen (Specimen TD3)

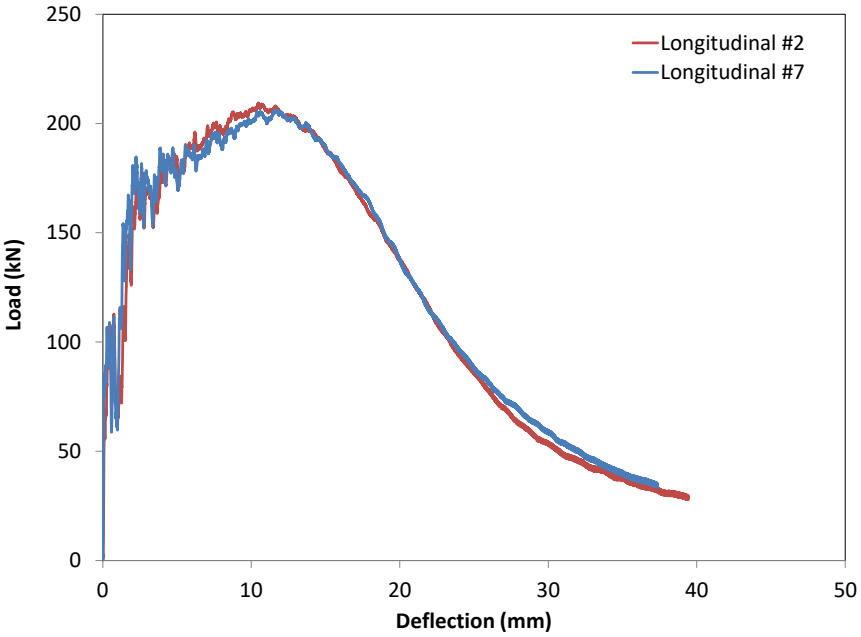

(a) Longitudinal sample

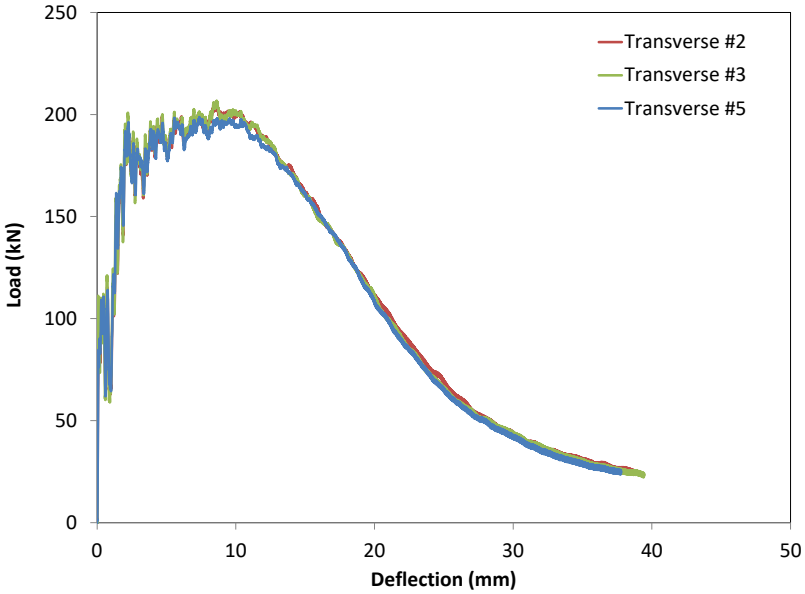

(b) Transverse sample

Figure 37: Load vs. deflection curves of drop-weight tear test (DWTT) samples of TC 128B recorded during impact testing.

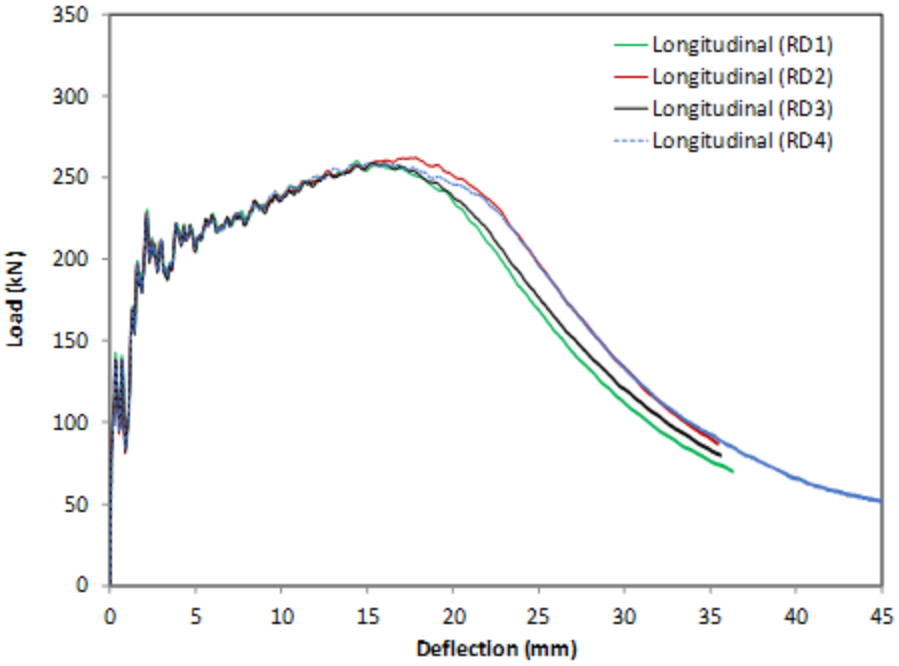

(a) Longitudinal specimen

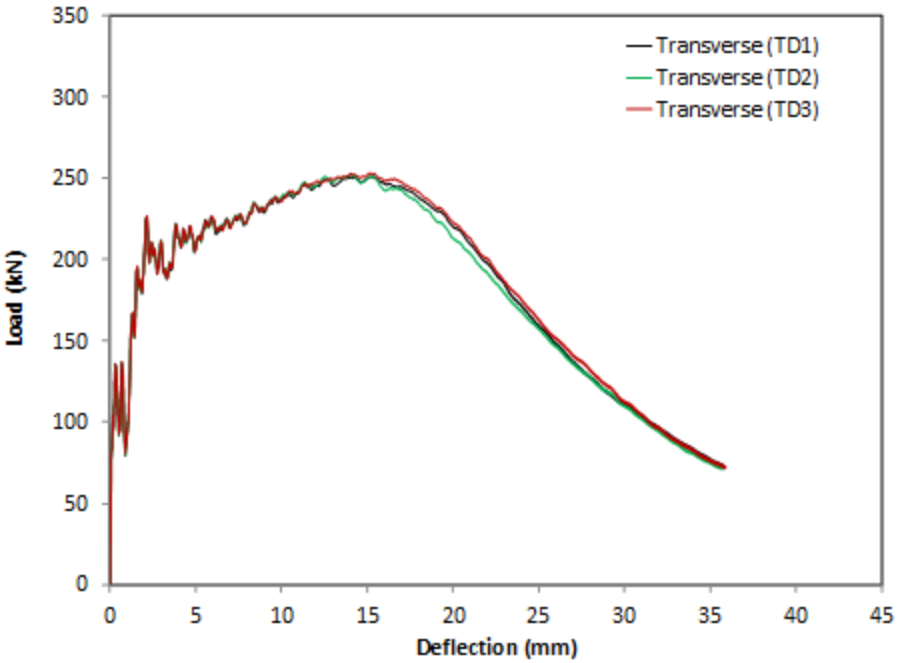

(b) Transverse specimen

Figure 38: Load vs. deflection curves of A516-70 DWTT specimens recorded during impact testing

According to ASTM E3039-16 [54], the procedure for calculating CTOA is:

- Find the maximum force value (P_m) and the corresponding load-line displacement value (Δ_m).
- Calculate and plot $\ln(P/P_m)$ versus $(\Delta-\Delta_m)/S$ for all data points beyond maximum force point (P_m, Δ_m) (i.e. the data corresponding to fracture propagation), where S is the loading span (S=254 mm).
- Find (ξ), the absolute value of the slope of the $\ln(P/P_m)$ versus $(\Delta-\Delta_m)/S$ curve, from all data corresponding to $\ln(P/P_m)$ values between -0.5 and -1.2 for the 10 mm deep notched specimen.

The critical CTOA values, $CTOA_{B/2}$, were calculated according to the following equation:

$$CTOA_{B/2} = \frac{8r_p}{\xi} \quad \frac{180}{\pi} \tag{4}$$

where r_p is the rotation factor, ξ is the absolute value of the slope and the CTOA is in units of degrees. The value of r_p for steels is

$$r_p = 0.58\frac{CVN}{\sigma_y \cdot B} + 0.55 \tag{5}$$

where CVN, σ_y and B are in units of J, MPa and mm, respectively. The calculated values of r_p, ξ and CTOA are summarized in Table 15 and Table 16. The mean averages of $CTOA_{B/2}$ are 11.3° and 10.2° for longitudinal and transverse samples of TC128B, respectively. The averages of $CTOA_{B/2}$ are 13.4° and 13.7° for longitudinal and transverse specimens of A516-70. The larger the CTOA, the higher the fracture propagation resistance. The CTOA values are in the low/middle range of $CTOA_{B/2}$ compared to pipe steels. The ASTM CTOA test standard E3039 provides the steel industry with a practical tool to optimize fracture propagation resistance as a function of composition and processing.

Table 15: Rotation factor, ξ and CTOA for TC128B

Specimen	**CVN (J)**	**B (mm)**	**YS (MPa)**	**r_p**	**Slope ξ**	**$CTOA_{B/2}$ (°)**	**Mean average $CTOA_{B/2}$ (°)**
RD2	269	15.2	390	0.58	25.22	10.5	11.3
RD3				0.58	21.62	12.2	
TD2	205	15.2	389	0.57	24.70	10.6	10.2
TD3				0.57	26.00	10.1	
TD5				0.57	25.96	10.1	

Table 16: Rotation factor, ξ and CTOA for A516-70

Specimen	CVN (J)	B (mm)	YS (MPa)	r_p	Slope	CTOA (°)	Mean average CTOA (°)
RD1	221	19.1	351	0.57	20.2	12.9	13.4
RD2	221	19.1	351	0.57	20.2	12.9	
RD3	221	19.1	351	0.57	19.1	13.7	
RD4	221	19.1	351	0.57	18.5	14.1	
TD1	203	19.1	343	0.57	18.3	14.2	13.7
TD2	203	19.1	343	0.57	19.1	13.6	
TD3	203	19.1	343	0.57	19.8	13.1	

The fourth A516-70 DWTT specimen in TD orientation showed a sharp load drop after the maximum load (Figure 74) that was found to correspond to a cleavage (brittle) fracture region in the specimen as shown in Figure 40. Since E3039 requires at least 85% shear area of a DWTT specimen for ductile fracture propagation toughness, this specimen (approximately 60% shear) was not included in the calculation of the mean average CTOA. The cleavage fracture region is believed to be related to the mixture of bainite and marternsite observed close to mid-thickness. This was not observed in the TC128B steel [3].

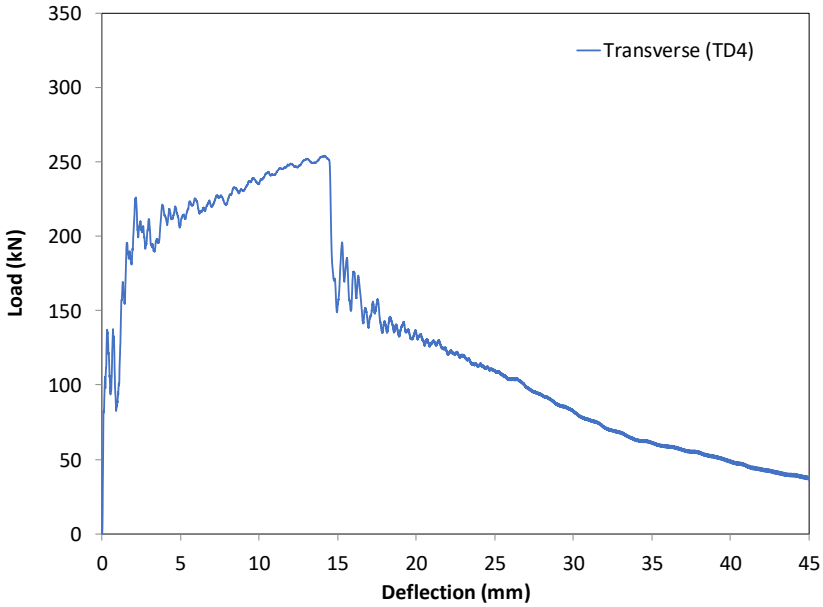

Figure 39: Load vs. deflection curve of a DWTT specimen in TD orientation showing a load drop during the test

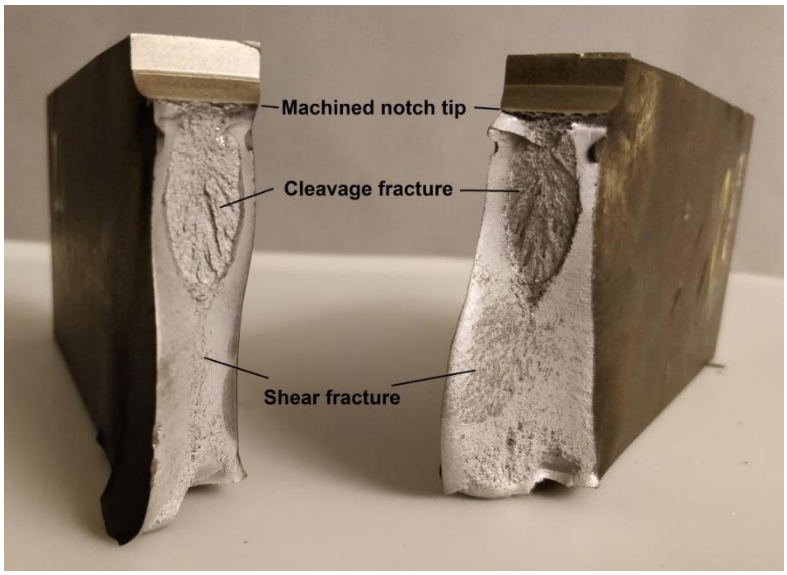

Figure 40: A DWTT specimen (TD4) showing a large cleavage region close to the notch tip

A single A516-70 DWTT RD specimen was tested at an intermediate loading rate of 0.1 m/s. The tested specimen displayed slant fracture as shown in Figure 41 and Figure 42. Unintentionally, during initial loading, the press stopped at about 4 mm deflection before reaching maximum load. The specimen was subsequently re-loaded to fracture. This would not affect CTOA according to ASTM E3039 because this property represents fracture propagation toughness and is derived using data obtained well after the maximum load (between the load range of 0.6-0.3 of maximum load). Figure 43 compares load vs. deflection curves of tests at the intermediate and impact rates. There is a modest increase in flow strength (consistent with the effect of strain rate on strength) and a slight increase in maximum-load deflection with increasing hammer velocity. The $CTOA_{B/2}$ of the specimen tested at the intermediate rate is 13.1° indicating negligible effect of loading rate on CTOA within the test rate range (see Table 16). This loading rate effect is consistent with observations on pipe steels [68]. The velocity of the crack as it propagated between crack lengths of 27 mm and 39 mm (the steady-state range where CTOA remains essentially constant) was estimated to be 0.19 m/s.

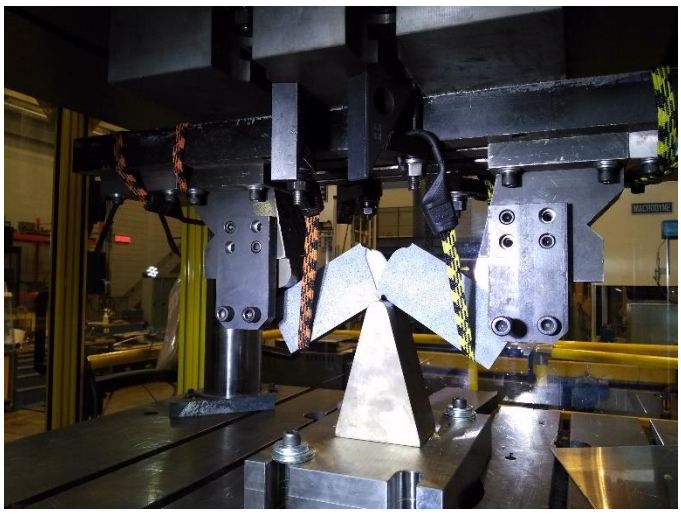

Figure 41: Loading fixture in a 110-ton press for intermediate-rate testing and the tested specimen fractured in slant mode

Figure 42: Fracture surface of DWTT specimen tested at intermediate rate

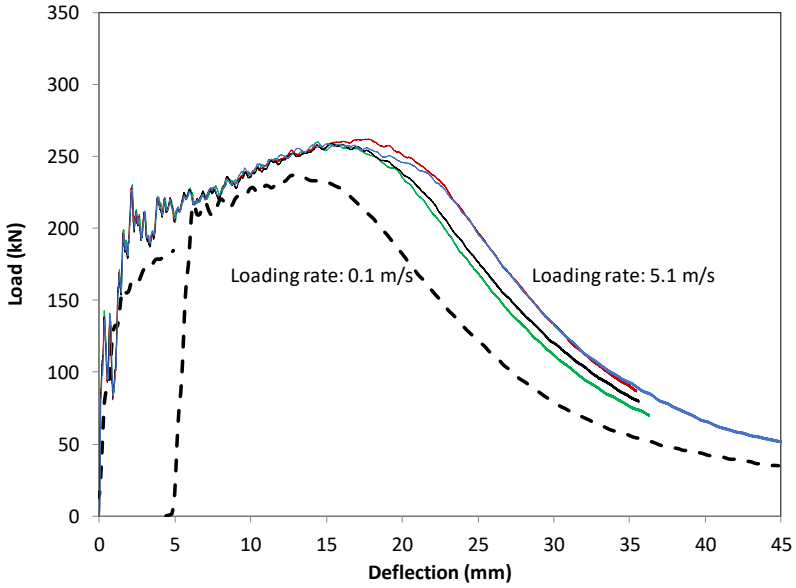

Figure 43: Load vs. deflection curves of A516-70 DWTT specimens in longitudinal orientation at different loading rates

Surface strain distribution was obtained from the digital image correlation (DIC) technique. The major strain (in the DWTT specimen length direction) and map, minor strain (in the DWTT specimen width direction) and map, and strain in the thickness direction ahead of the crack tip at a surface crack length of 35 mm (in the steady-state region) is shown in Figure 44. The major strain was approximately 33% close to the crack tip and decreased with distance away from the crack tip. Consistent with the rotation of the DWTT specimen and the requirement for force balance, the major strain decreased and changed to compressive strain near the neutral axis; the maximum compressive strain was approximately -9.5% at 31 mm ahead of the crack tip. The minor strain was approximately -3% close to the crack tip and increased and remained to be close to 0, and increased toward to the loading point. The presence of both major and minor strains indicates a bi-axial stress state ahead of the crack tip, although the major strain dominates as expected. Strains in the thickness direction were calculated from conservation of volume, and reflect thinning at the crack tip and thickening at the impact point. The strain distributions were in general agreement with previous simulation work on pipe steel [69].

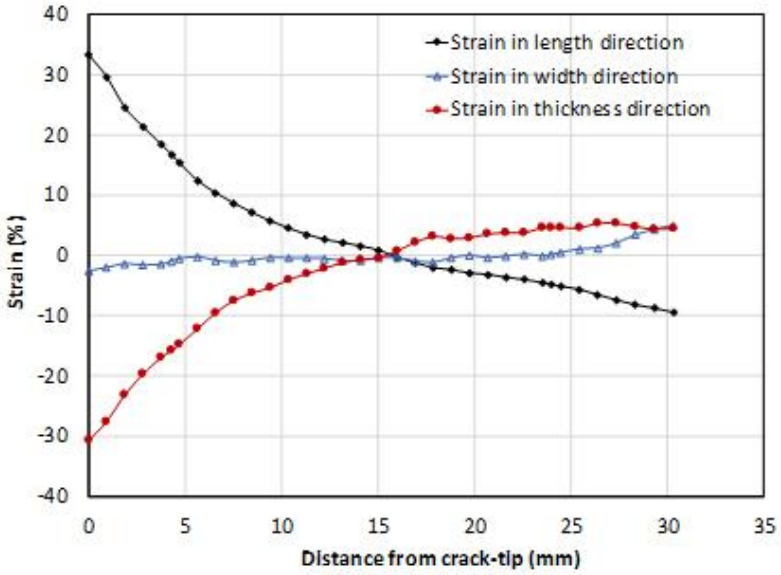

(a) Strain distributions

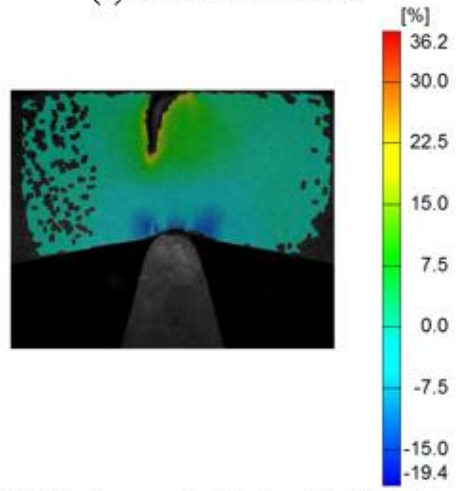

(b) Strain map in the length direction

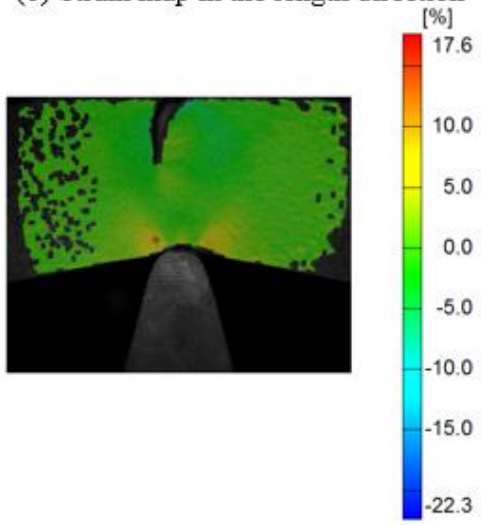

(c) Strain map in the width direction

Figure 44: Strain distribution ahead of crack tip at crack length of 35 mm (steady-state region)

6.3.3 Fracture Toughness

Typical P (load) vs. CMOD and P vs. LLD of the SE(B) specimens including partial unloadings are illustrated in Figure 45 through Figure 48 for deep-cracked and shallow-cracked samples of TC128B and A516-70.

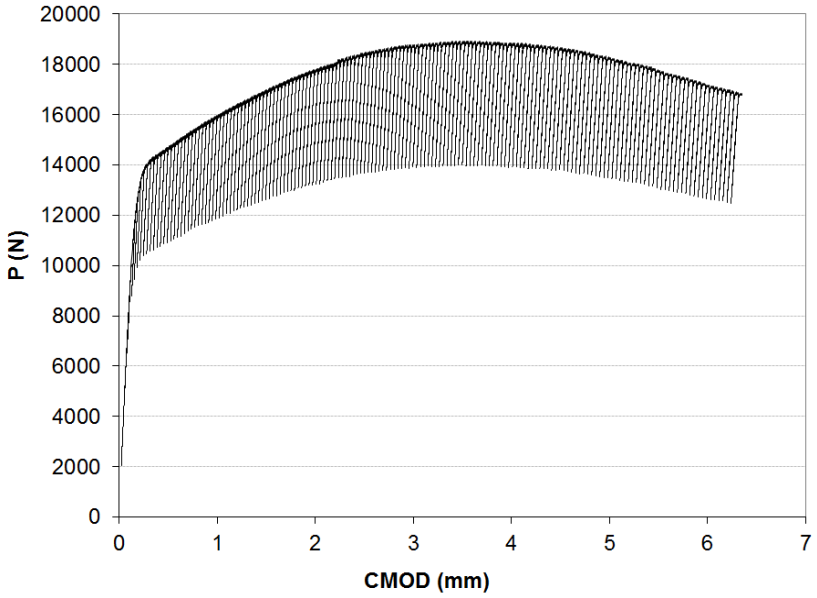

(a) Deep-cracked SE(B) spec. #2

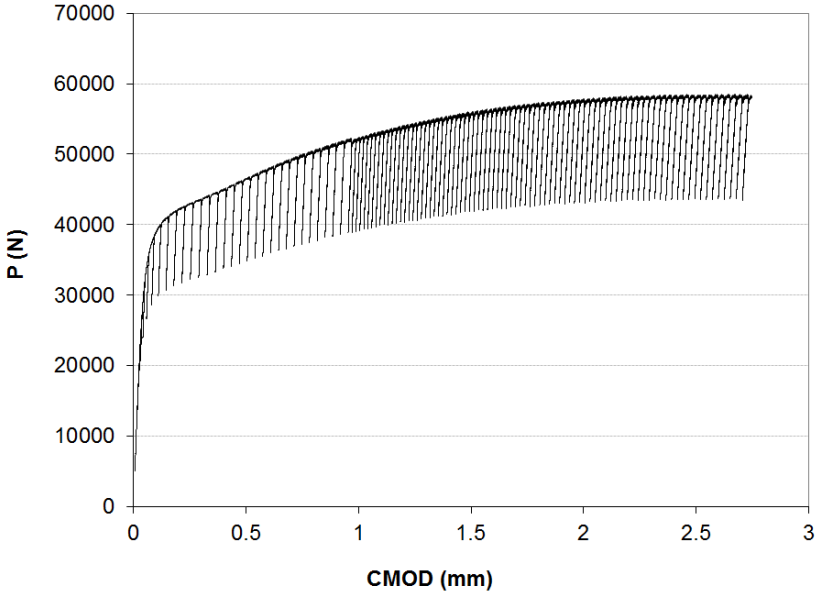

(b) Shallow-cracked SE(B) spec. #5

Figure 45: Load vs. CMOD of SE(B) TC128B specimens.

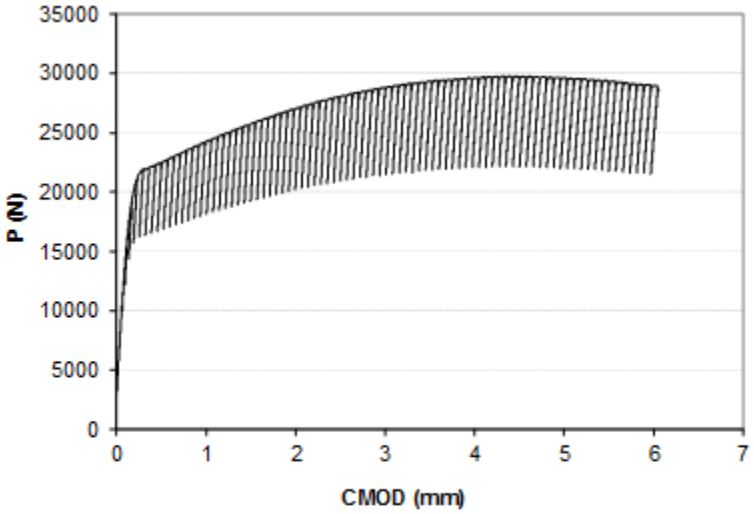

(a) Deep-cracked SE(B) spec. #1D

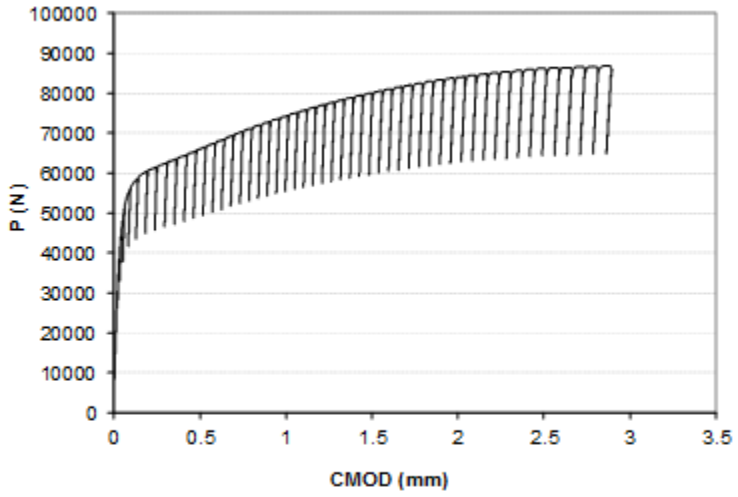

(b) Shallow-cracked SE(B) spec. #1S

Figure 46: Load vs. CMOD of SE(B) A516-70 specimens

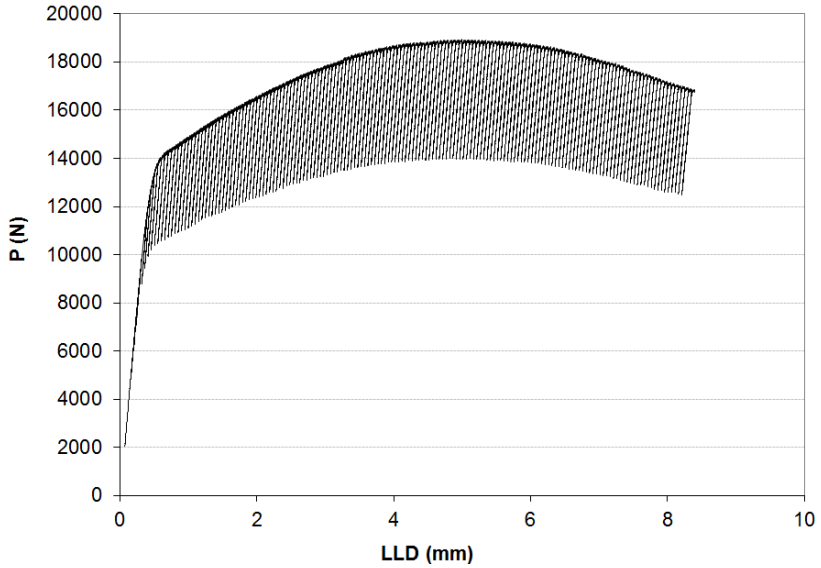

(a) Deep-cracked SE(B) spec. #2

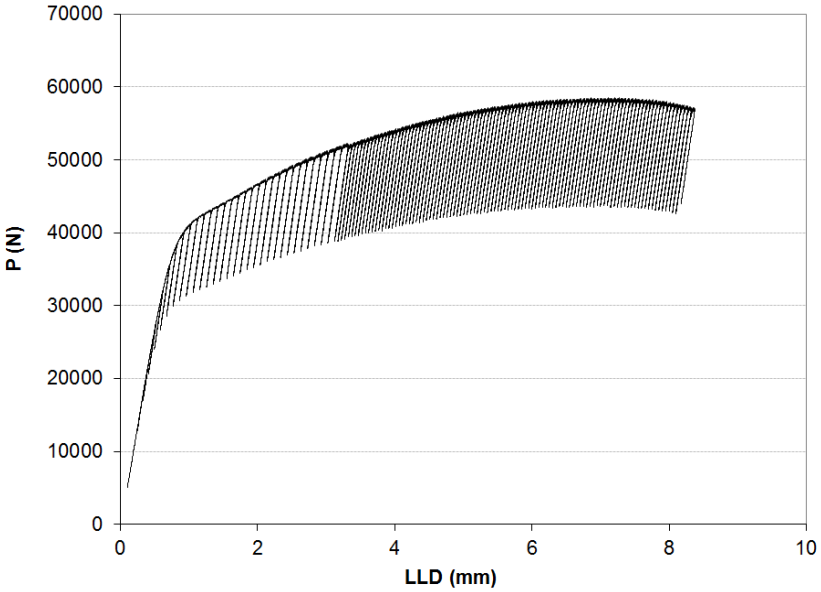

(b) Shallow-cracked SE(B) #5

Figure 47: Load vs. LLD of SE(B) TC128B specimens.

Typical P vs. CMOD and P vs. LLD curves of the SE(T) specimens including partial unloadings are illustrated in Figure 48 through Figure 51 for both deep-cracked and shallow-cracked samples of TC128B and A516-70. For deep-cracked SE(T) samples, P vs. CMOD and P vs. LLD curves look similar to those observed in pipe steels. For shallow-cracked SE(T) samples, there were small load drops and/or flat regions before the attainment of maximum load during the

displacement controlled loading. This feature is believed to be related to the long discontinuous yielding observed in tensile tests (see Figure 18, Figure 19) and is different from pipe steels.

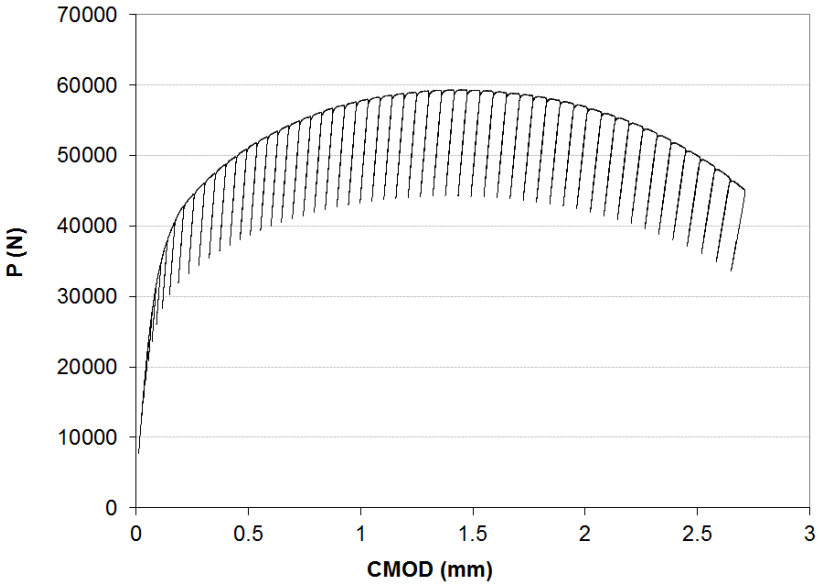

(a) Deep-cracked SE(T) spec. #2

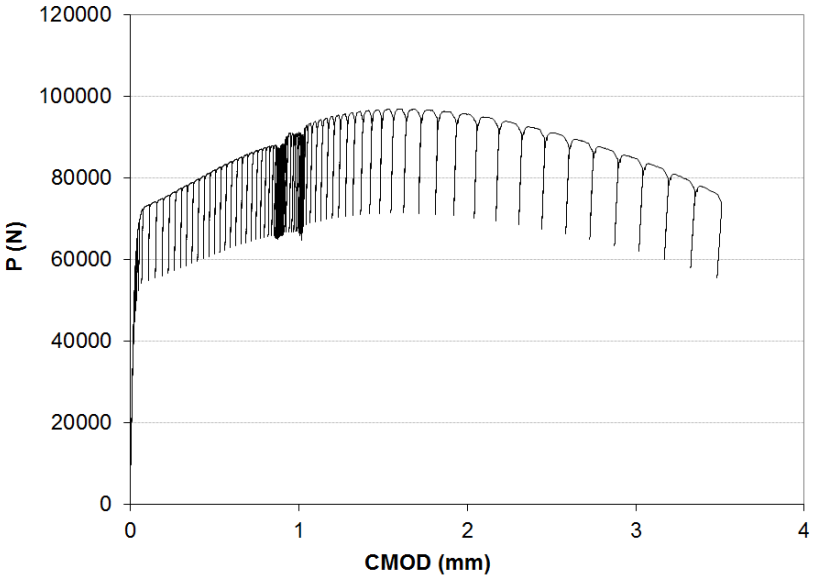

(b) Shallow-cracked SE(T) spec. #1

Figure 48: Load vs. CMOD of SE(T) TC 128 B specimens.

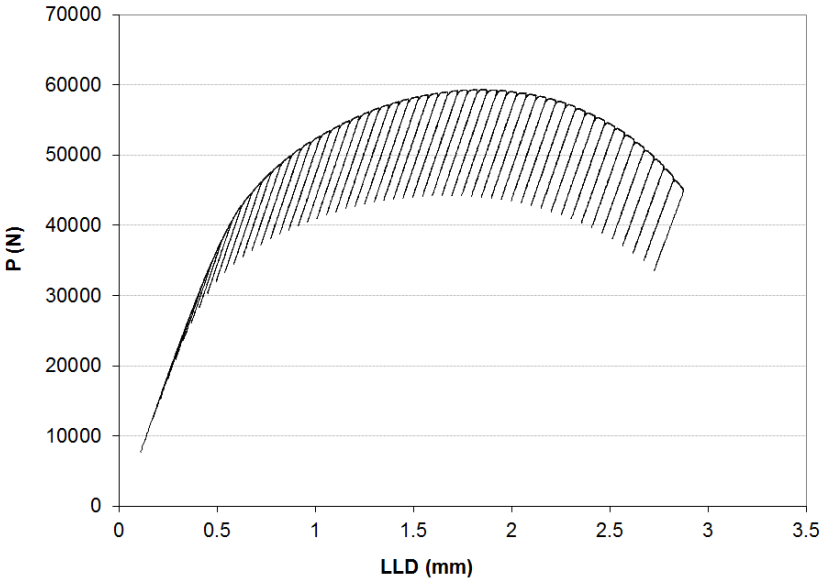

(a) Deep-cracked SE(T) spec. #2

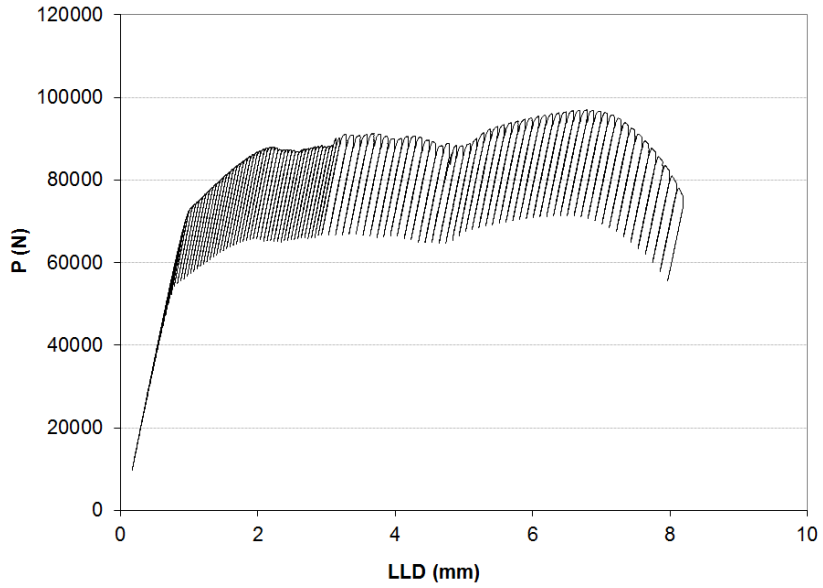

(b) Shallow-cracked SE(T) spec. #1

Figure 49: Load vs. LLD of SE(T) TC128 B specimens.

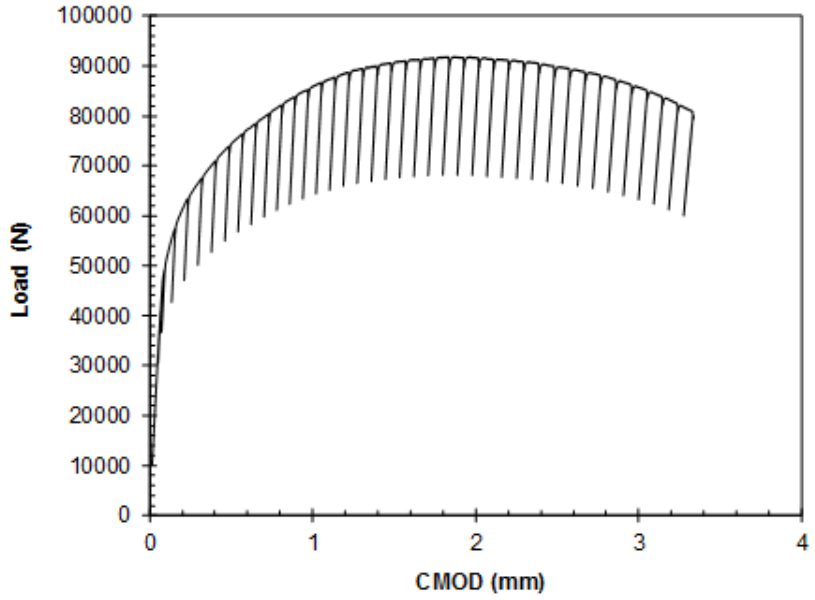

(a) Deep-cracked SE(T) spec. #6D

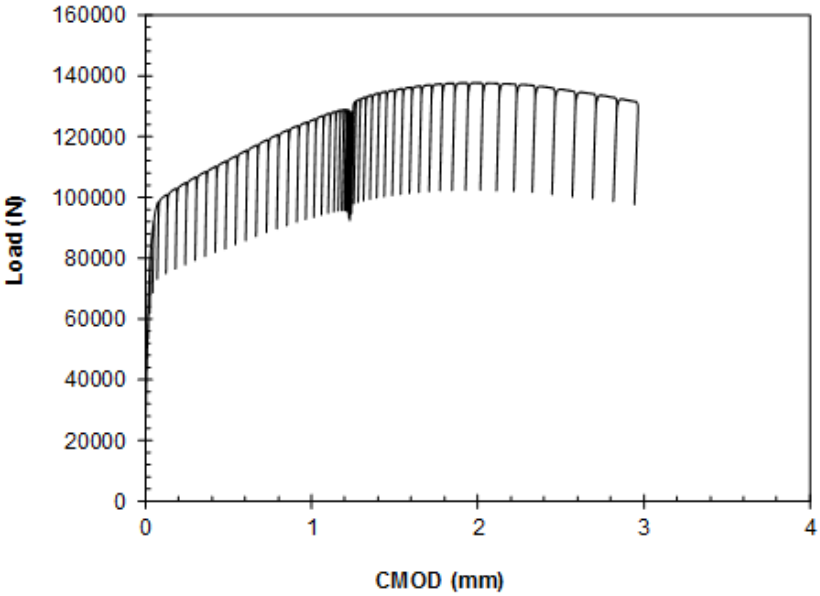

(b) Shallow-cracked SE(T) spec. #4S

Figure 50: Load vs. CMOD of SE(T) A516-70 specimens

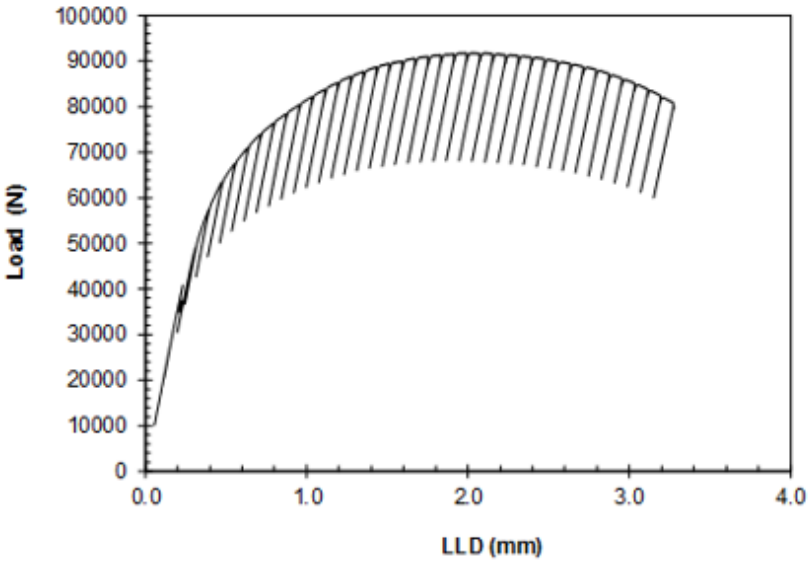

(a) Deep-cracked SE(T) spec. #6D

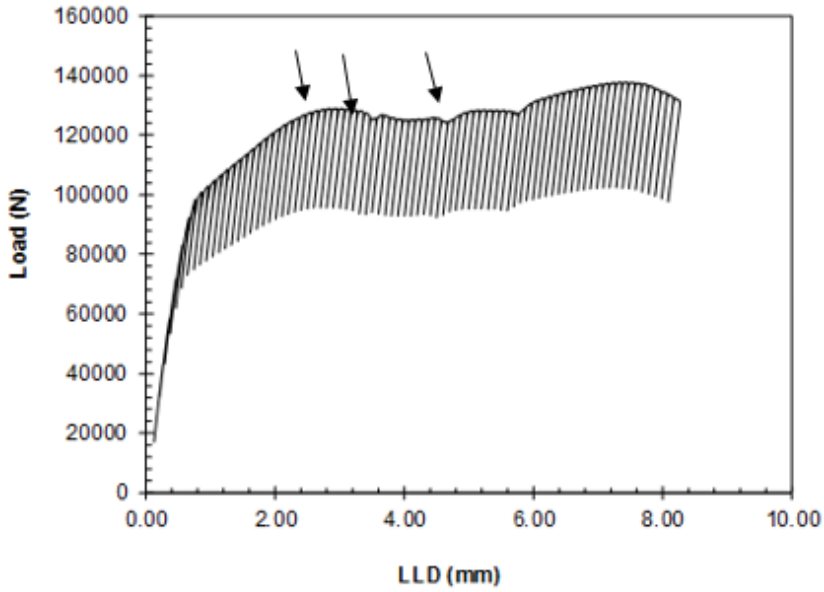

(b) Shallow-cracked SE(T) spec. #4S

Figure 51: Load vs. LLD of SE(T) A516 specimens

All tested samples were heat tinted at 350°C in air for 30 minutes to mark the crack extension and were fractured by impact after immerging in liquid nitrogen. Typical fracture surfaces are displayed in Figure 52; crack extensions were relatively uniform. Initial and final crack lengths were measured on fracture surfaces. Most samples met the ASTM E1820 crack size validity requirements except for some deep-cracked SE(B) samples. The crack size requirements indicate the crack size estimation accuracy from the compliance method and the accuracy is usually related to testing conditions (e.g., alignment or specimen size). The SE(T) samples also met the draft crack size validity requirements in [56].

Deep-cracked SE(B) spec. #2	Shallow-cracked SE(B) spec. #5	Deep-notched SE(T) spec. #2	Shallow-cracked SE(T) spec. #1

Figure 52: Typical fracture surfaces of tested fracture toughness samples.

Fracture toughness results are presented below. Deep-cracked B×2B SE(B) specimens (fatigue pre-cracked to a_0/W~0.5) are standard fracture toughness specimens (ASTM E1820 [55]), designed to give high-constraint lower-bound fracture toughness values. J-resistance (J-R) curves are shown in Figure 53 and Figure 54 according to ASTM E1820 [55]. The J-R results were consistent and all data were fitted to a standard power-law equation:

$$J = C_1(\Delta a)^{C_2} \quad \sigma_y(T) = \sigma_{y0}\exp\left(-\frac{1}{2}\left[\frac{T\text{-}RT}{r_3}\right]^{r_1} - \frac{1}{2}\left[\frac{T\text{-}RT}{r_4}\right]^{r_2}\right) \tag{6}$$

where J is in kJ/m^2, C_1 and C_2 are fitting constants, and Δa is the crack extension in mm. The horizontal dashed line in Figure 53 (and similar figures in the report) gives the maximum specimen-size-independent J value (i.e. the "capacity" of a specimen) and the vertical dashed line is the maximum crack extension capacity according to ASTM E1820 [55]. The maximum specimen-size- independent J values were reached after approximately 0.76 mm crack extension although the J-R curves are relevant to larger extensions if the results are used for assessment of the same thickness components as the samples. Maximum loads (or peak loads) were achieved at 0.76 – 0.88 mm for deep-cracked SE(B) specimens at room temperature and 1.2-1.3 mm for A516-70 specimens; these crack extensions are much larger than typical values for pipe steels (e.g. 0.1-0.3 mm [70]). This phenomenon is believed to be related to the discontinuous yielding; the steel starts to work harden only after the significant flat stress-strain initial region (Lüders region) that extends up to ~2.9%. The values of C_1 and C_2 for each specimen were obtained by least-squares fitting of the experimental data of repeated tests and are reported in Table 17; also included in Table 17 are the values for each SE(B) and SE(T) test and the mean values. In Table 17, a_0 is the physical measurement (on the fracture surface) of crack length. The J values at 0.2 mm crack growth, $J_{0.2}$, evaluated using Eq. (6), are also listed in Table 17 as fracture toughness initiation values for engineering critical assessment (ECA) purposes. The J values of the steel are acceptable for structural applications, although in the relatively low range compared to modern pipe steels[61].

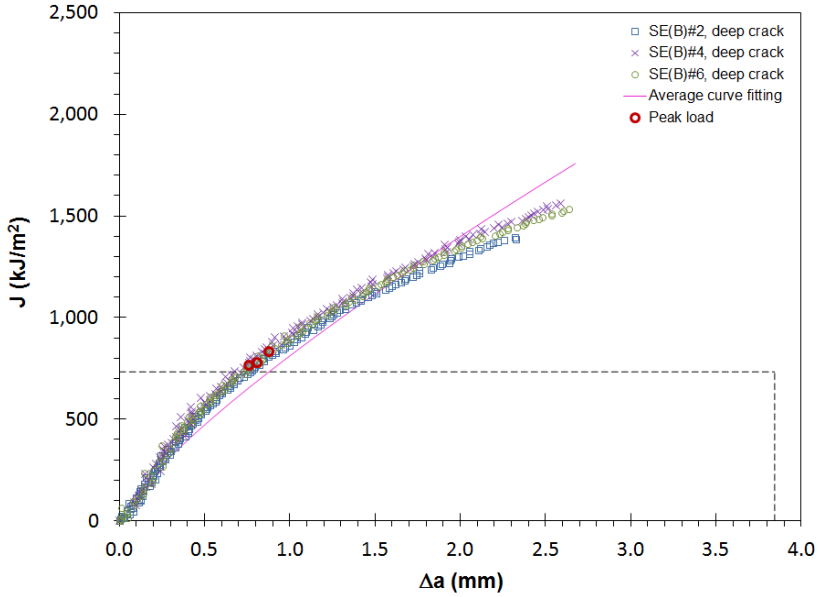

Figure 53: J-R curves of deep-cracked TC128B SE(B) specimens.

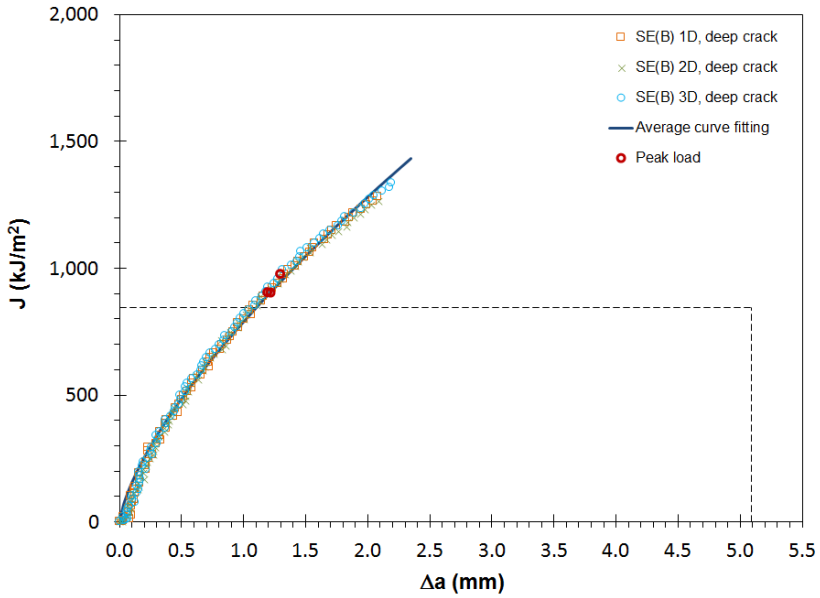

Figure 54: J-R curves of deep-cracked A516-70 SE(B) specimens

J-R curves of shallow-cracked SE(B) specimens are shown in Figure 55 and Figure 56. The fitting constants of C_1 and C_2, and $J_{0.2}$ for each specimen are listed in Table 17. Maximum loads of shallow-cracked samples were reached at 1.60-1.95 mm crack growth for TC128B and at 1.7-2.1 mm for A516-70. which were larger than those of the deep-cracked SE(B) specimens and of typical pipe steel (0.3-0.4 mm [70]). Shallow-cracked SE(B) specimens represent low-constraint conditions compared to those of deep-cracked SE(B) specimens and usually show higher J values (e.g., [70]for pipe steel). For the steels tested here at room temperature, J values were insensitive to the initial crack length and the mean average fitted $J_{0.2}$ values of shallow-cracked specimens were even slightly lower than those of deep-cracked SE(B) specimens. The results are in contrast to an X100 pipe steel [70] and may be related to the discontinuous yielding of

TC128B and A516-70 steels. It has been shown using cohesive zone modelling[1] that discontinuous yielding increases fracture toughness [59]. However, the interplay between discontinuous yielding and constraint on fracture toughness has yet to be investigated. This is of great interesting to structural performance of tank car steels and can be studied in the future using finite element modelling (FEM).

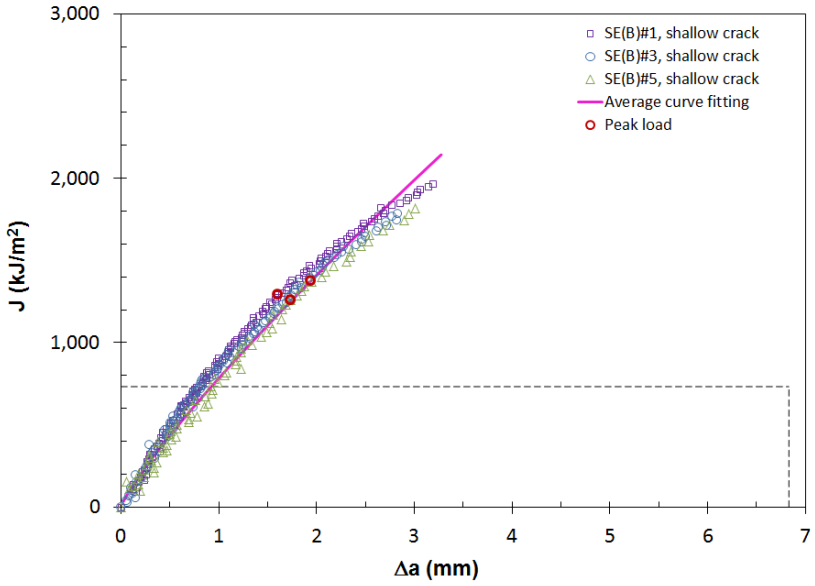

Figure 55: J-R curves of shallow-cracked TC128 B SE(B) specimens.

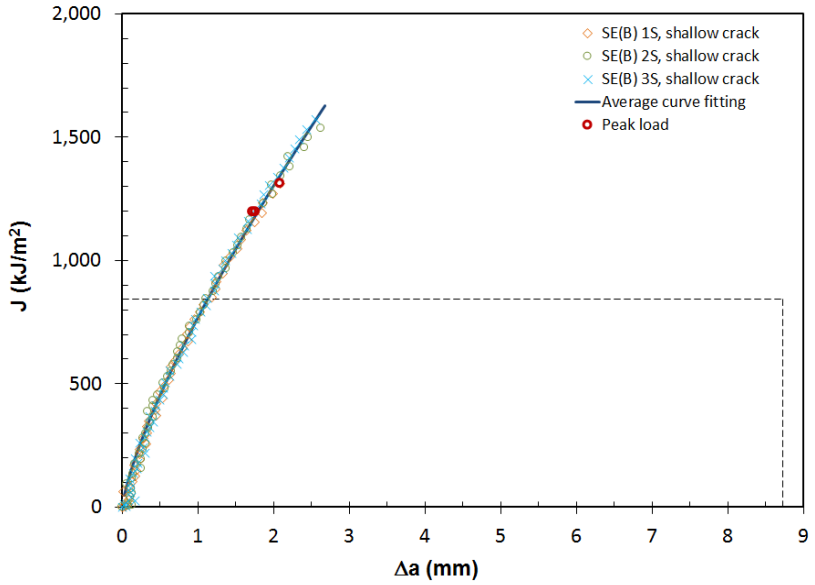

Figure 56: J-R curves of shallow-cracked A516-70 SE(B) specimens.

[1] The cohesive zone model (CZM) is a model in fracture mechanics in which fracture formation is regarded as a gradual phenomenon in which separation of the surfaces involved in the crack takes place across an extended crack tip, or cohesive zone, and is resisted by cohesive tractions.

Table 17: Parameters C_1 and C_2 fitted to J resistance curves, and initiation fracture toughness

Steel	Specimen Identification, B×W	a_0/W	C_1 (kJ/m2)	C_2	$J_{0.2}$ (kJ/m^2)
TC128B	SE(B) 2, B×2B	0.499	798	0.832	209
	SE(B) 4, B×2B	0.499	844	0.716	267
	SE(B) 6, B×2B	0.499	792	0.809	215
	Mean average	**0.499**	**813**	**0.783**	**230**
	SE(B) 1, B×2B	0.102	827	0.828	218
	SE(B) 3, B×2B	0.109	774	0.884	186
	SE(B) 5, B×2B	0.104	751	0.833	197
	Mean average	**0.105**	**784**	**0.848**	**200**
	SE(T) 2, B×B	0.487	723	0.648	255
	SE(T) #3 B×B	0.498	680	0.786	192
	SE(T) 5, B×B	0.505	605	0.769	175
	Mean average	**0.497**	**669**	**0.734**	**207**
	SE(T) 1, B×B	0.185	956	0.710	305
	SE(T) 4, B×B	0.187	956	0.750	286
	SE(T) 6, B×B	0.185	982	0.734	301
	Mean average	**0.186**	**965**	**0.732**	**297**
A517-70	SE(B) 1D, B×2B	0.49	785	0.707	206
	SE(B) 2D, B×2B	0.49	784	0.699	206
	SE(B) 3D, B×2B	0.49	800	0.686	207
	Mean average		**790**	**0.697**	**206**
	SE(B) 1S, B×2B	0.11	764	0.769	180
	SE(B) 2S, B×2B	0.11	775	0.733	184
	SE(B) 3S, B×2B	0.11	768	0.780	177
	Mean average		**769**	**0.761**	**180**
	SE(T) 5D, B×B	0.46	717	0.657	131
	SE(T) 6D, B×B	0.46	750	0.599	196
	SE(T) 8D, B×B	0.46	766	0.564	243
	Mean average		**744**	**0.607**	**190**
	SE(T) 1S, B×B	0.20	913	0.640	238
	SE(T) 3S, B×B	0.21	911	0.634	290
	SE(T) 4S, B×B	0.20	900	0.680	249
	Mean average		**908**	**0.651**	**259**

J-R curves of deep-notched SE(T) specimens are shown in Figure 57 and Figure 58. J-R curves of shallow-notched SE(T) specimens are shown in Figure 59 and Figure 60. Some J-R curves showed concave shape in early crack extensions, and some apparent negative crack growths

were found based on the compliance method reflecting a discontinuous decrease of unloading slopes with increasing load (see Figure 48b, Figure 49b, Figure 50 b, and Figure 51 b), especially in shallow-cracked SE(T) samples. These could be related to discontinuous yielding; further investigation of the effects of discontinuous yielding on deformation and fracture could be done using FEM. Clamped SE(T) tests impose low constraint and have similar constraint conditions to surface flaws under tension. Compared to the B×2B SE(B) specimens, the B×B SE(T) specimens have lower constraint due to both tension loading and specimen width. The effect of crack size on SE(T) toughness at room temperature is as expected, in that deep-cracked SE(T) specimens have lower J values than those of shallow-cracked SE(T) specimens. Shallow-cracked SE(T) specimens had the highest J values of all four types of samples. However, comparison of SE(T) and SE(B) data does not show the trends expected as measured with pipe steels. For example, shallow-cracked SE(B) samples are not tougher than deep-cracked SE(B) specimens, contrary to expectation. This may be connected to the observed discontinuous yielding, but further analysis is required and it is suggested to use FEM.

J-R curves for the four sample types are compared in Figure 61 and Figure 62.

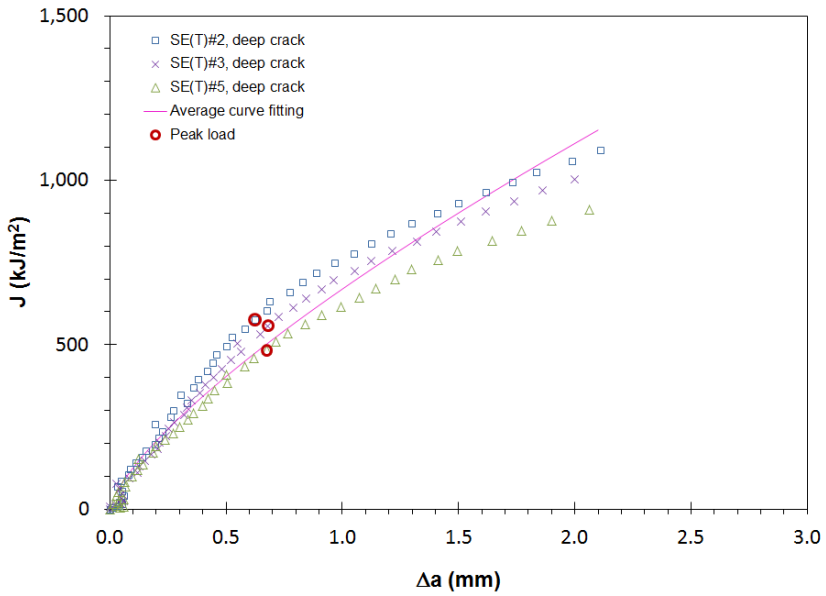

Figure 57: J-R curves of deep-cracked TC128B SE(T) specimens.

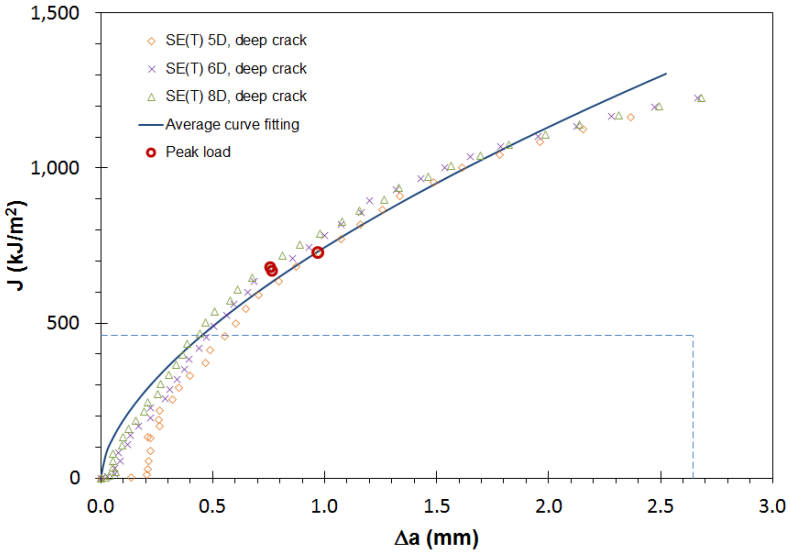

Figure 58: J-R curves of deep-cracked A516-70 SE(T) specimens

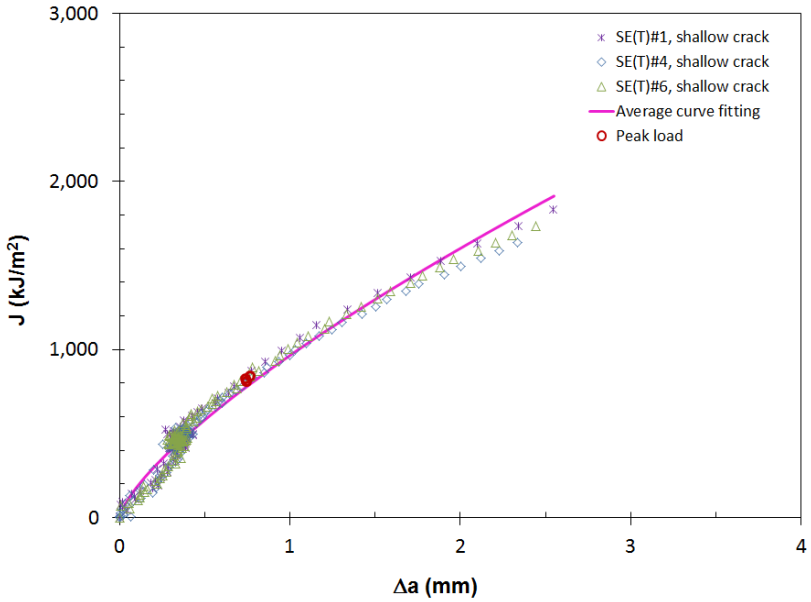

Figure 59: J-R curves of shallow-cracked TC128B SE(T) specimens.

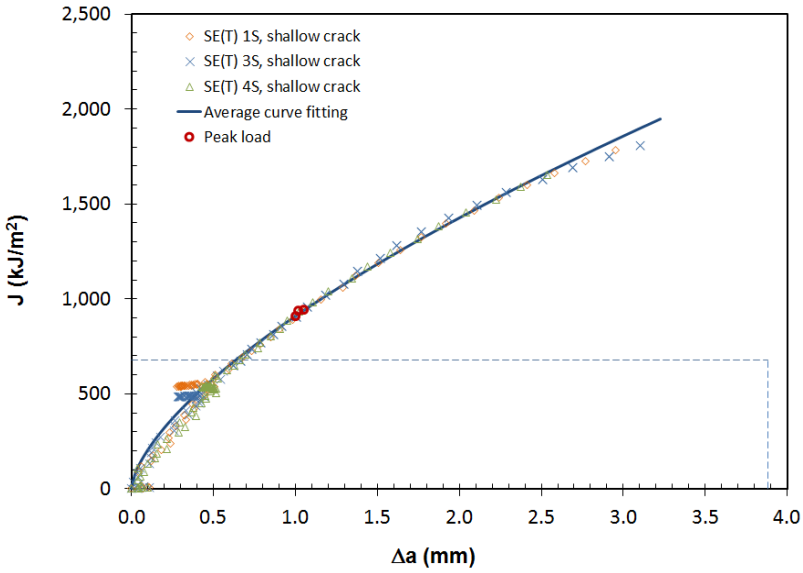

Figure 60: J-R curves of shallow-cracked A516-70 SE(T) specimens

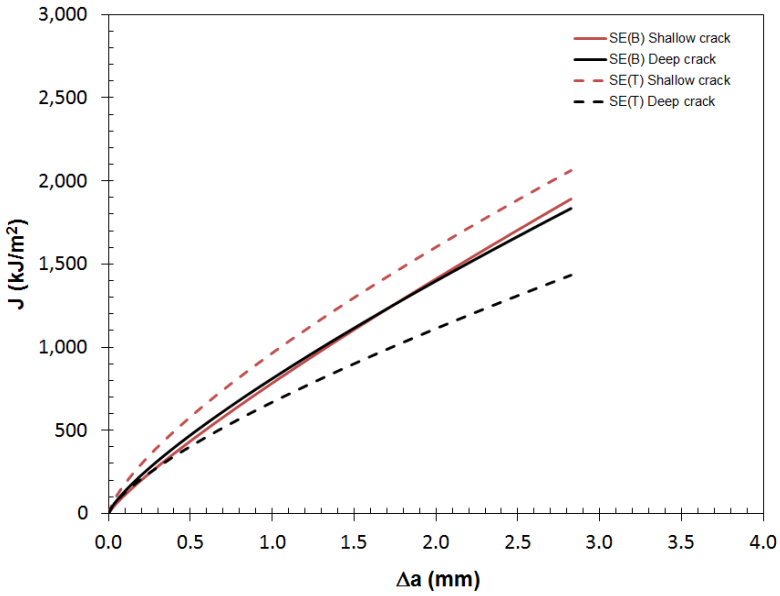

Figure 61: Comparison of J-R fitted curves of SE(B) and SE(T) specimens for TC128B.

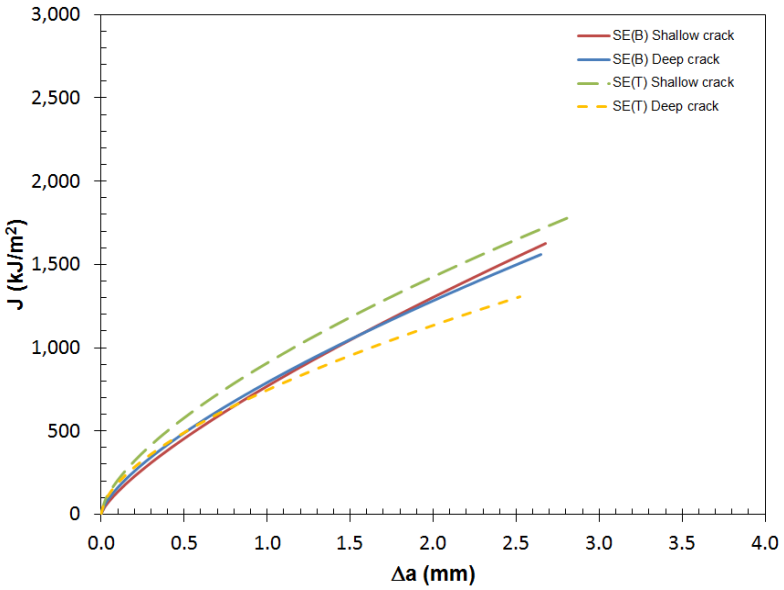

Figure 62: Comparison of J-R fitted curves of SE(B) and SE(T) specimens for A516-70

Crack-tip opening displacement (CTOD, or δ) is another elastic-plastic fracture mechanics parameter along with the J-integral and has been extensively used in pipeline applications. However, CTOD data for current tank car steels are very limited in open literature. CTOD can be correlated with J in a unique relation dependent primarily on work-hardening exponent and mode of loading, and values were converted from J-integrals for SE(B) specimens according to ASTM E 1820 [7] and for SE(T) specimens according to [56]. CTOD (δ) resistance curves are shown in Figure 63 - Figure 70. The trends of CTOD and CTOD-R curves are similar to J-R curves, because of the proportionality between CTOD and J. The solid line represents the standard fitting equation given by

$$\delta = D_1(\Delta a)^{D_2} \tag{7}$$

where δ and Δa are in mm, and D_1 and D_2 are fitting constants. The values of D_1 and D_2 for each specimen type were obtained by best-fitting the experimental data and are reported in Table 18. The CTOD values at 0.2 mm crack growth, $\delta_{0.2}$, evaluated using Eq. (7), are also listed in Table 18 CTOD-R fitted curves for the four sample types are compared in Figure 71 and Figure 72 for TC128 and A516-70 respectively.

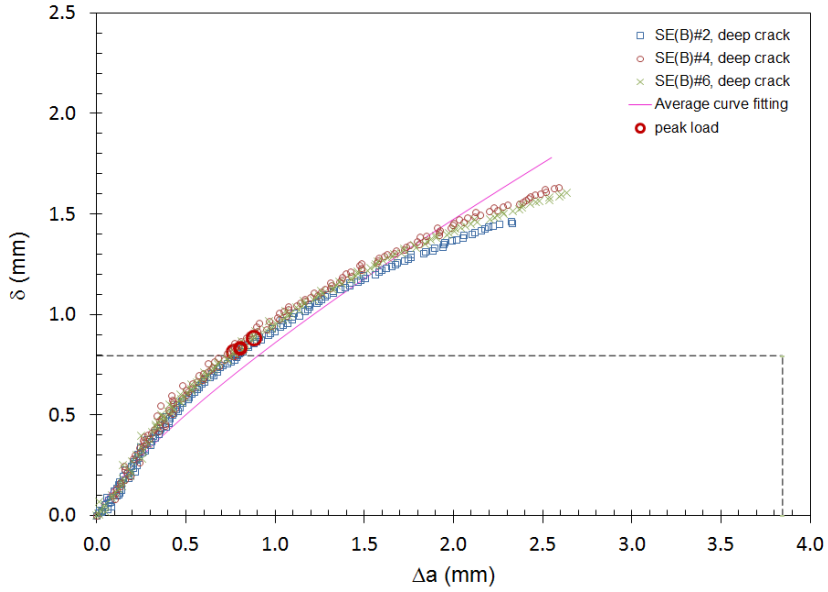

Figure 63: CTOD-R curves of deep-cracked TC128B SE(B) specimens.

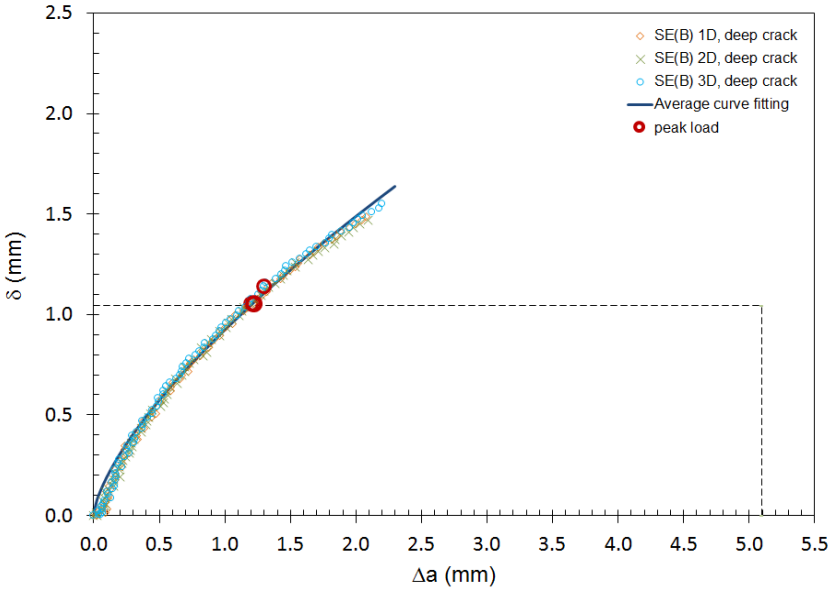

Figure 64: CTOD-R curves of deep-cracked A516-70 SE(B) specimens.

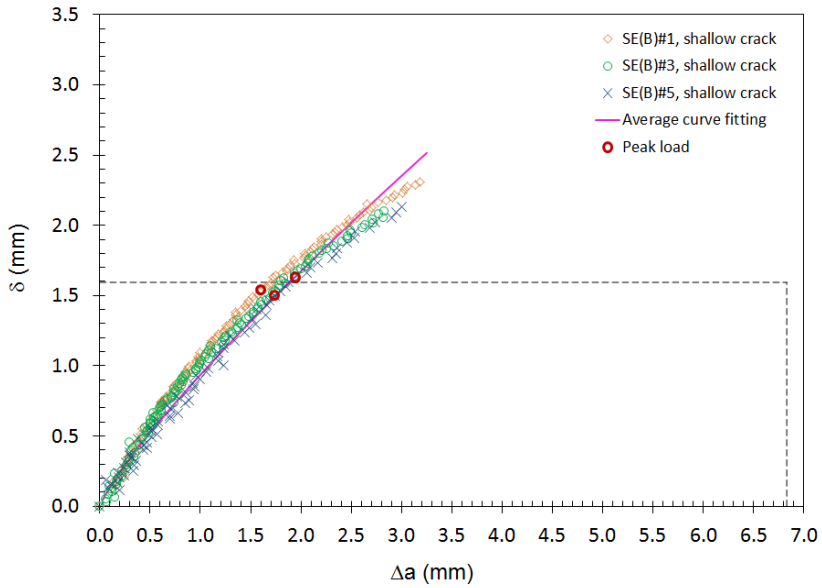

Figure 65: CTOD-R curves of shallow-cracked TC128B SE(B) specimens.

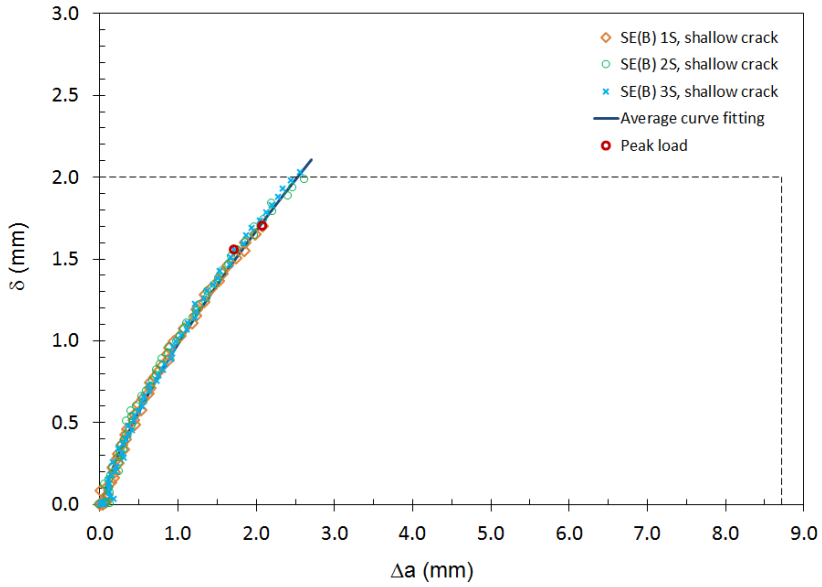

Figure 66: CTOD-R curves of shallow-cracked A516-70 SE(B) specimens.

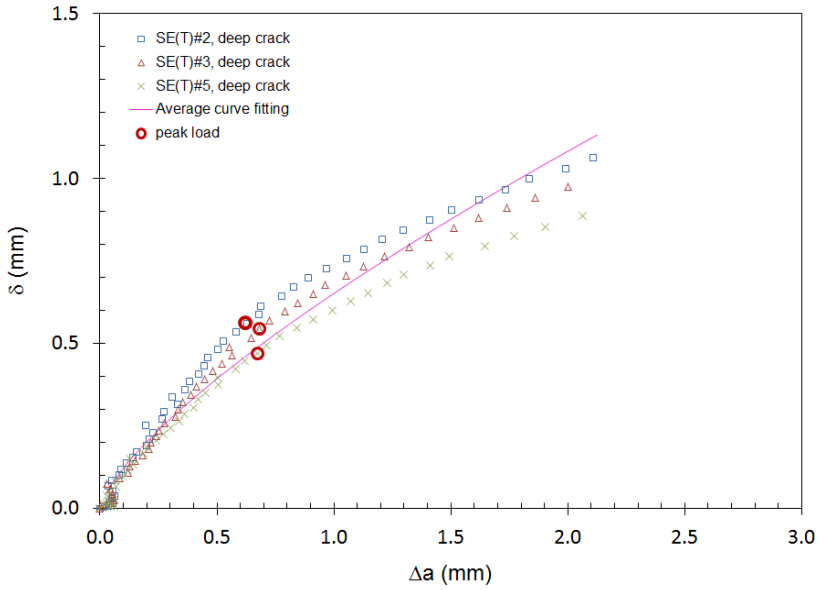

Figure 67: CTOD-R curves of deep-cracked TC128B SE(T) specimens.

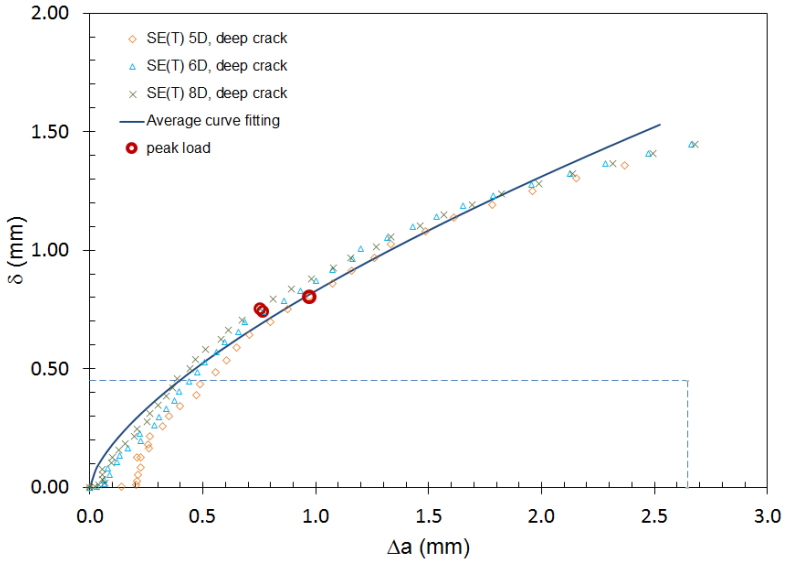

Figure 68: CTOD-R curves of deep-cracked A516-70 SE(T) specimens.

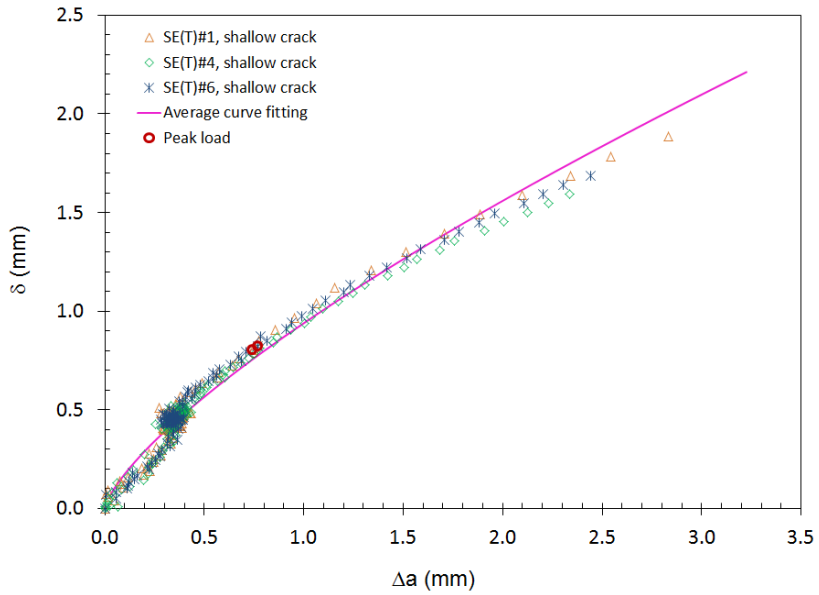

Figure 69: CTOD-R curves of shallow-cracked TC128B SE(T) specimens.

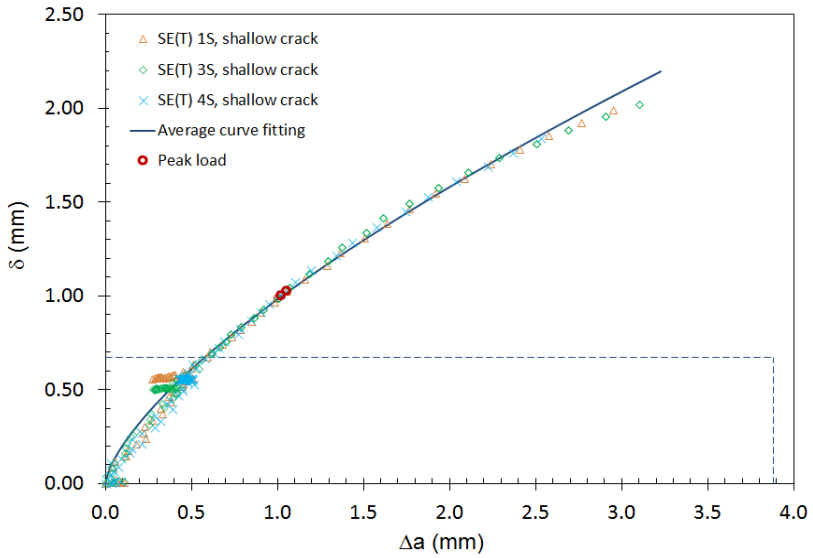

Figure 70: CTOD-R curves of shallow-cracked A516-70 SE(T) specimens.

Table 18: Parameters D_1 and D_2 fitted to CTOD resistance curves and initiation fracture toughness.

Steel	Specimen Identification, B×W	a_0/W	D_1 (mm)	D_2 (unit-less)	$\delta_{0.2}$ (mm)
TC128B	SE(B) 2, B×2B	0.499	0.846	0.826	0.224
	SE(B) 4, B×2B	0.499	0.895	0.707	0.287
	SE(B) 6, B×2B	0.499	0.838	0.802	0.230
	Mean average	**0.499**	**0.861**	**0.776**	**0.247**
	SE(B) 1, B×2B	0.102	0.989	0.815	0.266
	SE(B) 3, B×2B	0.109	0.924	0.874	0.226
	SE(B) 5, B×2B	0.104	0.899	0.824	0.239
	Mean average	**0.105**	**0.937**	**0.837**	**0.244**
	SE(T) 2, B×B	0.487	0.704	0.648	0.248
	SE(T) #3 B×B	0.498	0.662	0.785	0.187
	SE(T) 5, B×B	0.505	0.589	0.771	0.170
	Mean average	**0.497**	**0.652**	**0.735**	**0.202**
	SE(T) 1, B×B	0.185	0.931	0.710	0.297
	SE(T) 4, B×B	0.187	0.931	0.750	0.278
	SE(T) 6, B×B	0.185	0.956	0.734	0.293
	Mean average	**0.186**	**0.939**	**0.731**	**0.289**
A516-70	SE(B) 1D, B×2B	0.49	0.918	0.699	0.243
	SE(B) 2D, B×2B	0.49	0.917	0.692	0.243
	SE(B) 3D, B×2B	0.49	0.935	0.679	0.243
	Mean average		**0.923**	**0.690**	**0.243**
	SE(B) 1S, B×2B	0.11	0.999	0.761	0.237
	SE(B) 2S, B×2B	0.11	1.013	0.724	0.242
	SE(B) 3S, B×2B	0.11	1.003	0.770	0.233
	Mean average		**1.005**	**0.752**	**0.237**
	SE(T) 5D, B×B	0.46	0.793	0.716	0.127
	SE(T) 6D, B×B	0.46	0.838	0.654	0.195
	SE(T) 8D, B×B	0.46	0.854	0.617	0.246
	Mean average		**0.829**	**0.662**	**0.189**
	SE(T) 1S, B×B	0.20	0.986	0.677	0.239
	SE(T) 3S, B×B	0.21	0.985	0.669	0.295
	SE(T) 4S, B×B	0.20	0.970	0.719	0.250
	Mean average		**0.980**	**0.688**	**0.261**

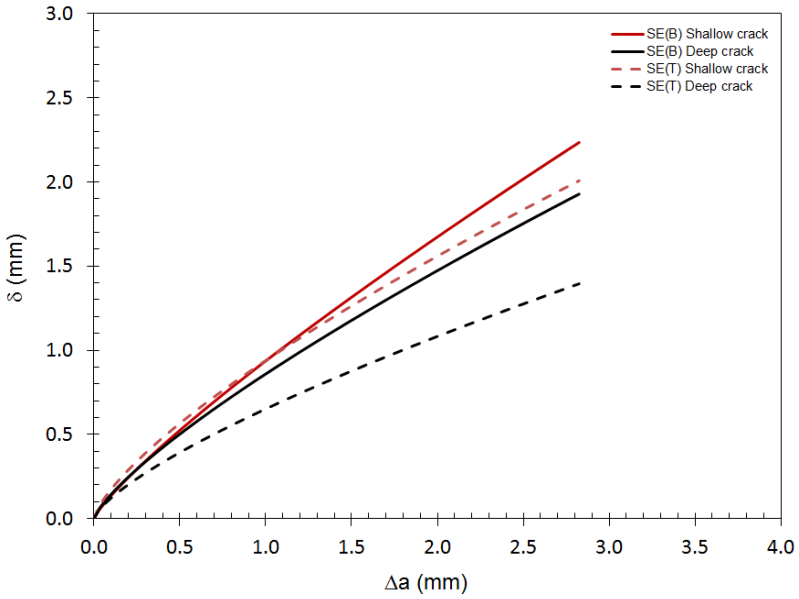

Figure 71: Comparison of CTOD-R fitted curves of SE(B) and SE(T) specimens for TC128B.

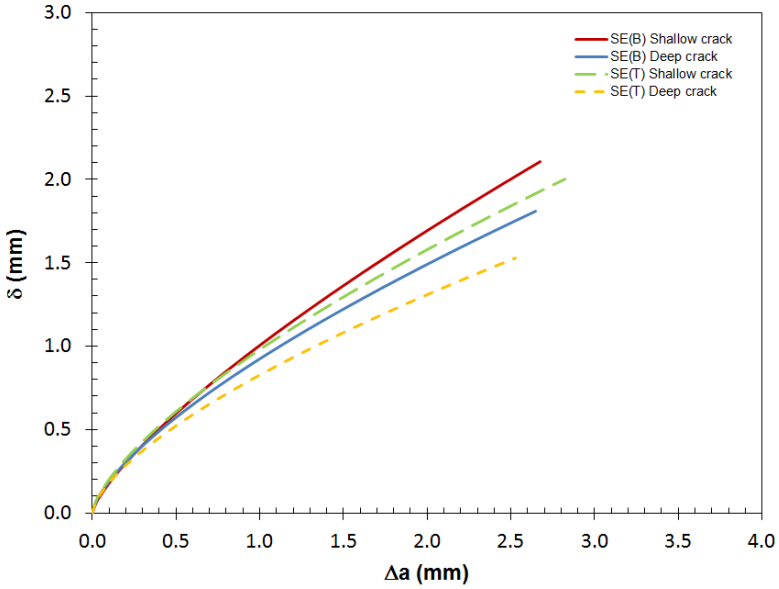

Figure 72: Comparison of CTOD-R fitted curves of SE(B) and SE(T) specimens for A516-70.

7 ANALYSIS OF THE TENSILE TEST RESULTS FOR CONSTITUTIVE MODELLING

There are a variety of models that may be used to describe the high-temperature behaviour of medium- and low-carbon steels. Models such as the phenomenological model developed by G. R. Johnson and W. H. Cook [62] and physically-based developed by F. J. Zerilli and R. W. Armstrong [63] are widely used to describe the flow behavior of metal at high-temperature and high-strain rates. However, these models do not provide the flexibility and framework to model detailed structural response at high temperatures[4]. The latter feature is available in models used by civil engineers; they use them to model the response of steel structure of buildings during fires. In this regard, as representative samples, we can cite the model described in the article by K. W. Poh [71] and standard such as the Eurocode 3 [72]. A comprehensive review of the data and the models may be found in the reports by Lueke *et al.* [73] and [74]. In addition to the description of models, the preceding reports contain compilations of the data available in the literature. The next subsections provide a description of the model used and fits to the experimental data for TC128B and A516-70.

7.1 Temperature-Dependent Modulus of Elasticity

From the data listed in Table 9, a model for the temperature dependence of the Young's modulus may be developed. Such a model will be crucial for describing elastic behaviour over the range of temperatures expected in a fire event. In this regard, the model developed by K.W. Poh [71] and the model recommended in Eurocode 3 [72] were deemed to be unwieldy owing to the large number of parameters used in the fits; five in the former and ten in the latter. This was also discussion in the paper *High-temperature properties of steel for fire resistance modeling of structures* [75].

W. E. Luecke [74] found that a simple three-parameter polynomial fit was found to model the temperature-dependent modulus as well as the previous two models. The fit reads

$$E(T) = E_{RT} + e_1 T + e_2 T^2 + e_3 T^3, \tag{8}$$

where T is the temperature, E_{RT} is the modulus at room temperature, and the lower case e_1 to e_3 are fitting constants.

The resultant polynomial fits of the temperature-dependent data given in Table 9 is shown in Figure 73. TC128B is shown in blue and A516-70 in black. The fitting parameters are given in Table 19.

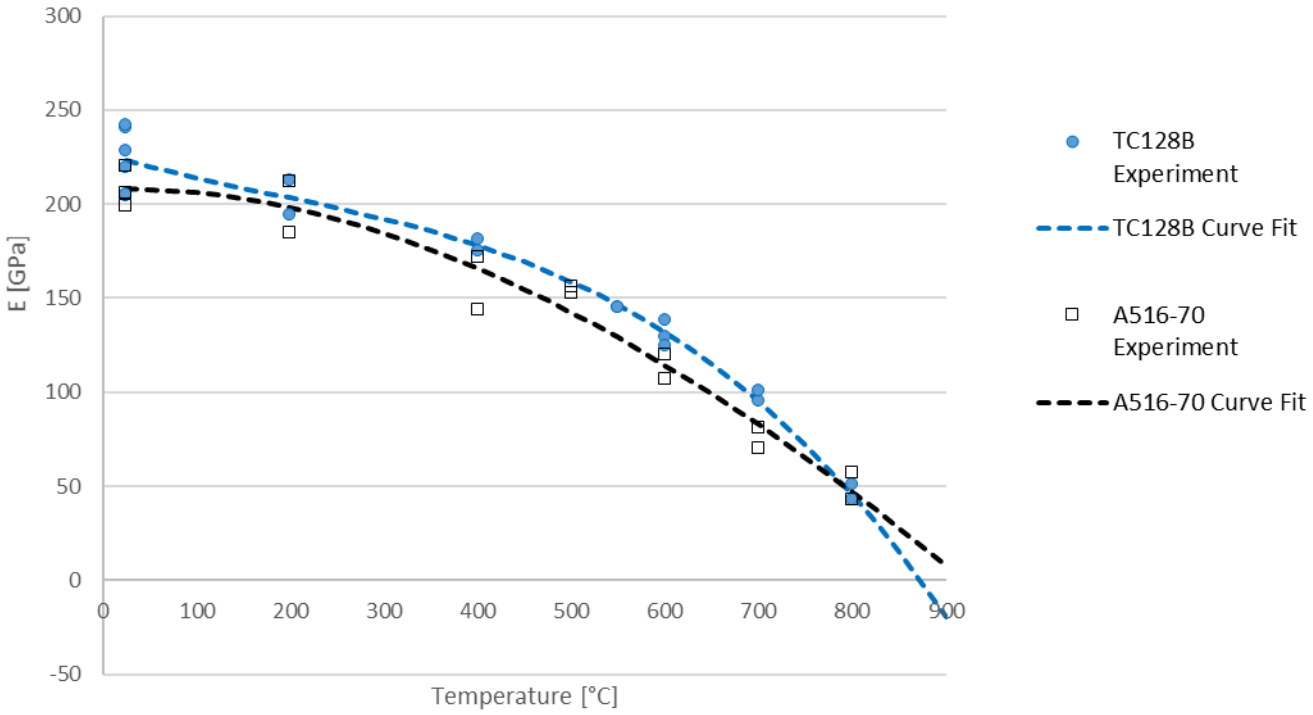

Figure 73: Temperature dependence of Young's Modulus. TC128 experimental data and curve fit are in blue. A516-70 is shown in black. The dotted lines denote the curve fits while the experimental results are shown as discrete data points.

Table 19: Constants for temperature-dependent elastic modulus of TC 128B and A516-70

	TC128B	**A516-70**
E_{RT} **[GPa]**	228	208.11
e_1 **[GPa/C]**	-0.19977	1.048×10^{-2}
e_2 **[GPa/C^2]**	-3.855×10^{-4}	-3.152×10^{-4}
e_3 **[GPa/C^3]**	-5.3513×10^{-7}	6.273×10^{-8}

7.2 Temperature-Dependent Yield Strength

It is well known that the yield strength decreases as temperature increases. Often, the decrease is taken to be linearly dependant on the temperature increase; see, for instance, the Johnson-Cook model [62]. Alternatively, physically-based models such as the Zerilli-Armstrong model [63] introduce the temperature dependence through an exponential dependence on the activation energy. For fire protection in structural engineering practice (see, for example, the work by K. W. Poh [71] and V. Kodur [75]) the models are empirical fits to data.

As in the case of the elastic modulus, the models for the temperature-dependent yield strength (0.2% offset) proposed in structural engineering practice have been reviewed by W. E. Luecke *et al* [73], and an alternative proposed. A reduction factor on the room-temperature strength is assumed and it reads.

$$\sigma_y(T) = \sigma_{y0} exp\left(-\frac{1}{2}\left[\frac{T-RT}{r_3}\right]^{r_1} - \frac{1}{2}\left[\frac{T-RT}{r_4}\right]^{r_2}\right), \tag{9}$$

where RT is room temperature, and r_i are fitting constants. The results of the fit to data in Table 9 are shown in Figure 74. The fitting constants are shown in Table 20. The horizontal lines show the minimum requirement for the yield strength at RT as specified by the AAR for TC128 (blue) and A516-70 (black). A commonly quoted rule of thumb for structural steels is that the strength is reduced to half the RT value when the temperature is raised to 538 ºC (see, for instance, [73]). This rule of thumb is borne out by the present data.

Table 20: Constants for temperature-dependent yield strength of TC128B and A516-70

	TC128B	**A516-70**
σ_{y0} **[MPa]**	354	396
r_1	3.875	5.5
r_2	0.795	1
r_3 **[ºC]**	612.763	610
r_4 **[ºC]**	529.184	550

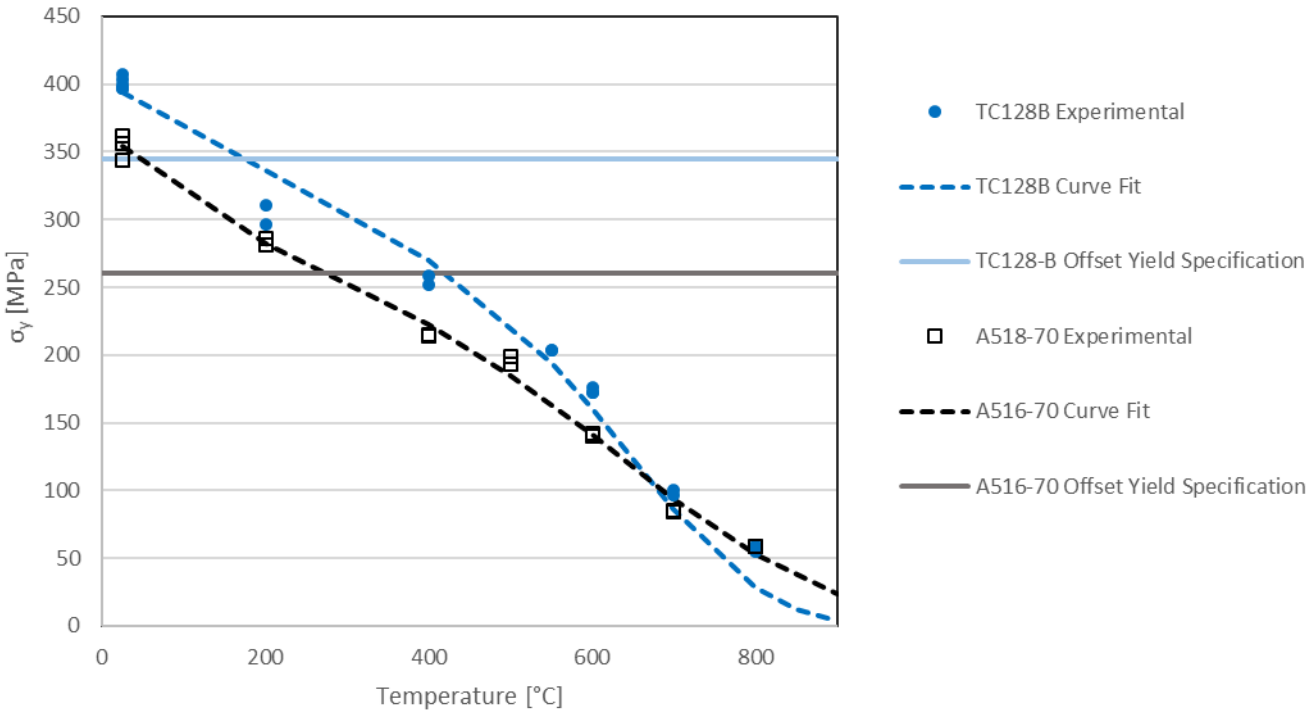

Figure 74: Temperature dependence of yield strength (0.2% offset). TC128 experimental data and curve fit are in blue. A516-70 is shown in black. The horizontal lines in light blue and gray show the minimum specified yield strength for TC128B and A516-70 respectively.

7.3 Temperature-Dependent Ultimate Strength

The expected softening of the stress-strain response and dependence of the ultimate tensile strength on temperature is observed in the data of Table 9. For the purpose of model development, the UTS computed from the true stress is used, and these are displayed in Figure 75. Again, a dashed horizontal line represents the minimum UTS required by the AAR. Filled diamonds display the measurements of UTS reported by [24].

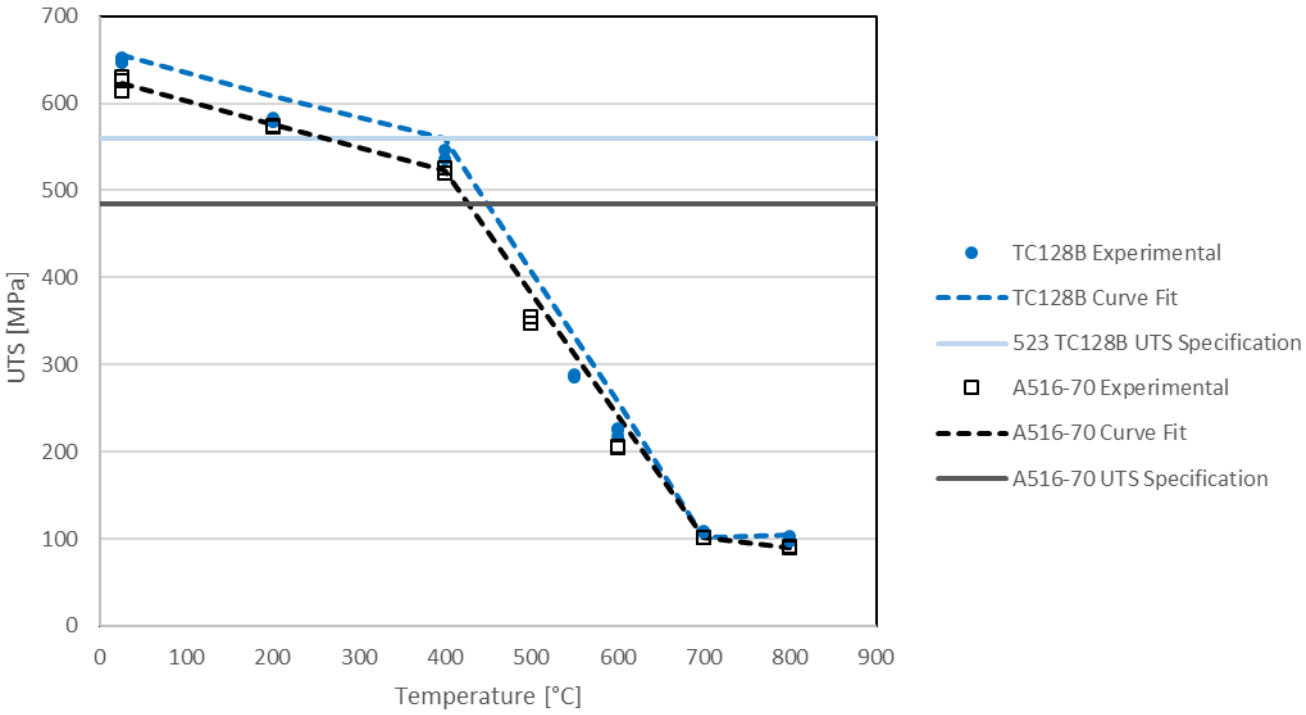

Figure 75: Temperature dependence of UTS. TC128 experimental data and curve fit are in blue. A516-70 is shown in black. The horizontal lines in light blue and gray show the minimum specified UTS for TC128B and A516-70 respectively.

Piecewise linear fits over the temperature ranges (RT, 400ºC), (400ºC, 700ºC), and temperatures greater than 700ºC are used to model the functional dependence of ultimate strength and temperature. The fits are given below.

A piecewise linear fit for the UTS of TC 128B:

$$\sigma_u(T) = \begin{cases} 662 - 0.2668\,T & RT \leq T \leq 400^o\,C \\ 1161.667 - 1.50667\,T & 400^oC < T \leq 700^oC \\ 201 - 0.12\,T & 700^oC < T \end{cases} \quad (10)$$

A piecewise linear fit for the UTS of TC A516-70:

$$\sigma_u(T) = \begin{cases} 629.667 - 0.26667\,T & RT \leq T \leq 400^oC \\ 1085.0 - 1.4050\,T & 400^oC < T \leq 700^oC \\ 182.0 - 0.115\,T & 700^oC < T \end{cases} \quad (11)$$

7.4 Stress-Strain Model

Combining the results and models for the elastic modulus and yield strength, a universal stress-strain curve that is a function of temperature may be developed as follows:

$$\sigma(T) = \begin{cases} E(T)\varepsilon, & \varepsilon \le \sigma_y(T)/E(T) \\ \sigma_y(T) + (\sigma_u(T) - \sigma_y(T))\left[1 - \exp(-n\varepsilon_p)\right], & \varepsilon > \sigma_y(T)/E(T)' \end{cases} \quad (12)$$

where $E(T)$ is given by Eq.(9) and $\sigma_y(T)$ by Eq (10). The function for $\sigma_u(T)$ is obtained by using the piecewise linear fit represented by Eqs (10) and (11). In the above expression, ε_p is the effective plastic strain and n is the hardening exponent. The above expression is a modification of the well-known Voce hardening law.

The hardening exponents used was TC128B and A516-70 are n =17 and n =18 respectively. It should be noted that n determines the shape of the curve between σ_y and σ_u. Small changes to n do not have a significant impact on the model. The results of this model are plotted against the experimental data for TC128B and A516-70 in Figure 76 Figure 77. Notice that the model curves are monotonically increasing functions of strain with a cap at the saturation value as dictated by the Voce model. The onset of localization and failure is not captured in this model. The latter feature can be accounted for through finite element modelling. Owing to the simplicity of the above expression, incorporation into commercial finite element software through user-defined subroutine is straightforward.

The main advantages of this model is that the fitting process is simple, the resulting equations can be easily applied in a finite element code and the overall trends of yield strength and UTS are captured well. The main disadvantage is that the change in the shape of the stress strain curve is not well captured since n is held constant across all temperatures.

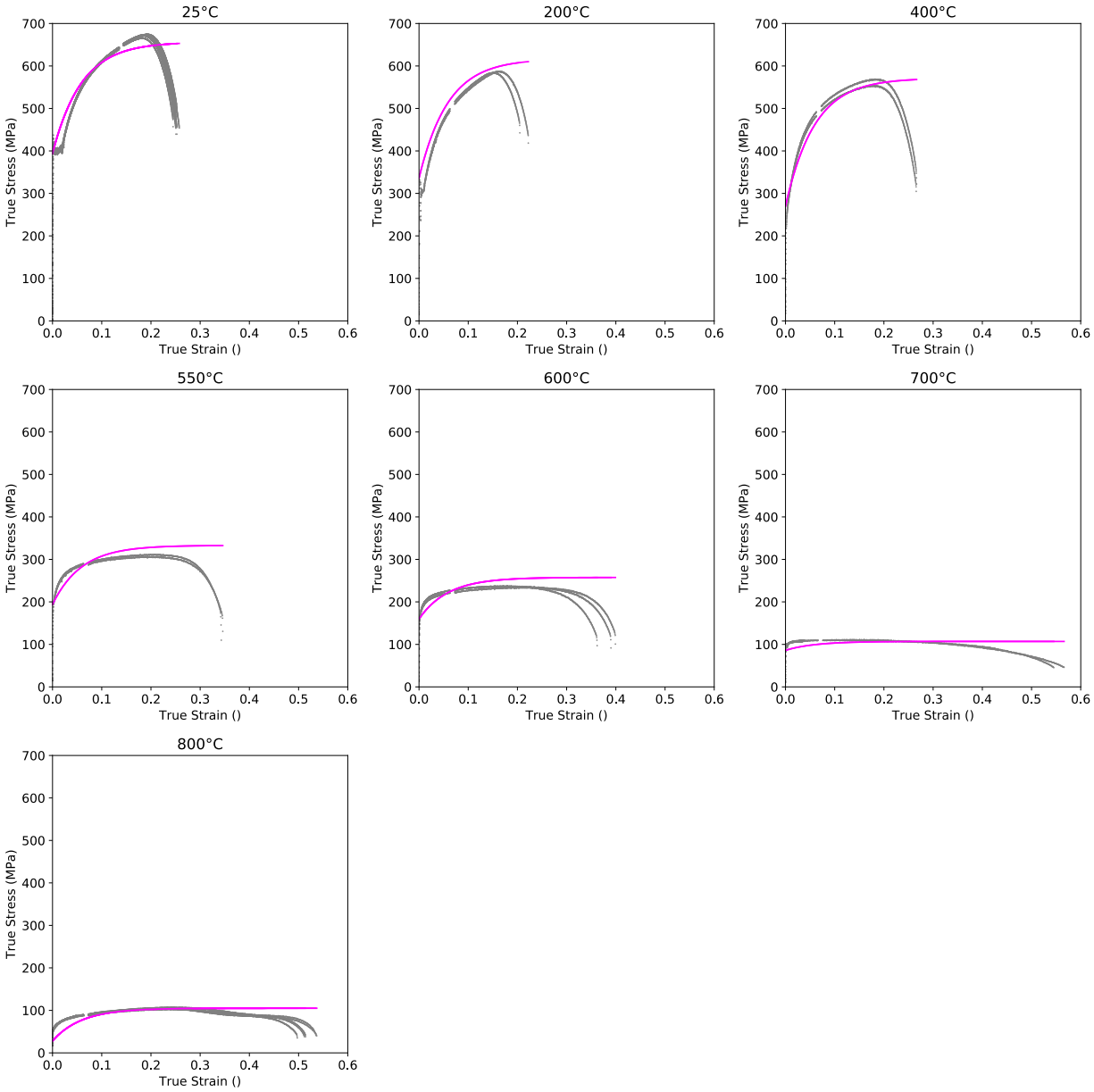

Figure 76: Tensile true stress versus true strain curves for TC128B. Material Model fits are shown in magenta. The experimental data is in grey.

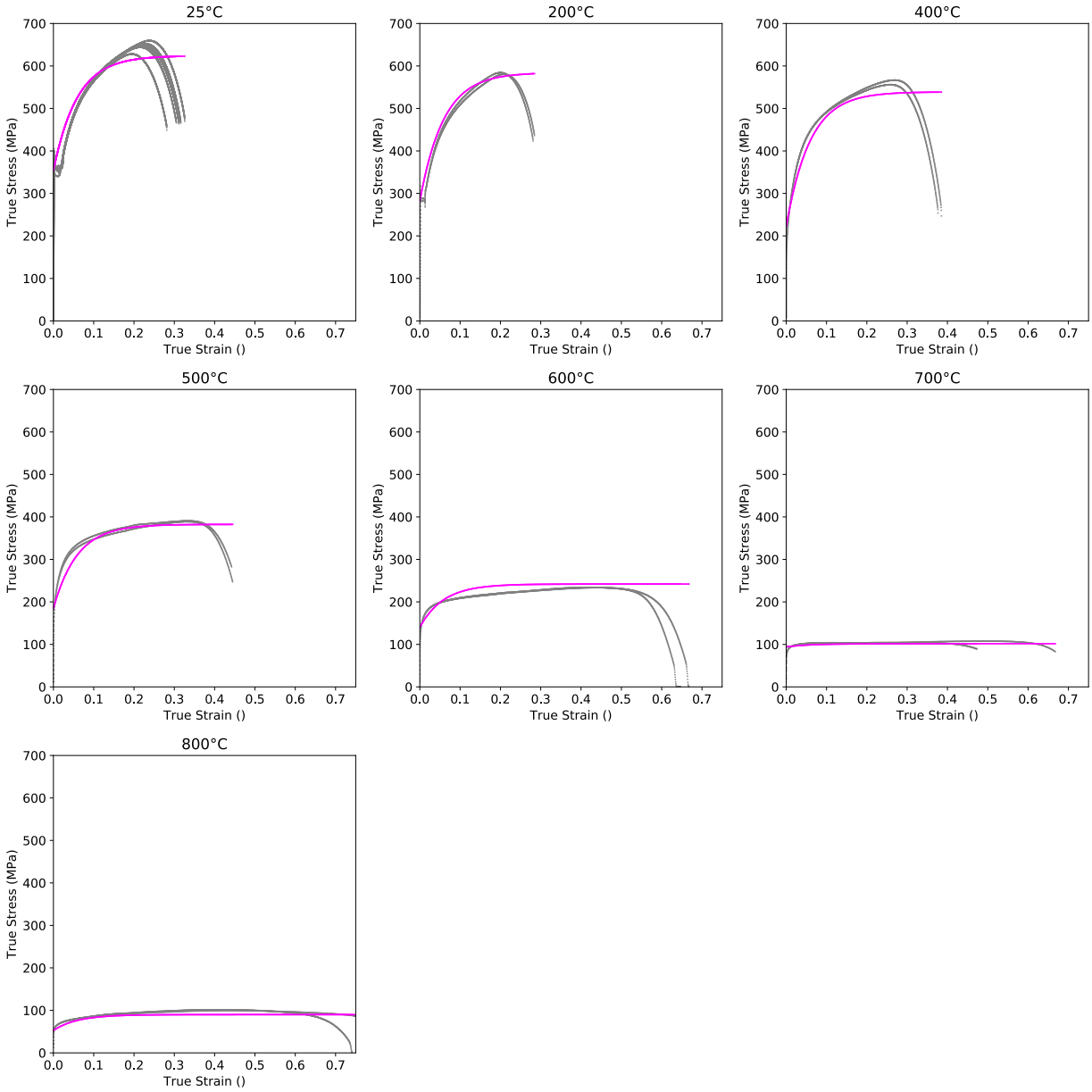

Figure 77: Tensile true stress versus true strain curves strain curves for A516-70 Material Model fits are shown in magenta. The experimental data is in grey.

8 SUMMARY AND CONCLUSIONS

Over the past several years CanmetMATIALS & Transport Canada have undertaken a comprehensive materials testing program in order to fill gaps in the knowledge of tank car materials and how they behave in accident scenarios. Two main areas of interest were investigated. The first being low-temperature failure response; this included low-temperature tensile tests and fracture toughness measurements (CVN, SE(B), SE(T), and DWTT). The second area of interest was high-temperature material behaviour including measuring the plastic deformation and creep rupture response. The steels under investigation were A516-70 and TC128B, the two most commonly used steels for rail tank cars.

Some key conclusions include:

- The composition of the A516-70 and TC128B steel tested met specifications. The low S and P contents are consistent with current steelmaking technology.
- Both steels exhibited Lüders bands (discontinuous yielding) at low plastic strain at temperatures of 200°C and below,
- No significant tensile anisotropy was observed for either material,
- Both steels have Charpy absorbed energy values that are substantially higher than the AAR specification at -46°C,
- Fracture propagation toughness values, $CTOA_{B/2}$, are reported for both steels.
- The results of B×2B SE(B) tests, representing baseline conservative fracture toughness values, were acceptable for structural applications although in the low range of typical modern steels,
- Increasing temperature resulted in lower yield stress and ultimate tensile stress, but higher ductility,
- The material's tensile properties were fit to a model, suitable for temperatures ranging from 25 °C to 800 °C, which can be implemented, in the future, into a finite element code for the purpose of modelling tank car failure in pool fire scenarios,
- Creep rupture testing was completed on both steels at temperatures ranging from 500°C to 800°C. As expected the rate of creep increased with temperature and applied load.

9 FUTURE WORK

CanmetMATERIALS intends to continue to investigate tank car steels and tank car failure. Key future tasks include:

1. Developing a finite element simulation of a tank car in a pool fire scenario. This task includes:
    a. Implementing the stress-strain model presented in this report to describe high-temperature plastic deformation as a user defined material model,
    b. Developing a constitutive a creep model based on the experimental data provided in the report which can be utilized in FEA to predict rupture time at various temperatures and loading scenarios,

   c. Mapping temperature contours and pressure data as boundary conditions to a model of rail tank car geometry.
2. J values for Deep-cracked SE(T) specimens and Shallow-cracked SE(T) specimens from experiment were presented in the report. Some characteristics of the fracture response were found to be different than typical with other steels. This may be attributed to the discontinuous yielding response at low plastic strains. Consequently, an investigation using FEA into the importance of discontinuous yielding on tank car steel fracture is being performed.
3. Mechanical testing of tank car weld material, including high-temperature, low-temperature, and fracture testing to determine if welds represent a weak point of the tank car structure.

REFERENCES

[1] S. Xu, “A Review of the Strength and Fracture Toughness Properties of Two Tank Car Steels: TC128B and A516-70 - CMAT WF 8933792,” 2016.

[2] S. Xu *et al.*, “Tensile and Fracture Toughness of a Current Tank Car Steel, A516-70 - CMAT WF 25325866,” 2018.

[3] S. Xu, J. Liang, L. Yang, A. Laver, and W. R. Tyson, “Tensile and Fracture Toughness of a Current Tank Car Steel, TC128B - CMAT WF 16144032,” 2017.

[4] C. H. M. Simha, “Mechanical Properties of Tank Car Steel at Flame Temperature and Modeling of Failure - A Review - CMAT WF 5792872,” 2016.

[5] H. Simha and J. Mckinley, “High-Temperature Mechanical Properties of Tank Car Steel - Testing and Analysis - CMAT WF 15390827,” 2017.

[6] J. Mckinley and C. H. M. Simha, “High-Temperature Mechanical Properties of ASTM 516 Grade 70 Plate Testing and Analysis,” 2018.

[7] D. N. Senior, “Internal Corrosion of Rail Tank Cars.”

[8] J. E. Gordon and O. Orringer, “Prospects for Making Carbide-Free Bainitic Thick Steel Plate by Means of Controlled Quenching: a First Estimate,” *ASME Int. Mech. Eng. Congr. Exhib.*, vol. 10, pp. 119–126, 1995.

[9] M. R. Johnson and E. A. Phillips, “Study of Railroad Tank Car Thickness Minimums, RPI-AAR Railroad Tank Car Safety Research and Test Project, Report No. RA-12-3-56,” 1989.

[10] E. Phillips and H. Role, “Phase 17 Report on Study of Class 105A Tank Cars (Car Population and Accident Data Analysis),” *RPI-AAR Railr. Tank Car Saf. Res. Test Proj. Rep. No. RA-17-1-43 (AAR R-433), August 22, 1980*.

[11] A. Bing, A. Dizon, J. Brickett, A. Papson, and L. O’Rourke, “Risk Evaluation Framework and Selected Metrics for Tank Cars Carrying Hazardous Materials,” *DOT/FRA/ORD-15/07, May 2015*.

[12] S. Vaynman, M. E. Fine, and Y.-W. Chung, “Evaluation and Application of Super-Tough Steel for Use in Tank Cars Transporting Cryogenic Liquids,” *Cent. Commer. Innov. Transp. Technol. (CCITT), Febr. 1, 2012*.

[13] E. A. Philips, E. A. Eiber, M. S. R. D.R. Stephen, D. R. Ahlbeck, and E. C. Rodabaugh, “Tank Car Design Basis – Yield vs. Tensile,” *AAR Rep. No. R-668, Battelle Columbus Lab. Columbus, OH, 1987*.

[14] T. L. Anderson, *Fracture Mechanics: Fundamentals and Applications*. 3rd ed., CRC Press, Boca Raton, Fla, 2005.

[15] F. R. Ahad, K. Enakoutsa, K. N. Solanki, Y. Tjipowidjojo, and D. J. Bammann, “A Physically Motivated Internal State Variable Plasticity/Damage Model Embedded with a Length Scale for Hazmat Tank Cars’ Structural Integrity Applications,” *Proc. ASME/ASCE/IEEE 2011 Jt. Rail Conf. JRC2011, March 16-18, 2011, Pueblo, Color. USA, JRC2011-56063*.

[16] T.L. Anderson, B. Rose, P. C. McKeighan, and S. W. Kirkpatrick, “Quantifying and Enhancing Puncture Resistance in Railroad Tank Cars Carrying Hazardous Materials. Phase II: Development and Validation of a Puncture Resistance Evaluation Methodology,” *Prep. Transp. Issues Team, Chlorine Institute, Arlington, VA, December 2007*.

[17] “Railway Investigation Report R13D0054 - Runaway and main-track derailment,” 2013.

[18] "Accident Involving Two Freight Trains - Accident No. DCA14MR004," 2013.
[19] R. Lautkaski, "Evaluation of BLEVE risks of tank wagons carrying flammable liquids," *J. Loss Prev. Process Ind.*, vol. 22, no. 1, pp. 117–123, 2009.
[20] F. Lees, *Lees' Loss prevention in the process industries: Hazard identification, assessment and control*. Butterworth-Heinemann, 2012.
[21] A. D'Aulisa, A. Tugnoli, V. Cozzani, G. Landucci, and A. M. Birk, "CFD modeling of LPG vessels under fire exposure conditions," *AIChE J.*, vol. 60, no. 12, pp. 4292–4305, 2014.
[22] "MHIDAS - Major Hazard incident Data Service." 2003.
[23] R. K. Eckhoff, "Boiling liquid expanding vapour explosions (BLEVEs): A brief review," *J. Loss Prev. Process Ind.*, vol. 32, pp. 30–43, 2014.
[24] G. E. Hicho and D. E. Harne, "Mechanical Properties and Fracture Toughness of AAR TC 128 Grade B Steel in the Normalized, and Normalized and Stress Relieved Conditions," *Gov. Res. Announc. Index(USA)*, p. 46, 1991.
[25] A. Zahoor and G. E. Hicho, "Materials and Fracture Mechanics Assessments of Railroad Tank Cars," *NIST Report, NISTIR-6266, Sept. 1998*.
[26] R. Viswanathan, *Damage mechanisms and life assessment of high temperature components*. ASM international, 1989.
[27] C. S. Hybinette, "Current Approaches to Tank Car Safety Enhancement," *Proc. 39th MWSP Conf. ISS, Vol. XXXV, 1997, pp. 1149-1152*.
[28] J. P. Hughes, C. F. Heuer, and T. L. Anderson, "Fracture Behavior of Tank Car Steels in Accidents from 1981 through 1994," *Sims Prof. Eng. RPI-AAR Railr. Tank Car Saf. Res. Test Proj. AAR Rep. No. R-924 (Report No. RA-03-6-62), AAR, Washington, D.C., December 1998*.
[29] S.W. Kirkpatrick, R. W. W. S. Pellini, D. H. Stone, and J. W.J. Harris, "Risk Assessment for Damaged Pressure Tank Cars," *PVP-Vol. 458, Comput. Technol. Appl. ASME, 2003, PVP2003-1920*.
[30] E. A. Phillips and W. S. Pellini, "Phase 03 Report on Behavior of Pressure Tank Car Steels in Accidents," *Railr. Tank Car Saf. Res. Test Proj. Rep. No. RA-03-6-48 (AAR R-553), June 20, 1983*.
[31] P. C. McKeighan, "Mechanical Properties of Tank Car Steels Retired from the Fleet," *SwRI Proj. No. 18.12240, August 2008*.
[32] P. C. McKeighan, D. Y. Jeong, and J. W. Cardinal, "Mechanical Properties of Tank Car Steels Retired from the Fleet," *Proc. 2009 ASME Jt. Rail Conf. JRC2009, March 3-5, 2009, Pueblo, Color. USA, JRC2009-63060*.
[33] D. Bai, J. Dorricott, F. Hamad, and S. Hansen, "Development of a Low Carbon HSLA Alternative to TC128 for Tank Car Application," *Proc. MS&T 2004, New Orleans, Louisiana, USA, Sept. 26-29, 2004, pp. 407-416*.
[34] G. E. Hicho, "The Mechanical, Stress-Rupture, and Fracture Toughness Properties of Normalized and Stress Relieved AAR TC128 Grade B Steel at Elevated Temperatures," *Rep. NISTIR 5157, March 1993*.
[35] G. E. Hicho, T. A. Stewart, and R. J. Fields, "'Memorandum from G.E. Hicho, T.A. Stewart and R.J. Fields to Claire Orth regarding Report RA-03-7-53, letter dated October 28, 1987,'" *Exhib. 4-S, Docket No. DCA-02-MR002, Exhib. No. 4-S, Natl. Bur. Stand. Oct. 28, 1987*.
[36] L. L. Olson, "Phase 03 Data Display Report on Results of Tests on Mill Plate Samples and Samples Removed from Tank Cars Involved in Accidents," *Railr. Tank Car Saf. Res. Test Proj. 67195, Rep. No. RA-03-3-13, AAR Tech. Center, April 19, 1972*.

[37] S. Vaynman, M. E. Fine, and S. P. Bhat, “High-Strength, Low-Carbon, Ferrite, Copper-Precipitation-Strengthening Steels for Tank Car Applications,” *Proc. MS&T 2004, New Orleans, Louisiana, USA, Sept. 26-29, 2004, pp. 417-421*.

[38] R. K. Steele, “Steel Alloys with Lower Bainite Microstructures for Use in Railroad Cars and Track,” *DOT-VNTSC-FRA-98-11, January 2002*.

[39] R.L. Bodnar, F. Hamad, C. Penniston, and S. Roysum, “As-rolled Plate Product with Improved Yield Strength, Toughness, and Weldability for Pressurized Railroad Tank Cars,” *Proc. MS&T 2007 (4th Int. Symp. Railr. Tank Cars II), 2007, pp. 597-612*.

[40] M. Manohar and W. E. Heitmann, “Effects of Niobium, Titanium and Nitrogen on the Microstructure and Technical Properties of Normalized Tank Car Steel Plates,” *Proc. MS&T 2007 (4th Int. Symp. Railr. Tank Cars II), 2007, pp. 3484-3493*.

[41] W. E. Heitmann, F. C. Feher, C. Hybinette, and M. Manohar, “The Influence of Sulfur Concentration Below 0.006% Along With Sulfide Shape Control on the Charpy V-Notch Properties of Normalized and Stress Relieved TC128 Grade B Steel Plate,” *Proc. MS&T 2007 (4th Int. Symp. Railr. Tank Cars II), 2007, pp. 27-35*.

[42] S. R. Bala, “Evaluation of New Steels for Tank Cars,” *TP 1081OE, Weld. Inst. Canada, January 1991*.

[43] R. Sims, T. Ros-Yanez, and W. Heitmann, “HPS 50W Steel (ASTM A709) Applicability to Tank Car Structures,” *Proc. Mater. Sci. Technol. 2014 (MS&T 2014), Pittsburg, PA, USA, Oct. 12-16, 2014, pp. 1197-1210*.

[44] R. D. Sims, “Tank Car Steel Investigations,” *Proc. MS&T 2004, New Orleans, Louisiana, USA, Sept. 26-29, 2004, pp. 401-408*.

[45] C. Hybinette, “An Insight to the AAR Steels Task Force Projects and Initiatives to Improve Materials for Tank Car Construction,” *Proc. Mater. Sci. Technol. 2014 (MS&T 2014), Pittsburgh, PA, USA, Oct. 12-16, 2014, pp. 1189-1195*.

[46] “AAR Manual of Standards and Recommended Practices,” in *Specifications for Tank Cars*, 2007, p. Section C-III (Appendix M, M-1002).

[47] ASTM A516/A516M-10, “Standard Specification for Pressure Vessel Plates, Carbon Steel, for Moderate- and Lower-Temperature Service.” ASTM International, West Conshohocken, PA, 2015.

[48] C. D. Lundin, G. Zhou, and K. K. Khan, “Metallurgical Characterization of HAZ in A516-70 and Evaluation of Fracture Toughness Specimens,” *WRC Bull. 403, July 1995, pp. 1-88*.

[49] “Standard Terminology Relating to Fatigue and Fracture Testing,” in *ASTM E1823 – 13*, ASTM International, 100 Barr Harbor Drive, PO Box C700, West Conshohocken, PA 19428-2959, United States, 2014.

[50] G. E. Hicho and D. E. Harne, “Mechanical Properties and Fracture Toughness of AAR TC128 Grade B Steel in the Normalized, and Normalized and Stress Relieved Conditions,” *NISTIR 4660, Rep. No. 24, NIST, Sept. 1991*.

[51] A. M. Birk and K. T. Yoon, “High-temperature stress-rupture data for the analysis of dangerous goods tank-cars exposed to fire,” *J. Loss Prev. Process Ind.*, vol. 19, no. 5, pp. 442–451, 2006.

[52] E. ASTM, “8M: Standard test method for tension testing of metallic materials (Metric),” *Annual Book of ASTM Standards, Philadelphia*. 2016.

[53] ASTM, “E21-09 Standard Test Methods for Elevated Temperature Tension Tests of Metallic Materials.” 2009.

[54] “Standard Test Method for Determination of Crack-Tip-Opening Angle of Pipe Steels Using DWTT Specimens,” in *ASTM E3039-16*, ASTM International, 100 Barr Harbor

Drive, PO Box C700, West Conshohocken, PA 19428-2959, United States, May 2016, 2016.

[55] "Standard Test Method for Measurement of Fracture Toughness, ASTM International," in *ASTM E1820-13*, ASTM International, 100 Barr Harbor Drive, PO Box C700, West Conshohocken, PA 19428-2959, USA, 2014.

[56] N. Pussegoda, S. Tiku, and B. Tyson, "Test Protocol: Measurement of Crack-Tip Opening Displacement (CTOD) and J-Fracture Resistance Curves Using Single-Edge Notched Tension (SENT) Specimens," *Doc. No. 30166-001 (Rev. 01), BMT Fleet Technol. Limited, January 2014*.

[57] "Specifications for Tank Cars," in *AAR Manual of Standards and Recommended Practices Section C, Part III*, 2014, p. Specification M-1002, Appendix M.

[58] "Standard Specification for General Requirements for Steel Plates for Pressure Vessels," in *ASTM A20/A20M-15*, ASTM International, 100 Barr Harbor Drive, PO Box C700, West Conshohocken, PA 19428-2959, United States, 2015.

[59] X. Ren, H. O. Nordhagen, Z.-L. Zhang, and O. M. Akselsen, "Tensile Properties of 420 MPa Steel at Low Temperature," *Proc. Twenty-fifth Int. Ocean Polar Eng. Conf. Kona, Big Island, Hawaii, USA, June 21-26, 2015, pp. 346-352*.

[60] S. Xu, R. Bouchard, and W. R. Tyson, "Constitutive Equation for Structural Steels," *Met. Mater. Trans. A, Vol. 35A, 2004, pp. 1410-1414*.

[61] S. Xu and W. R. Tyson, "Effects of Strain Rate on Strength, and of Orientation on Toughness, of Modern High-Strength Pipe Steels," *J. Pipeline Eng. Vol. 14, No. 3, 2015, pp. 211-224*.

[62] G. R. Johnson and W. H. Cook, "A constitutive model and data for metals subjected to large strains, high strain rates and high temperatures," in *Proceedings of the 7th International Symposium on Ballistics*, 1983, vol. 21, no. 1983, pp. 541–547.

[63] F. J. Zerilli and R. W. Armstrong, "Dislocation-mechanics-based constitutive relations for material dynamics calculations," *J. Appl. Phys.*, vol. 61, no. 5, pp. 1816–1825, 1987.

[64] "TP14877, Containers for Transport of Dangerous Goods by Rail, a Transport Canada Standard," 2016.

[65] W. Oldfield, "Curve Fitting Impact Test Data: A Statistical Procedure," *ASTM Stand. News, Vol. 3, No. 11, 1975, pp. 24-29*.

[66] D. Chun, "Alternate Criteria for Notch Toughness Behavior Characterization of Certain Metals and Associated Design of Experiments," *J. Mater., JMLSA, Vol. 7, No. 2, June 1972, pp. 257-262*.

[67] S. Xu *et al.*, "Toughness of ERW Pipe Seam Welds: Interim Report of Results to Inform CSA Steel Pipe Standard," *CanmetMATERIALS Rep. C. 12243591*, 2016.

[68] R. Z. and W. R. T. S. Xu, J. Sollen, J. Liang, ""Effects of Notch Type and Loading Rate on CTOA of Modern X65 and X70 Pipe Steels," *Proc. 10th Int. Pipeline Conf. 2014 (IPC 2014), Calgary, Alberta, Canada, Sept. 29 – Oct. 3, 2014, ASME, IPC2014-33334*.

[69] W. R. Tyson, M. A. Gesing, C. H. M. Simha, and S. Xu, "Comments and Replies on the Paper 'Determination of Dynamic Rotation Factor for DWTT Specimens by Strain Analysis and Hardness Measurement', FFEMS, 2016, 39, 830–838, by J. Fang, J.W. Zhang, and Y.D. Zhou," *Fat. Fract. Eng. Mater Struct. (FFEMS), Vol. 40, 2017, pp. 1501–1505*.

[70] D.-Y. Park, W. R. Tyson, J. A. Gianetto, G. Shen, and R. S. Eagleson, "Evaluation of Fracture Toughness of X100 Pipe Steel Using SE(B) and Clamped SE(T) Single Specimens," *Proc. 8th Int. Pipeline Conf. (IPC 2010), Calgary, Alberta, Canada, Sept. 27 - Oct. 1, 2010, ASME, IPC2010-31282*.

[71] K. W. Poh, “Stress-strain-temperature relationship for structural steel,” *J. Mater. Civ. Eng.*, vol. 13, no. 5, pp. 371–379, 2001.
[72] Eurocode 3, “Eurocode 3: Design of Steel Structures-Part 1-2: General Rules-Structural Fire Design,” 2007.
[73] W. E. Luecke *et al.*, “Mechanical Properties of Structural Steels. Federal Building and Fire Safety Investigation of the World Trade Center Disaster.,” *Natl. Inst. Stand. Technol.*, 2005.
[74] W. E. Luecke, S. W. Banovic, and J. D. McColskey, *High-temperature tensile constitutive data and models for structural steels in fire*. 2011.
[75] V. Kodur, M. Dwaikat, and R. Fike, “High-temperature properties of steel for fire resistance modeling of structures,” *J. Mater. Civ. Eng.*, vol. 22, no. 5, pp. 423–434, 2010.